

**Lateral Surface Superlattices in strained InGaAs
layers**

Brian Milton

**Thesis submitted to the University of Glasgow's Department of Physics and
Astronomy for the Degree of Doctor of Philosophy, August 2000**

© Brian Milton 2000

ProQuest Number: 13818793

All rights reserved

INFORMATION TO ALL USERS

The quality of this reproduction is dependent upon the quality of the copy submitted.

In the unlikely event that the author did not send a complete manuscript and there are missing pages, these will be noted. Also, if material had to be removed, a note will indicate the deletion.



ProQuest 13818793

Published by ProQuest LLC (2018). Copyright of the Dissertation is held by the Author.

All rights reserved.

This work is protected against unauthorized copying under Title 17, United States Code
Microform Edition © ProQuest LLC.

ProQuest LLC.
789 East Eisenhower Parkway
P.O. Box 1346
Ann Arbor, MI 48106 – 1346

GLASGOW
UNIVERSITY
LIBRARY

12109- COPY 1

Acknowledgements

I am very grateful to all those who helped me throughout this work. Dr. Andrew Long, Dr. Elef Skuras and Dr. John Emeleus, who all helped immeasurably during fabrication and testing. Also, all the staff in Electrical Engineering who ran my beamwriter jobs and helped whenever things got a bit difficult. Also, thanks to Prof. John Davies, for a lot of help on the theoretical side.

I must also thank all my family and friends who have had to put up with me during this time.

Abstract

Lateral Surface Superlattices were fabricated by etching in strained InGaAs layers above a GaAs/AlGaAs 2DEG channel. These were etched both by dry plasma wet chemical etching to produce periods of 100nm, 200nm and 300nm. These superlattices were fabricated on Hall bars to allow four terminal measurement and a blanket gate was placed on top, to allow variations in the carrier concentration.

The magnetoresistance effects of these superlattices were studied at varying values of gate voltage, which varies the carrier concentration and the electrostatic periodic potential and at temperatures down to 45mK in a dilution refrigerator. From the oscillations observed in the magnetoresistance traces it is possible to calculate the magnitude of the periodic potential. This showed that the etched, strained InGaAs was producing an anisotropic piezoelectric potential, along with an isotropic electrostatic potential. The variation in period allowed a study of the change of this piezoelectric potential with the period as well as a study of the interactions between the electrostatic and piezoelectric potentials.

Further, at the lowest temperatures a strong interaction was observed between the Commensurability Oscillations, caused by the periodic potential, and the Shubnikov-de Haas Oscillations due to the Landau Levels. This interaction was studied as it varied with temperature and carrier concentration.

Contents

1	Introduction	1
1.1	Introduction	1
1.2	Outline	1
1.3	Review of previous work	2
2	Basic Theory	4
2.1	Introduction	4
2.2	2DEG Formation	4
2.3	Bulk effects in magnetic fields	6
2.4	Sources of lateral potential modulation	10
2.5	Periodic Modulation in Magnetic Fields	14
2.6	Estimation of potentials	17
3	Fabrication	22
3.1	Introduction	22
3.2	Facilities	23
3.3	Fabrication Techniques	23
3.3.1	Marker layer	26
3.3.2	Ohmic contacts	27
3.3.3	Isolation	28
3.3.4	Superlattice	29
3.3.5	Gate	31
3.4	Imaging	31
3.5	Packaging	35
4	Instrumentation	36
4.1	Introduction	36
4.2	The Blue System	36
4.3	The Black System	40

4.4	Data Acquisition	43
5	300nm period LSSL results	45
5.1	Introduction	45
5.2	Samples with a mark:space ratio of 1:10	46
5.3	Samples with a mark:space ratio of 1:1, Basic Features	52
5.4	Samples with a mark:space ratio of 1:1, Gate Effects	56
5.5	Potential Magnitudes of 1:1 mark:space ratio samples	58
5.6	Temperature dependence of 1:1 mark:space ratio samples	63
6	100nm and 200nm period LSSL, high temperature results	68
6.1	Introduction	68
6.2	100nm samples	68
6.2.1	Basic features	68
6.2.2	Gate effects	73
6.2.3	Potential magnitudes	75
6.2.4	Temperature	76
6.3	200nm samples	78
6.3.1	General features	78
7	100 nm period LSSL, low temperature results	82
7.1	Introduction	82
7.2	Basic Features	82
7.3	Section 1 (below 1T)	85
7.4	Section 2 (1T to 2 T)	89
7.5	Section 3 (above 3T)	91
7.6	Temperature dependence	94
7.7	Voltage effects	95
7.8	Hall resistance	97

8	Conclusion	103
8.1	Fabrication technique	103
8.2	Experimental results	104
8.2.1	Introduction	104
8.2.2	300nm samples	104
8.2.3	100nm samples	105
8.2.4	200nm period samples	106
Appendix	Data Accumulating using National Instruments	107
	Labview™ Software	
A.1	Introduction	107
A.2	Basics of programming in Labview™	107
A.3	Program specifics	109
A.3.1	Gatesweep programs	110
A.3.2	Magnetic Sweep programs	111
A.3.3	Capacitance programs	112
A.3.4	The FFT program	113

Figures

2.1	Conduction Band Diagram for a delta doped sample	5
2.2	Broadened Landau Levels as a function of energy	7
2.3	Schematic of edge states in a Hall bar in a strong magnetic field	8
2.4	Example of Shubnikov-de Haas oscillations and the equivalent Quantum Hall Plateaux	9
2.5	A slice through the wafer A1246	11
2.6	Schematic of Hall bar with crystal directions indicated	12
2.7	Schematic diagram of the component parts of the electrostatic potential produced by an etched rib in an LSSL	13
2.8	Theoretical calculations of magnitude of the piezoelectric potential versus period of LSSL for the first two harmonics	14
2.9	Sample trace from sample 9, period 300nm, current flow direction [011], taken at 5K with zero bias on the gate	18
3.1	The basic Hall bar	22
3.2	The lift-off process	26
3.3	Wam pattern for alignment layer	26
3.4	Ohmic pattern in Wam	27
3.5	Wam design of the isolation layer	28
3.6	Schematic design of a 1:1 mark:space Superlattice	29
3.7	Gate pattern as designed in Wam	31
3.8	AFM image of 300nm LSSL	32
3.9	SEM image of 300nm LSSL	33
3.10	Schematic of device in chip packaging	34
4.1	Schematic of VTI insert and sample rod	37
4.2	Measurement wiring	38
4.3	Connections in the sample holder	39
4.4	Schematic of the dilution refrigerator	41
4.5	Schematic of fridge electronics	42

5.1	Unpatterned Hall bar fabricated on control material and measured at 1.6K	45
5.2	The magnetoresistance of the 17s wet etch sample measured at 1.6K	47
5.3	Magnetoresistance of Sample 2 (12s wet) measured at 5K	48
5.4	Magnetoresistance of Sample 6 (90s dry) measured at 5K	48
5.5	Experimental Commensurability Oscillation positions from sample 6 compared to theory	49
5.6	Fast Fourier Transform of the traces plotted in Fig. 5.4	51
5.7	Fast Fourier Transform of Fig. 5.3	51
5.8	AFM image of an LSSL manufactured using the same conditions as Sample 9, but left ungated	52
5.9	Magnetoresistance of Sample 9 measured at 1.6K	53
5.10	Comparison of experimental CO peak positions against theory for the sample shown in Fig. 5.9	54
5.11	FFT of results shown in Fig. 5.9	55
5.12	Magnetoresistance traces obtained from the control samples, made at the same time, and under the same conditions as the stressor sample9	56
5.13	Voltage effects on the magnetoresistance of the $[01\bar{1}]$ orientation of sample 9 at 5K	57
5.14	Magnetoresistance variation with gate bias for $[001]$ crystal direction	58
5.15	Amplitude of the periodic potentials in sample 9	60
5.16	Potential magnitude calculated from sample trace shown in Fig. 5.12	62
5.17	Variation of magnetoresistance trace with temperature for sample 9, $[01\bar{1}]$	64
5.18	The trough magnitudes for sample 9 $[011]$ against temperature	65
5.19	The trough magnitudes for sample 9 $[01\bar{1}]$ against temperature	65
6.1	SEM micrograph of 100nm period etched surface	68
6.2	AFM analysis of 100nm LSSL, 90s etch time	69

6.3	Sample 11 measured at 10K	70
6.4	Theoretical potential magnitudes for sample 11	71
6.5	Fast Fourier Transform of the traces in Fig. 6.3	72
6.6	Variation of magnetoresistance traces with gate voltage for $[01\bar{1}]$ at 10K	74
6.7	Voltage effects for $[001]$ device	74
6.8	100nm LSSL potential at 10K	76
6.9	Temperature dependence of sample 11	77
6.10	$k=2$ trough depth against temperature for the $[01\bar{1}]$ sample	77
6.11	AFM picture of 200nm period LSSL	78
6.12	Magnetoresistance against magnetic field for the 200nm LSSL	74
6.13	Magnetoresistance against magnetic field for the 200nm LSSL	80
7.1	$[01\bar{1}]$ $T=45\text{mK}$ $V_g=0.3\text{V}$	82
7.2	Trace shown in Fig. 7.1 for differing values of excitation voltage	83
7.3	Comparison between high and low temperature runs	84
7.4	Section 1 $[01\bar{1}]$ $T=45\text{mK}$ $V_g=0.3\text{V}$	85
7.5	Second order perturbation calculation	86
7.6	DOS perturbation calculated from the Raikh and Shabazyan based model, compared to the experimental result	88
7.7	SdH oscillations displacement against filling factor	89
7.8	Section 2 $[01\bar{1}]$ $T=45\text{mK}$ $V_g=0.3\text{V}$	90
7.9	Section 3 $[01\bar{1}]$ $T=45\text{mK}$ $V_g=0.3\text{V}$	91
7.10	Anisotropy and small structure visible at high fields at 45mK, $V_g=0.3\text{V}$	92
7.11	Unpatterned control wafer (i.e. no InGaAs stressor layer) at 45mK	93
7.12	Temperature effects $[01\bar{1}]$ $V_g=0.3\text{V}$	94
7.13	Voltage effects for Section 1 and 2	95
7.14	Voltage effects for Section 3	95
7.15	Original Hall trace and with the linear component subtracted for $[01\bar{1}]$	97

7.16	An expanded view of the linear part removed trace shown in Fig. 7.15	97
7.17	Hall traces measured at different gate voltages	98
7.18	$1/B$ v. ν for $[01\bar{1}]$	99
7.19	Hall resistance at high magnetic field, $T=45\text{mK}$ $V_g=0.3\text{V}$ $[01\bar{1}]$ Linear part removed	100
7.20	$1/B$ against ν as measured from Hall traces of samples $[01\bar{1}]$	101
A.1	Example of code from the single magnetic sweep program	108
A.2	Front panel of the EG&G Gate sweep program	110
A.3	Single Magnetic Sweep program Front Panel	110
A.4	Front Panel of Fast Fourier Transform program	113

Tables

3.1	Parameters of superlattices produced for this thesis	30
3.2	Samples studied for this thesis	35
3.3	Theoretical values of potential modulation in 300nm period $[01\bar{1}]$ sample	59

Chapter 1 Introduction

1.1 Introduction

This thesis will cover work carried out between October 1996 and October 1999. It was a continuation of work carried out by S. Vallis and E. Skuras et al[1-4] prior to my arrival in the group.

They had studied striped metal gate superlattices, with a variety of periods. They studied the magnetoresistance traces obtained for various magnitudes of potential and with various periods. They discovered that strain in the metal gates led to a piezoelectric potential, which combined with the purely electrostatic potential from the biased gates. It was therefore suggested that producing superlattices using intentionally strained, etched layers would lead to larger potential magnitudes and allow greater study of the piezoelectric contribution. Also, it would allow the electrostatic variation of the carrier concentration to be carried out independently of the periodic potential. Hence, for this work I studied etched superlattices on similar wafers to that used by E. Skuras and S. Vallis, concentrating on the magneto-resistance results.

I produced 300nm, 200nm and 100nm period superlattices with a range of electrostatic potential sizes. These were produced by dry plasma and wet chemical etching, making use of a positive resist mask, with the pattern being written by a beam writer.

1.2 Outline

In Chapter 2 will detail the basic theory behind semiconductor heterostructures and superlattices. This will include a look at the theory of the piezoelectric effect as applied to periodic arrays of stressor material.

Chapter 3 details the fabrication procedures involved in the production of the experimental samples. This will include wafer preparation, beam writer techniques and a full list of the different patterns written.

Chapter 4 involves the measurement equipment used. This involved two different Oxford Instruments cryostats, denoted black and blue, with two different cooling inserts.

Chapters 5,6,and 7 will detail the results obtained. Chapter 5 will involve the initial experiments carried out while the fabrication procedure was still being perfected, involving 300nm period devices. Chapter 6 will include 100nm and 200nm devices as measured in the blue measurement system at higher temperatures and Chapter 7 will cover the 100nm devices, measured at the lowest temperatures in the black system. Chapter 8 will bring together all the conclusions obtained through out the work.

1.3 Review of previous work

The previous work carried out in this department involved striped metal gates. That is, a striped, periodic pattern was written in resist by the beamwriter and then a gold film was evaporated over the top. When the resist was dissolved away any gold adhering to the wafer surface remained, leaving behind a set of gold lines. These were then connected together, away from the measurement region, to form one continuous gate. A bias could then be applied to this gate to create a periodic electrostatic potential at the level of the 2DEG. It is the interaction between the electrons and this periodic potential that was studied. These were studied by A.C. lock-in techniques in a Helium cryostat at temperatures of approximately 1.5K.

There are a number of problems with this method. For small periods it can be very difficult to get a continuous gate. This can lead to unmodulated areas of the electron gas. Also, as the period becomes reduced, the effective potential at the 2DEG becomes smeared. Thus we end up simply depleting the electrons with no periodic effect. The magnitude of the potential is usually of the order of one percent of the Fermi level which is not very large, giving rise to small, noise prone oscillations.

It was, however, noted by those working in Glasgow [3] that there was a small periodic potential even when the gate bias was zero. This, it transpired, was due to strain from the gate metal. As the sample is cooled to measurement temperatures, the gate contracts at a different speed to the underlying substrate. This leads to a strain at the interface. It was initially believed that the electrostatic potential seen by the 2DEG was due to the deformation effect. This was proved to be theoretically too small however. Thus it was believed that the piezoelectric effect was the source.

Hence, the motivation for my work was to introduce a deliberately strained superlattice and study its properties. The aim being to prove that the piezoelectric effect

was present. After proving this I moved on to producing short period superlattices with potentials approximately ten percent of the Fermi level using these strained layers.

References

[1] S. Vallis PhD. Thesis University of Glasgow 1996

[2] E. Skuras, A.R. Long, I.A. Larkin, J.H. Davies, M.C. Holland *App. Phys. Lett.* **70** 871 (1997)

[3] R. Cuscó, E. Skuras, S. Vallis, M.C. Holland, A.R. Long, S.P. Beaumont, I.A. Larkin, J.H. Davies. *Superlattices Microstruct.* **16** 283 (1994)

[4] A.R. Long, J.H. Davies, M. Kinsler, S. Vallis, M.C. Holland. *Semicond. Sci. Technol.* **8** 1581 (1993)

Chapter 2 Basic Theory

2.1 Introduction

All experiments in this work were carried out on III-V semiconductors. The basic theory of charge accumulation and flow in these materials has been extensively studied. The effects of periodic potentials on the properties of these semiconductors is a more recent addition to the theory. The basics will be set out in the following chapter.

2.2 2DEG Formation

For any semiconductor the lattice can be thought of as a set of periodically charged points which make up planes of charge. As is known from X-ray optics, waves in a periodic structure undergo Bragg reflection. This is the fact that as the wave number becomes a multiple of the periodicity of the lattice, back reflection becomes a large factor. Thus when $k = \frac{n\pi}{a}$ (where k is the wavenumber, n is an integer and a is the period of the crystal lattice) a standing wave is set up between neighbouring lattice planes. This can be then described as two different charge densities which then allow two different energy states to exist [1]. These have the same wavenumber, and thus crystal momentum, but different energies. Thus an energy gap is formed. An insulator has an energy gap insurmountable to all electrons while a semiconductor has a smaller, yet not insignificant, gap. The region below the gap, where the majority of states are filled, is known as the valence band. Above the gap, where most of the states are empty, the region is known as the conduction band as this is where the electrons that conduct current reside, in our samples.

When a junction between two different layers of semiconductor is formed the energy gap is distorted. This can be best illustrated in a conduction band diagram. This is a diagram which describes the variation of the conduction band edge as a function of position. Fig. 2.1 shows such a diagram for a delta doped GaAs/AlGaAs heterostructure.

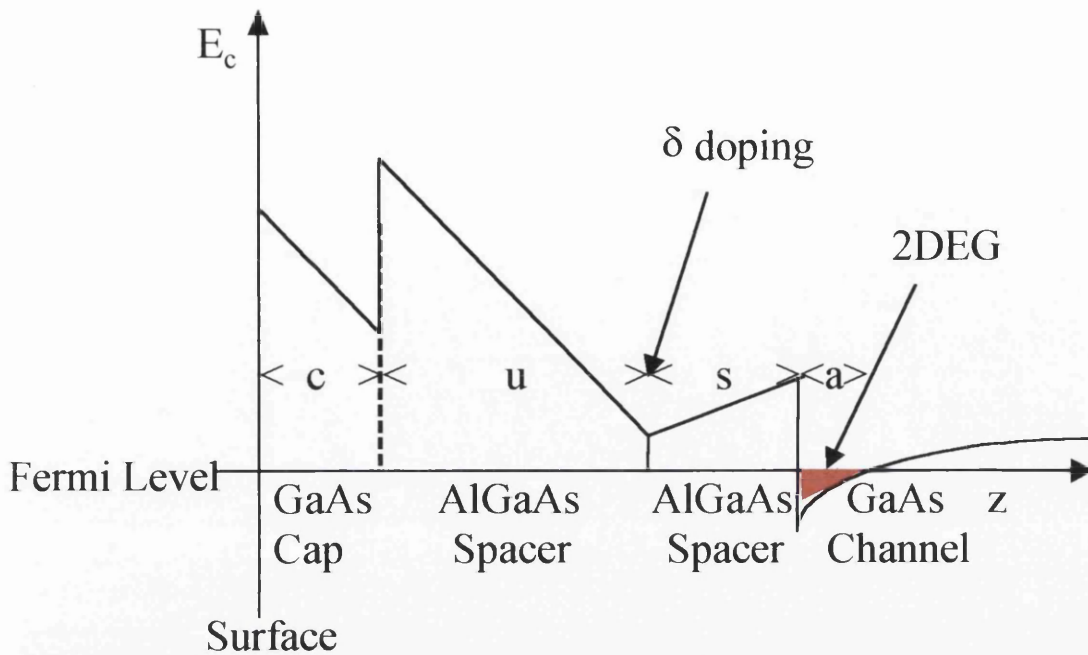


Fig. 2.1 Conduction band diagram for a delta doped sample. The distance into the wafer from the surface is represented by positive z .

As can be seen, the GaAs/AlGaAs interface produces an abrupt change in energy. This is due to the AlGaAs having a larger energy gap than the GaAs. Thus the conduction band is pushed up and the corresponding valence band is pushed down. Above a critical value of donor atoms inserted into the doping region the number of electrons produced is sufficient to fill the states at the GaAs surface and promote some electrons into the conduction band. Obviously these will fall into the lowest energy point which is at the inner GaAs/AlGaAs interface. The electrons are held against the interface by electrostatic forces, where the abrupt change in energy inhibits movement into the AlGaAs region, and electrons are free to move in two dimensions only. Thus a two dimensional electron gas (2DEG) is formed.[2]

Due to the obstruction in the z direction, the energy of the electrons splits into a set of subbands. These can be thought of as similar to the energy levels in a quantum well. If an electron has sufficient energy it can scatter from one subband to the next, effectively moving in the z direction. However, if the concentration of electrons is low and the gap between subbands large then this is unlikely to occur. Thus the electrons are truly confined in the z direction.

The number of electrons is governed by the energy band offsets in the sample and the depth of the well which is a function of the layer structure. If we assume that the donor ions are frozen at measurement temperatures, then the Fermi energy is pinned, and thus the concentration of electrons can be described as follows [3];

$$n_{2D} = \frac{(\Delta E_c - E_{dd})\epsilon_0}{\left(\frac{s}{\epsilon_a} + \frac{a}{\epsilon_g}\right)e^2} \quad (2.1)$$

where n_{2D} is the carrier concentration, ΔE_c is the conduction band offset between the GaAs and AlGaAs layers, E_{dd} is the pinning energy of the donor ions, ϵ_a and ϵ_g are the dielectric constants of the AlGaAs and GaAs respectively and s and a are as shown in Fig. 2.1.

2.3 Bulk effects in a magnetic field.

Applying a magnetic field perpendicular to the plane of the 2DEG causes the electrons to execute circular orbits. These are known as cyclotron orbits whose

frequency is: $\omega_c = \frac{|eB|}{m}$. The cyclotron radius is given by: $R_c = \frac{\sqrt{2mE}}{|eB|}$ [2].

For a 2DEG in zero field all different values of k have different energies.

However, as a field is applied, solving the Schrödinger equation for a magnetic field perpendicular to the flow of charge reveals that these states collapse into n degenerate levels broadened by scattering events, such as electron-electron scattering or impurity scattering. [2]. These levels have energies of $E_n = \left(n - \frac{1}{2}\right) \frac{h\omega_c}{2e}$. As can be seen in Fig.

2.2 all levels below the Fermi level are filled. As the magnetic field increases the energy of the Landau levels increases. Thus the Landau levels move past the Fermi level of the 2DEG forcing all the electrons in to lower levels and causing oscillations of the Fermi energy. The density of states available at the Fermi level changes, altering the resistance. The resistance oscillations, known as Shubnikov-de Haas (SdH)

oscillations, are periodic in $\frac{1}{B}$ in the following manner;

$$\Delta \frac{1}{B} = \frac{hn_{2D}}{2e} \quad (2.2)$$

where $\Delta \frac{1}{B}$ is the frequency, h is Planck's constant and e is the charge on an electron.

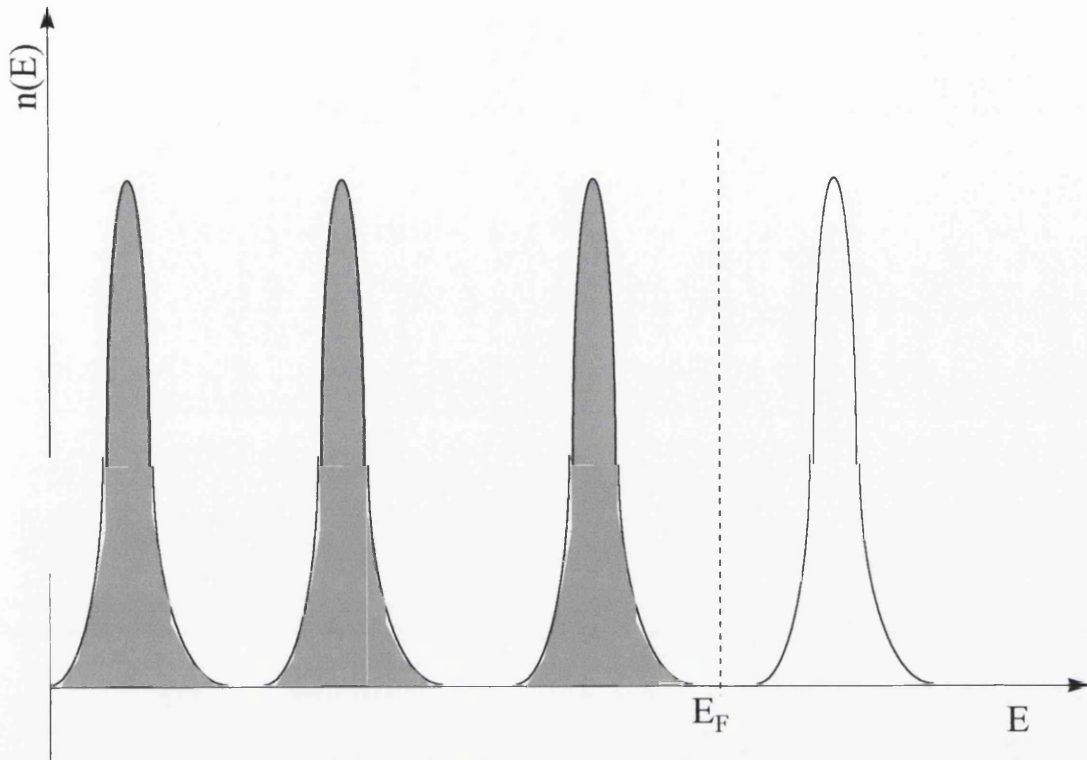


Fig. 2.2 Broadened Landau Levels as a function of energy

The transverse resistance is also affected by the magnetic field. As the field increases the well known Hall effect can be observed [4]. The Hall resistance increases in a linear fashion (the Classical Hall Effect) until the quantum Hall effect sets in. This manifests itself as a set of plateaux that occur at the same fields as the minima of the SdH oscillations and have a resistance that is an integer fraction of $\frac{h}{2e^2}$.

This can be explained if we think of edge states in the Landauer-Büttiker formalism [5,6]. In a strong magnetic field, when the Fermi level lies between Landau Levels in the bulk of the material, the electrons are forced to travel along the edge of the sample (Fig.2.3). If a voltage V is applied at contact A then current $-\left(\frac{e^2}{h}\right)V$ is injected into each of the upper edge states. As no net current flows in or out of the voltage contacts C and D they must have an equal voltage V upon them. The same argument applies to the lower voltage contacts E and F which have an equivalent

voltage to that of contact B, i.e. 0V. Hence the total current flowing is $-N\left(\frac{e^2}{h}\right)V$ and

the Hall resistance becomes $\frac{(V_D - V_G)}{I} = -\frac{V}{I} = -\frac{1}{N}\left(\frac{h}{e^2}\right)$. This is the Hall plateau

resistance.

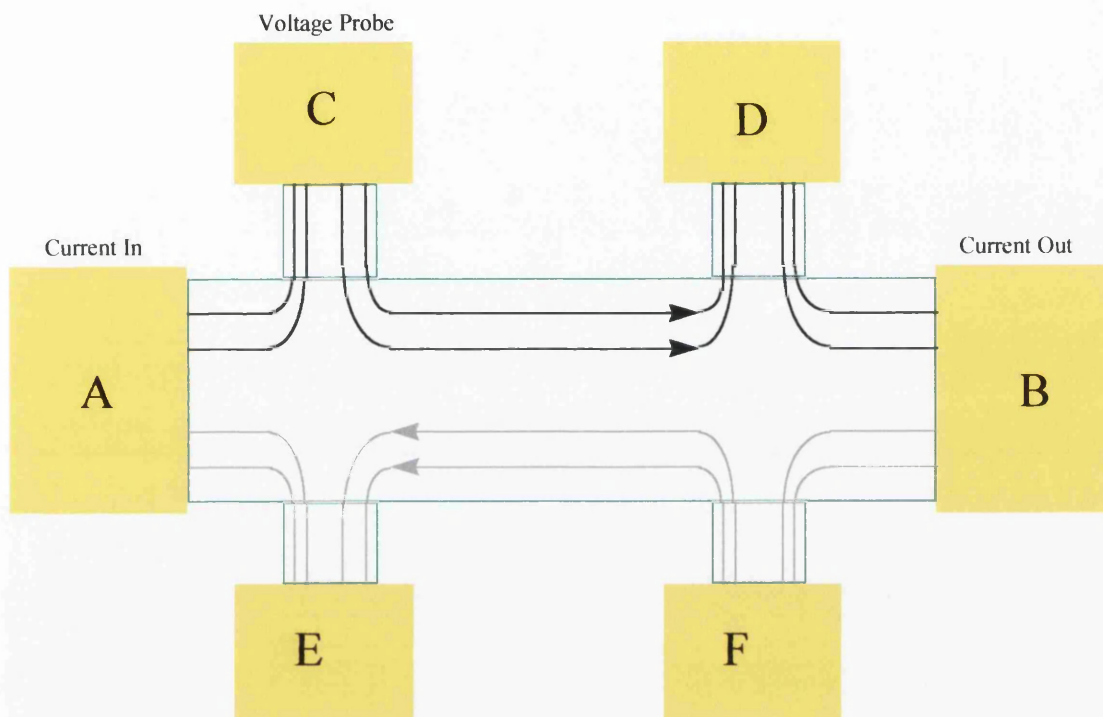


Fig. 2.3 Schematic of edge states in a Hall bar in a strong magnetic field

An example of these two phenomena are shown in Fig 2.4. The Hall plateaux can be seen to oscillate about the line of the Classical Hall effect. It is also easy to see that the plateaux correspond to the minima in the SdH oscillations, indicating their common origin.

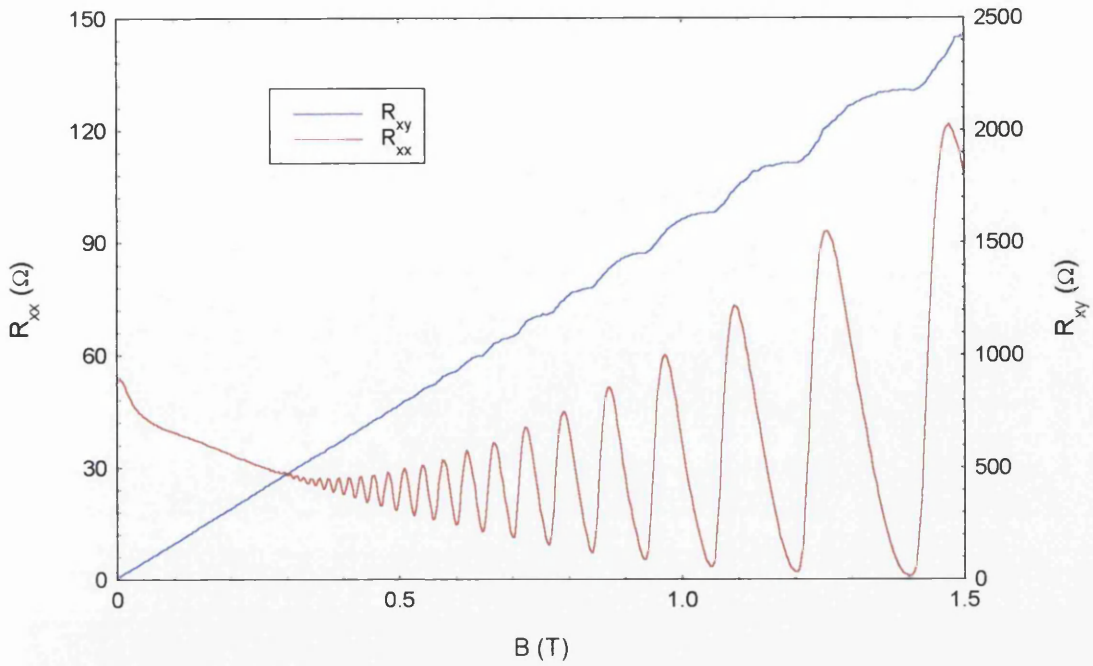


Fig 2.4 Example of Shubnikov-de Haas oscillations and the equivalent Quantum Hall Plateaux

It is possible to calculate the carrier concentration from the above mentioned Hall traces. This involves measuring the Hall resistance at zero and a fixed field and combining this information with the longitudinal resistance. This comes from;

$$R_{xy(B=X)} - R_{xy(B=0)} = \frac{X}{ne} \quad (2.3)$$

where X is the fixed field value and

$$\mu = \frac{L_x}{L_y} \frac{1}{R_{xx(B=0)} ne} \quad (2.4)$$

where L_x/L_y is the ratio of length to width of the Hall bar and μ is the Hall mobility. Hence it is possible to measure the carrier concentration and Hall mobility free from any variations due to magnetic field. It is also possible to calculate the carrier concentration purely from longitudinal resistance measurements. If the frequency of the SdH oscillations are obtained then the concentration can be calculated from Eqn. 2.2. These two methods supply a useful check to each other.

2.4 Sources of lateral potential modulation.

The periodic potential was originally supplied by a holographic system [7,8]. This involved fabricating a plain Hall bar, without a gate, and cooling it to Helium temperatures. The sample was then illuminated with an interference pattern. This light would promote electrons locally from the donor states to the 2DEG, hence creating a periodic modulation of carrier concentration.

This was quickly followed by a striped metal gate on the surface of the wafer [9]. A voltage was applied which reduced the density of the buried 2DEG in a periodic manner and the effects of this studied. Previously very small periods (~60nm) have been obtained using metal gates but with small potential magnitudes [10]. A further problem with metal gates is continuity. If the metal is not continuous across the whole superlattice then regions without any modulation can be created. This is a particular problem when it comes to very thin metal in short period superlattices.

It was noted a few years ago in Glasgow [11] that additional effects were seen beyond those of the potential supplied by the metal gate on the samples used. It was discovered that, as the sample cooled, the gate thermally contracted at a different rate to the underlying semiconductor. This produced elastic distortion and strain, which then coupled to the 2DEG through both the deformation and piezoelectric potentials. The deformation potential arises due to the fact that compressing or expanding a semiconductor alters its band gap. Thus this will affect the local electron density. The piezoelectric effect is due to the compression or expansion changing the relative distances between lattice atoms and causing a bulk polarisation to develop. For example, in the [111] direction of the crystal structure a line can be drawn that passes through planes of all Ga ions and all Al ions. Hence, if the crystal is compressed along the [111] direction the lengths of the bonds joining these planes are changed, and they develop additional dipole moment. The result is a bulk polarisation, and leads to bound charge density, and an effective electric field and modulation of the electron density. Due to the symmetry requirements of the piezoelectric effect the magnitude of the potential formed goes as $\sin 2\theta$, where θ is the angle from [010] to the current flow direction (see Fig. 2.6) in our samples, which were fabricated on a (100) surface [12].

The effect of the deformation potential was found to be small in comparison to the piezoelectric.

My project was to create a specialised stressor layer separate from the electrostatic metal gate, confirm that it modulates the 2DEG by means of the piezoelectric effect and see if it is possible to produce strong, short period modulation by this technique.

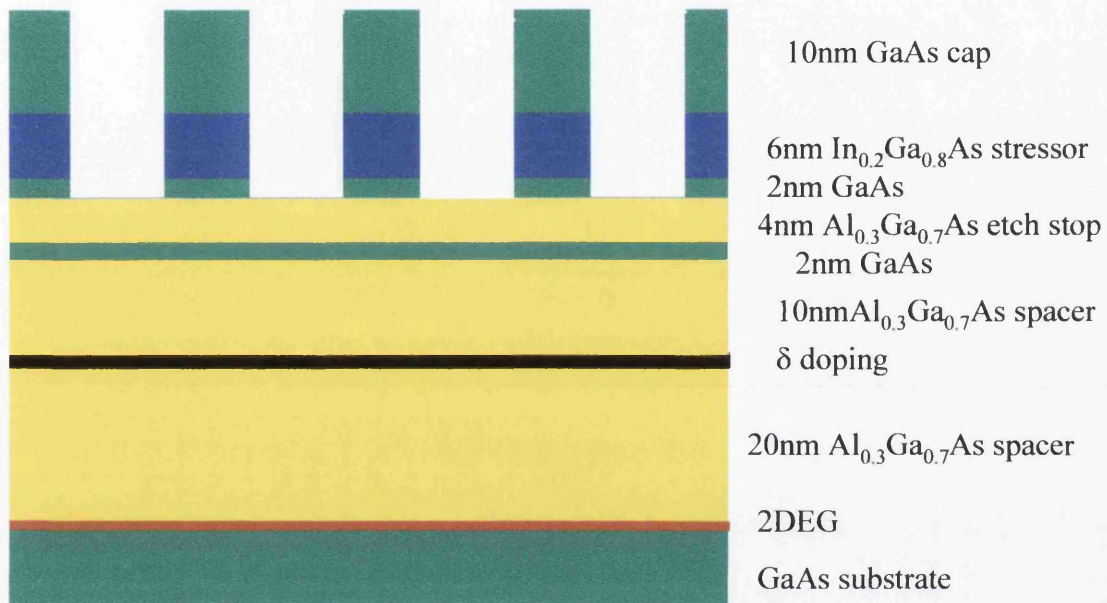


Fig. 2.5 A slice through the wafer A1246. The top three layers have been etched to produce the periodic effect.

Fig. 2.5 shows the layer system used. A special layer of $\text{In}_{0.2}\text{Ga}_{0.8}\text{As}$ was grown to act as the stressor as it has a larger lattice constant than GaAs. It is this lattice mismatch, rather than differential thermal contraction, that introduces the strain. The layer has to be kept thin. If the layer becomes too thick it is energetically favourable for dislocations to form, producing irregular surfaces and eventually causing the strained layer to relax [2,13]. This strained layer was then etched to produce a periodic strain as shown. This process, however, also introduces other periodic effects. The simple act of etching away the top layer of a semiconductor changes the conduction band diagram, i.e. an entirely new conduction band diagram can be drawn with different depth parameters. As the thickness of the cap layer and upper spacer reduce the assumption made in Eqn. 2.1, i.e. that E_{dd} is a constant, becomes invalid Thus, if Eqn. 2.1 is re-written to remove E_{dd} the following is obtained;

$$n_{2D} \left(\frac{c}{\epsilon_g} + \frac{s}{\epsilon_a} + \frac{u}{\epsilon_a} + \frac{a}{\epsilon_g} \right) = N_\delta \left(\frac{c}{\epsilon_g} + \frac{u}{\epsilon_a} \right) - \frac{\epsilon_0}{e^2} E_c(0) \quad (2.5)$$

where N_δ is the doping density and $E_c(0)$ is the conduction band offset at the surface [14]. All other parameters are as in Eqn. 2.1. As this shows, changing the thickness of the upper layers, by etching for example, will change the local carrier density. The deformation due to differing areas of stress translates into a small potential which can also change the local carrier concentration [15]. The piezoelectric effect acts in the same manner as the deformation potential but has been shown to be much larger [12]. It also has a directional component, the magnitude is proportional to $\sin(2\theta)$, where θ is the angle from [010] to the direction of current flow (positive towards [001]) [12,16] (Fig. 2.6). Further to these, if a metal gate is evaporated on top of the etched region, the metal will enter into the etched trenches. This then creates areas where the gate is closer to the 2DEG than on top of the ribs. These effects then combine to produce an overall modulation which is subject to a number of variables.

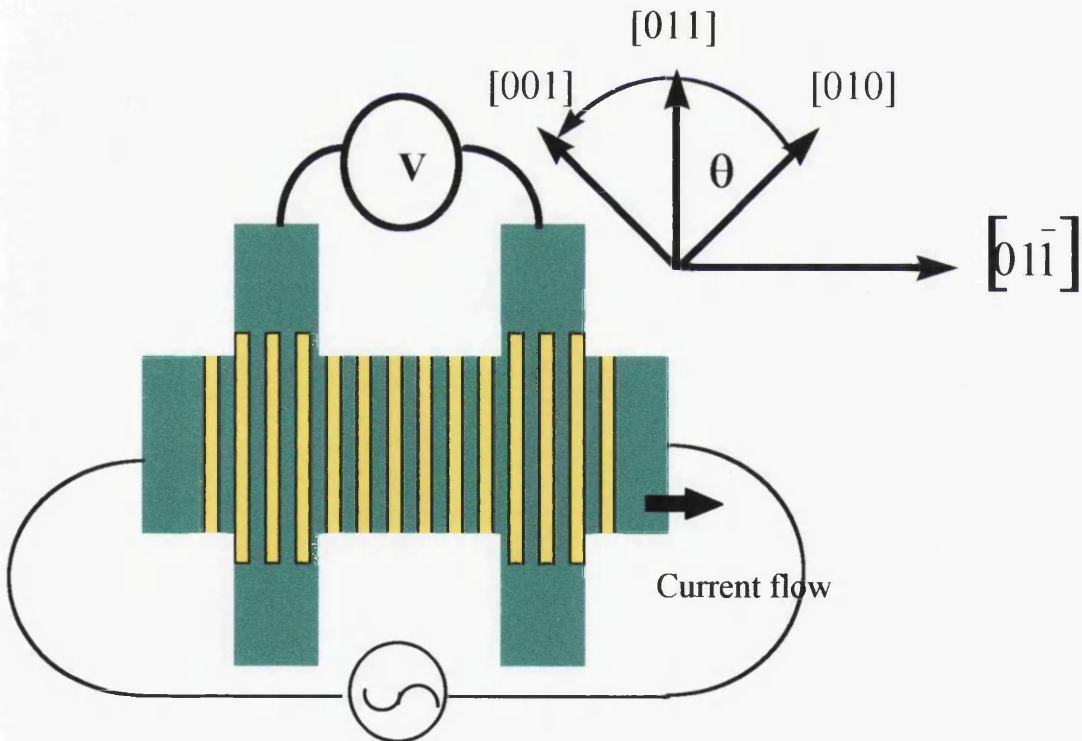


Fig. 2.6 Schematic of Hall bar with crystal directions indicated. $\theta = -45$ degrees in this example

To prove that the InGaAs was the **main** source of the modulation a control wafer was also grown at the same time as the InGaAs wafer. This contained an

equivalent set of layers except that the InGaAs was replaced by GaAs. Thus the 2DEG was at the same depth from any modulation. Also the patterning of both wafers was carried out simultaneously to ensure that both samples were identical.

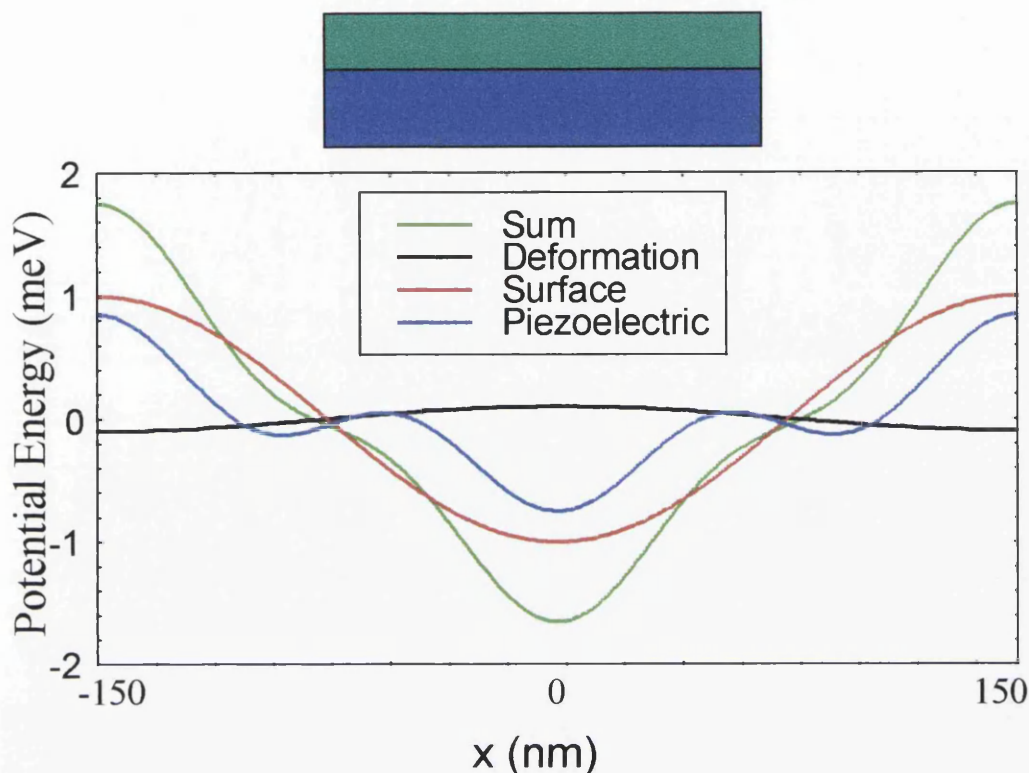


Fig. 2.7 Schematic diagram of the component parts of the electrostatic potential produced by an etched rib in an LSSL. Period 300nm, current flow direction [011].

The blue and green blocks represent the rib of a superlattice (see text)

Fig.2.7 is drawn for one rib of stressor (blue bar), surmounted by a GaAs cap (green bar), in an array. This array will then, theoretically, produce the potentials illustrated. The potentials produced via the surface, deformation and piezoelectric effect will then sum together to produce the green trace. It should be noted that this is only one cell of the full array created by the superlattice. If the superlattice rib was to lie at ninety degrees to this, in relation to the crystal direction [010], then the piezoelectric potential would be of opposite sign due to the $\sin(2\theta)$ term. Thus the sum would be much smaller. At forty five degrees to this in either direction the piezoelectric term is equal to zero.

The depth at which the 2DEG lies will affect the modulation. Larkin et al [12] showed that both the strength and sign of the potential depends upon the ratio of l/d , l

being the period of the modulation and d the depth of the 2DEG. $d = c + u + s$ from Fig. 2.1. As Fig. 2.8 shows, the sign is predicted to change as the period gets larger, with harmonics crossing the axis at larger values of period. Changing the depth of the 2DEG will change the point at which the traces meet the axis, as well as the magnitude of the potential at the 2DEG. It is important to have the ribs as close to the electrons as possible to make the magnitude of the potential large. Unfortunately, the dopant atoms are a source of scattering and hence reduce the mobility of the 2DEG the closer they are. Thus a balance must be struck between closeness for good transmission of harmonics and distance for limited ionic impurity scattering.

The ratio of the width of the rib to the trench in Fig. 2.8 is 1:1. If this is altered then the crossing point does not change but the relative sizes of the different harmonics do. It should thus be possible to alter this rib to space ratio to encourage certain harmonics. Thus the harmonic content seen is heavily dependent on fabrication accuracy.

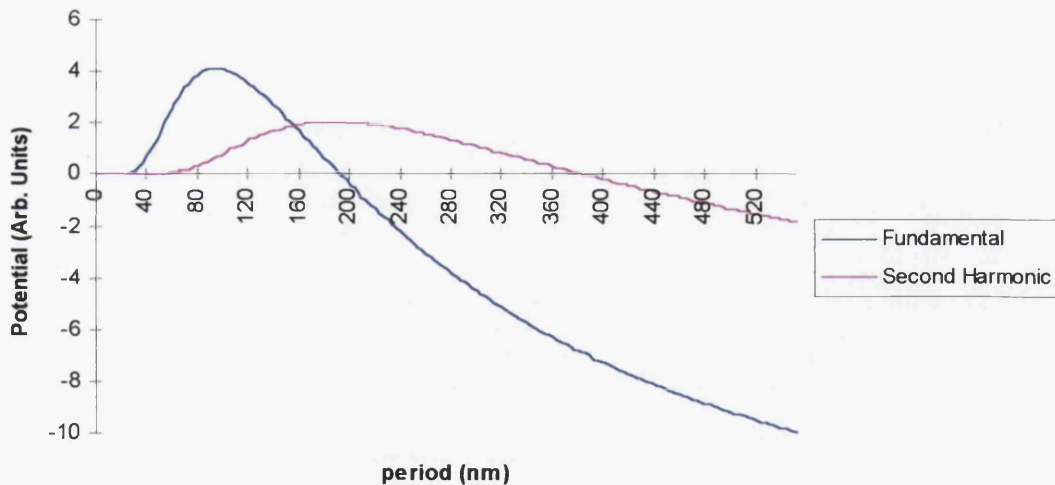


Fig. 2.8 Theoretical calculations of magnitude of the piezoelectric potential versus period of LSSL for the first two harmonics. $d=43\text{nm}$, $c=16\text{nm}$, Trench:Rib=1:1, c,d as in Fig. 2.1, Hall bar current flows in $[01\bar{1}]$ direction

2.5 Periodic Modulation in Magnetic Fields

If a one-dimensional periodic modulation of the electron concentration is set up an interesting set of effects can be seen in varying magnetic fields. The commensurability between the dimensions of the cyclotron orbits and the period of the modulation is very important.

The semi-classical argument by Beenaker goes as follows [17]. When a sea of electrons is subject to both an electric and a magnetic field then a drift velocity at right angles to both is created. As the electric field oscillates in the periodic potential of a superlattice this drift velocity will oscillate in direction. If an average is taken over a cyclotron orbit, then it can be shown that that as the cyclotron orbit changes with B field so the average drift velocity changes. This leads to a change in the lateral drift velocity and hence lateral conductivity. This results in the observed change in the longitudinal resistance. These resistance changes are known as Commensurability Oscillations (CO).

The cyclotron radius (R_c) is the radius of an orbit of a free electron in a magnetic field;

$$R_c = (2\pi n_{2D})^{\frac{1}{2}} \frac{h}{2\pi eB} \quad (2.6)$$

where n_{2D} is the carrier concentration, B is the magnetic field, e is the fundamental charge on an electron and h is Planck's constant.

The CO troughs are found at cyclotron radii of;

$$R_c = \frac{a}{2} \left(k - \frac{1}{4} \right) \quad (2.7)$$

k being the CO index and a the period of the potential. The magnitude of these oscillations was derived by Beenaker [17] and is shown here;

$$\frac{\delta\rho}{\rho} = \left(\frac{eV_0}{E_F} \right)^2 \frac{l^2}{aR_c} \cos^2 \left(\left(\frac{2\pi R_c}{a} \right) - \frac{\pi}{4} \right) \quad (2.8)$$

where $\delta\rho$ is the peak to peak change in the resistance, V_0 is the magnitude of the periodic potential, l is the mean free path, ρ is the zero field resistance and E_F is the Fermi energy.

Further resistance changes can also be seen at extreme low and high magnetic fields. At low fields the Lorentz force supplied to the electrons is small in comparison to the magnitude of the electrostatic potential and so the progress of the electrons is

impeded. The electrons then stream laterally in this magnetic field. This causes the resistance to rise with increasing magnetic field [18]. These streaming orbits become closed cyclotron orbits past a “magnetic breakdown” point. This point occurs when the electrostatic force is equal to the magnetic force. This point can be calculated as;

$$B_0 = \frac{2\pi V_0}{av_F} \quad (2.9)$$

where V_0 is the size of the potential, v_F is the Fermi velocity and a is the period of the potential [19]. The streaming orbits do not become closed instantaneously. There is a rapid decay of the streaming orbits, prior to the breakdown point, which can be seen as a decrease in the resistance. However, in our samples, this decay is not seen, due to other, higher field, effects overlapping this region.

At high magnetic field a rise in resistance is also seen. It is proportional to the square of the magnitude of the periodic potential in the following way;

$$\frac{\delta\rho}{\rho} = 1 + \left(\frac{eV_0}{E_F}\right)^2 \omega_c^2 \tau^2 \quad (2.10)$$

where $\tau = \frac{l}{v_F}$ [19]

It is also heavily modified by any Shubnikov-de Haas oscillations present. Both these effects are known as Positive Magnetoresistance (PMR) effects.

The above arguments have assumed that the commensurability structure is a simple semi-classical effect. It is possible, however, to perform a quantum mechanical analysis of the periodic modulation [20]. This gives a similar magnetoresistance result for a first order perturbation. It is interesting to note that the COs manifest as a modulation of the width of the Landau Levels, as the magnetic field is varied. The LLs are broadened at a resistance maximum and are unmodulated at a resistance minimum. Further broadening terms, such as random impurity scattering, can be added into this analysis, making it a very powerful tool.

As the quantum mechanical SdH oscillations are very temperature dependant most work has been done at temperatures sufficient to smear out these SdH oscillations and leave the CO behind. However, little has been done to study the interactions between the two types of oscillation at low temperatures. A simple explanation of what happens is that the SdH oscillations have their average value

modulated by the CO. Thus the SdH amplitudes are unaffected but their absolute value in resistance is shifted depending on the underlying CO. Chapter 7 will cover work designed to study this particular area.

2.6 Estimation of potentials

There are two methods by which we can calculate the magnitude of the potentials used in these experiments. As the magnetic energy must be equivalent to the modulation energy at the PMR peak it's position in magnetic field can be used to estimate the potential. It should be noted that the "magnetic breakdown" point that Eqn. 2.6 refers to occurs just after the magnetoresistance peak, when all the open orbits have become closed. In experimental traces it is not possible to discern this point. Thus the peak itself is used. This will introduce some error.

With equations (2.6) and (2.7) the carrier concentration can be calculated from the position of a trough (a useful check against the value found from the SdH oscillations) and, if combined;

$$\frac{a}{2} \left(k - \frac{1}{4} \right) = \left(2\pi m_{2D} \right)^{\frac{1}{2}} l_m^2 \quad (2.11)$$

and then rearranged (for arbitrary CO oscillation number k);

$$\frac{(4k-1)a}{8} = \frac{v_F m_c}{eB} \quad (2.12)$$

If this is then combined with (2.9);

$$\frac{eV_0}{E_F} = \frac{8B_0}{(4k-1)\pi B} \quad (2.13)$$

The other method makes use of Beenaker's perturbation calculation which relates the magnitude of the CO oscillations to the magnitude of the potential. Beenaker showed that the longitudinal resistance varies with magnetic field in the following way;

$$\frac{\delta\rho}{\rho} = \left(\frac{eV_0}{E_F}\right)^2 \frac{l^2}{aR_c} \cos^2\left(\left(\frac{2\pi R_c}{a}\right) - \frac{\pi}{4}\right) \quad (2.14)$$

where $\delta\rho$ is the peak to peak change in resistance, ρ is the zero field resistance, l is the mean free path, eV_0 is the magnitude of the potential and E_F is the Fermi energy. The magnitude of a first order potential can be calculated from the change in peak to peak resistance at an integer value of k , the CO index in the following way;

$$\frac{eV_0}{E_F} = \sqrt{\frac{\delta\rho}{\rho} a R_c} \frac{1}{l} \quad (2.14a)$$

where $\delta\rho$ refers to the peak to peak amplitude of the measured oscillation.

This then allows comparison as a check on the accuracy of the two methods. However if harmonics are present in the electrostatic potential then they will add in to the value obtained from the PMR method as follows $V_0 = V_1 + 2V_2 + 3V_3 + \dots$. Thus a difference between the two methods can often be attributed to this.

Both these methods are used in tandem to allow cross checking. It should be noted that the CO method is based on a perturbation calculation and so only “small” magnitudes should be included.

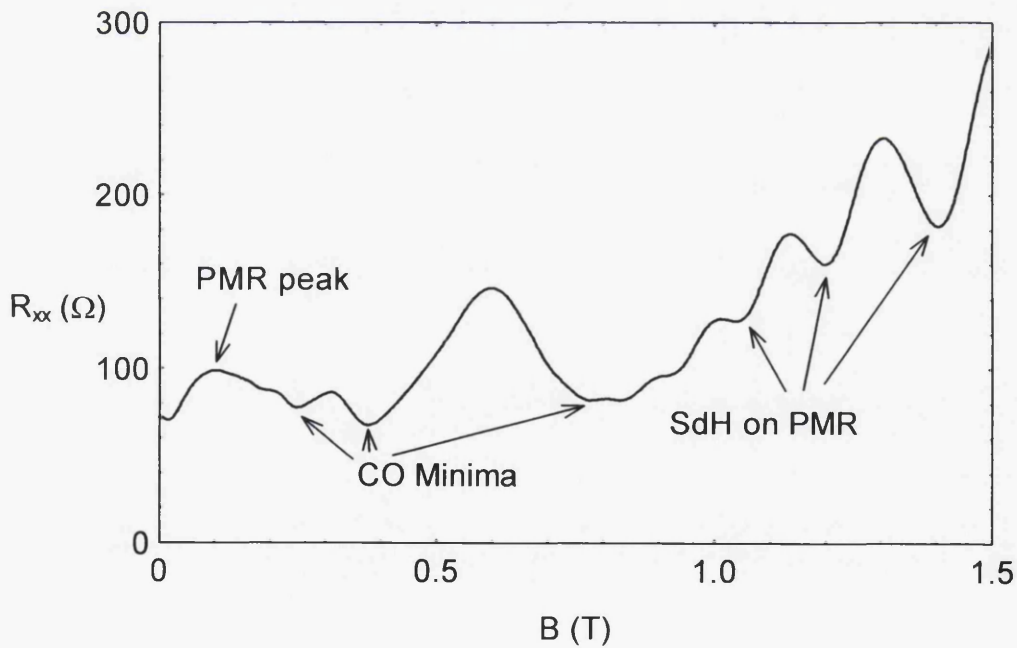


Fig. 2.9 Sample trace from sample 9, period 300nm, current flow direction [011], taken at 5K with zero bias on the gate

If a periodic potential is present then the features shown in Fig. 2.9 should appear in an R_{xx} against B trace. There will be a PMR peak at low fields ($<0.3T$). This is due to the open, streaming orbits described earlier. As the magnetic field increases the cyclotron orbit becomes commensurate with the potential period. Thus CO appear. As the cyclotron orbit is initially large the oscillations are small. This comes from the Beenaker equation (2.14) where $\delta\rho$ is inversely proportional to R_c . The oscillations then increase as the radius contracts until the radius is equal to $\frac{3}{8}$ of the period (from equation (2.7) for $k = 1$). This gives the large minimum at $\sim 0.8T$. In this example the SdH oscillations are becoming visible at this field and so they begin to modulate the CO. As the field rises further the sample moves into the Geim PMR region. It is heavily modulated by SdH oscillations, however, and the interplay between these two effects is not fully understood.

The magnitude of the potential can be calculated in a number of ways. As described earlier, the relative positions of the PMR peak and the $k=2$ CO trough give one estimate of the magnitude. Thus, from a trace such as the one above, positions can be measured and the potential calculated. Unfortunately, if the SdH oscillations are large they can overlay the $k=2$ minimum. This can add errors to the measurement of position. Also, if the potential is large, the two points become very close together. Thus it can be difficult to confidently say that the $k=2$ minima is not being offset by the PMR peak. The size of a CO peak, i.e. $\delta\rho$, is also an indication of the potential magnitude. However, this can also be modified by similar factors. SdH oscillations can make it hard to say at which point a peak or trough occurs and a large potential can cause most of the oscillations to be drowned out by the PMR, leaving nothing to measure. Also, a very small potential gives small oscillations. These can introduce large measurement errors when the peak heights are measured from the experimental trace.

References

- [1] H.P. Myers. *Introductory Solid State Physics*. Taylor and Francis (1991)
- [2] J.H. Davies *The Physics of Low-Dimensional Semiconductors* Cambridge University Press (1998)
- [3] A.R. Long, J.H. Davies, M. Kinsler, S. Vallis, M.C. Holland. *Semicond. Sci. Technol.* **8** 1581 (1993)
- [4] K.v. Klitzing, G. Dorda, M. Pepper. *Phys. Rev. Lett.* **45** 494 (1980)
- [5] R. Landauer. *IBM J. Res. Dev.* **1** 223 (1957); **32** 306 (1988)
- [6] M. Büttiker. *Phys. Rev. Lett.* **57** 1761 (1986)
- [7] D. Weiss, K. von Klitzing, K. Ploog, G. Weimann. *Europhys. Lett* **8** 179 (1989)
- [8] R.R Gerhardt, D. Weiss, K. von Klitzing. *Phys. Rev. Lett* **62** 1173 (1989)
- [9] R.W. Winkler, J.P. Kotthaus, K. Ploog. *Phys. Rev. Lett.* **62** 1177 (1989)
- [10] S. Vallis PhD Thesis Univ. Of Glasgow (1996) {Maybe actual paper?}
- [11] R. Cuscó, E. Skuras, S. Vallis, M.C. Holland, A.R. Long, S.P. Beaumont, I.A. Larkin, J.H. Davies. *Superlattices Microstruct.* **16** 283 (1994)
- [12] I.A. Larkin, J.H. Davies, A.R. Long, R. Cusco. *Phys. Rev. B* **56** 15242 (1997)
- [13] A.G. Cullis, A.J. Pidduck, M.T. Emeny. *Journal of Crystal Growth* **158** 15 (1996)

- [14] E. Skuras, M.C. Holland, C.J. Barton, J.H. Davies, A.R. Long *Semicond. Sci. Technol.* **10** 922 (1995)
- [15] J.H. Davies, I.A. Larkin, *Phys. Rev. B* **49** 4800 (1994)
- [16] E. Skuras, A.R. Long, I.A. Larkin, J.H. Davies, M.C. Holland *App. Phys. Lett.* **70** 871 (1997)
- [17] C.W.J. Beenaker *Phys. Rev. Lett.* **62** 2020 (1989)
- [18] P.H. Beton, E.S. Alves, P.C. Main, L. Eaves, M.W. Dellow, M. Henini, O.H. Hughes, S.P. Beaumont, C.D.W. Wilkinson *Phys. Rev. B* **42** 9229 (1990)
- [19] A.K. Geim, R. Taboryski, A. Kristensen, S.V. Dubonos, P.E. Lindelof. *Phys Rev. B* **46** 4324 (1992)
- [20] C. Zhang, R.R. Gerhardts. *Phys. Rev. B* **41** 12850 (1990)

Chapter 3 Fabrication

3.1 Introduction

All of the Lateral Surface Superlattices were fabricated on top of Hall bars (Fig. 3.1). The Hall bar geometry allows measurement of both longitudinal and transverse resistance. It is also reasonably simple to make and devices of this type have been fabricated in Glasgow for some time. Current can be passed down the length of the Hall bar and the voltages are then measured as shown. The two extra contacts are for any gate which may be deposited. In the case of my samples, the Hall bar was patterned in the region containing the voltage probes and then a flat gate was evaporated on top of the whole active region.

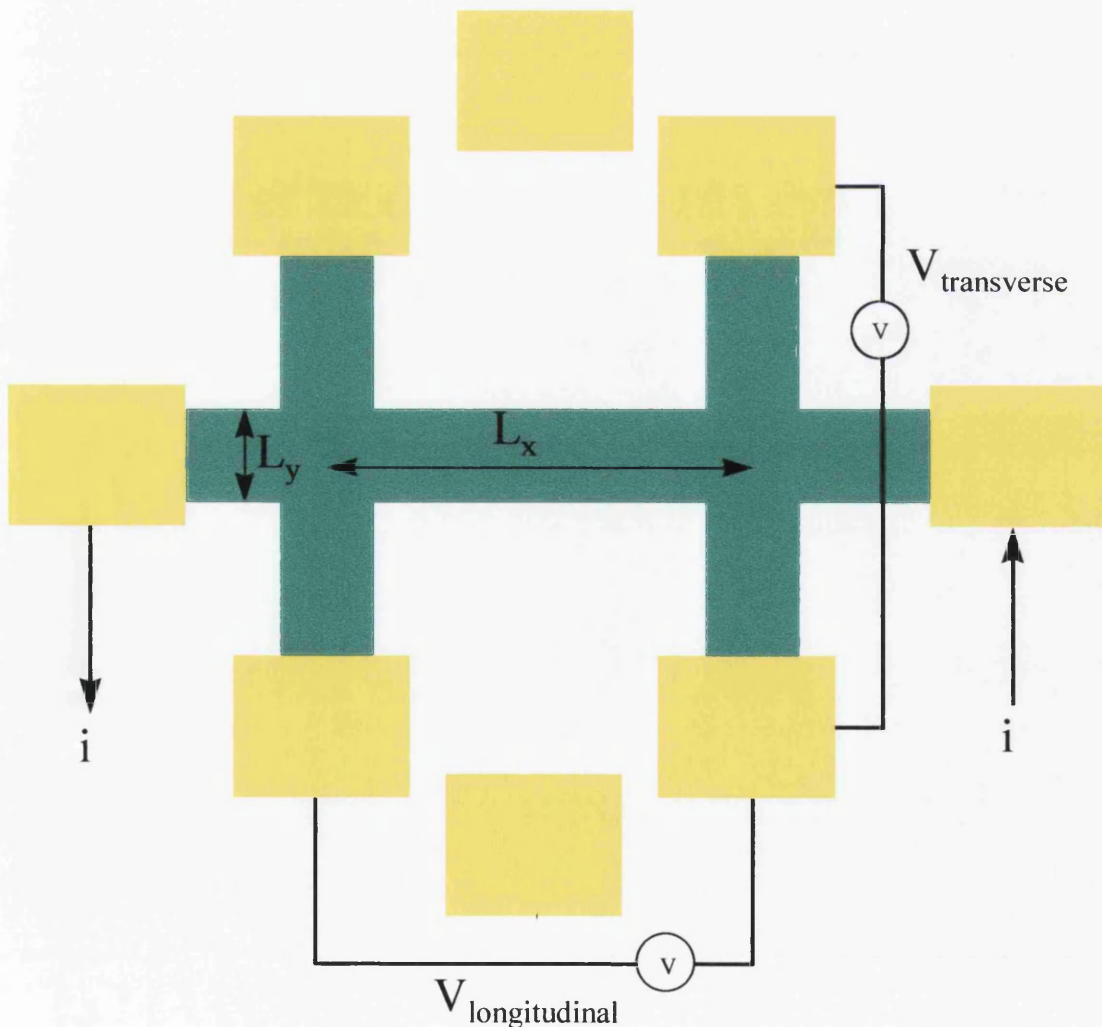


Fig. 3.1 The basic Hall bar

All the samples used in these experiments were fabricated in the Department of Electronics and Electrical Engineering at the University of Glasgow. Much help and advice was supplied by the technical staff in the Ultra Small Structures Lab where the majority of the work was carried out.

3.2 Facilities

The majority of the work was carried out in a class 10,000 clean room. This contained two class 100 fume cupboards, two baking ovens, a Plassys Metal Evaporator and access to the beamwriter. The department has a Leica Cambridge Beamwriter EBP5. This works by projecting an electron beam onto the wafer. The beam can be moved by magnetic coils such that it draws out the required pattern. This pattern is drawn in light-sensitive resist which undergoes a chemical reaction upon illumination. The illuminated resist will then dissolve in a mixture of IsoPropyl Alcohol (IPA) and Methyl isoButyl Ketone (MiBK) leaving a patterned mask for further processing. A second clean room in the department has a Rapid Thermal Annealer (RTA) which is used for the annealing of Ohmic contacts. There are also two Hitachi Scanning Electron Microscopes, a DC probing station, a wafer scribe and a gold wire bonder available.

All wafers used in these experiments were grown by Molecular Beam Epitaxy (MBE), also in the Department of Electronics and Electrical Engineering.

3.3 Fabrication Techniques

All the wafers used in these experiments were of a similar nature. They consisted of a simple delta doped heterojunction, as had been used on many occasions by others in the group, with a novel $\text{In}_{0.2}\text{Ga}_{0.8}\text{As}$ layer near the surface to introduce stress. The “stressor” layer structure is as follows;

Surface

10nm GaAs

6nm $\text{In}_{0.2}\text{Ga}_{0.8}\text{As}$

2nm GaAs

4nm $\text{Al}_{0.3}\text{Ga}_{0.7}\text{As}$

2nm GaAs
10nm Al_{0.3}Ga_{0.7}As
 δ -doping ($3.5 \times 10^{12} \text{cm}^{-2}$)
20nm Al_{0.3}Ga_{0.7}As
GaAs channel and substrate

In addition a “control” wafer was also grown, at the same time. This had an identical set of layers, except that the “stressor” InGaAs layer was replaced with a pure GaAs layer. Thus, it would be possible to fabricate samples on this second wafer, any differences between the two being attributed to the stress produced.

When received these wafers were cleaved by a diamond tipped scribe into quarter wafers for ease of fabrication. They were then cleaned by ultrasound in acetone for five minutes and rinsed in Iso-Propyl Alcohol (IPA) for a further five minutes with ultrasound and dried with compressed nitrogen gas. This cleaning procedure would be carried out before fabrication of each layer as contamination of the surface could impair adhesion of resist to the surface or distort the pattern required. The sample had a Poly-Methyl Methacrylate (PMMA) resist spun on it and was submitted to the beamwriter technicians.

The usual method for generating the PMMA layer was to spin a thick layer of the resist, bake it for a short time to prevent mixing with a second layer, and then spin the second layer which was baked for longer (Fig. 3.2). The baking causes the resist to harden, allowing the mask produced to be rigid. After the resist had been baked it was submitted to the beamwriter. After writing the sample was then developed. This involved dipping the samples in a mix of IPA and Methyl iso-Butyl Ketone (MiBK), known as a developer. The exact ratio of these two, and the length of time the sample would be immersed, depended upon the job in hand. The electron beam generates a pattern by reducing the PMMA to smaller molecules. These are small enough to be dissolved away by the developer, leaving behind the undeveloped resist. This can then be used as a mask for metallisation and wet or dry etching.

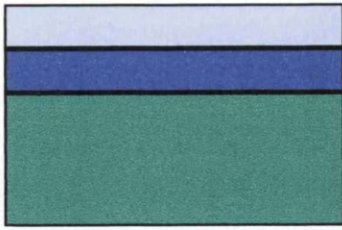
Metallisation was carried out in the Plassys evaporator. The sample was placed in a vacuum and metal was evaporated over the visible surface. Once metallised the sample was placed in warm acetone. This dissolved the unexposed mask resist, taking

the excess metal with it. Thus the desired pattern in metal is left behind. This process is called lift-off. For etching, wet or dry, the sample is merely etched to the required depth and then the mask resist is removed with warm acetone as above.

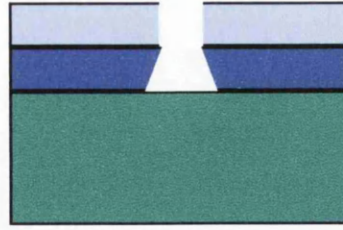
The bi-layer structure was most important where a metal pattern was to be deposited. It is desirable that the lower layer dissolves slightly quicker during developing. This creates an overhang at the edge of the pattern. Hence the lower layer is spun with a lighter resist, which is broken up more by the electron beam, and hence a slightly larger feature is created in the lower area, creating the desired overhang. When the metal is evaporated it will fill the exposed area but will not move under this overhang. Thus, when removing the excess metal and resist later the acetone is free to attack the PMMA from the side without any metal being in the way. In the case of etching it is more important to have straight edges to the resist mask. This will more effectively guide the etchant to the wafer surface. Thus a single layer, or perhaps two layers of similar material, are used.

The resists available were of two types. They were known locally by the manufacturers names and were Aldrich (Ald) and Elvacite (Elv). They had an average molecular weight of 120,000 and 360,000 respectively. The polymers were dissolved in chlorobenzene or xylene to a number of different percentage weight contributions. The higher the percentage of PMMA in the solvent the thicker becomes the resist when spun on to a wafer.

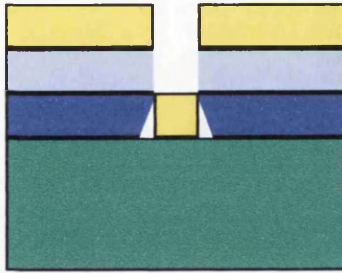
To expose the resist in the beamwriter, for each layer of the process, a separate "pattern" and "job" file were required. These computer files instruct the beamwriter as to its task. Initially a CAD package called Wavemaker (Wam) was used to create the designs. Each layer was then analysed by a program called CATS to produce the pattern file. A second program, BWL, was used to set parameters such as dose and sample position. This is the job file.



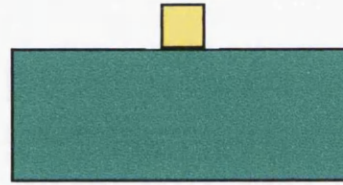
a) Wafer with resist bi-layer



b) Wafer after patterning in beamwriter and developing



c) After metallisation



d) After lift-off, the finished product

Fig. 3.2 The lift-off process

3.3.1 Marker layer

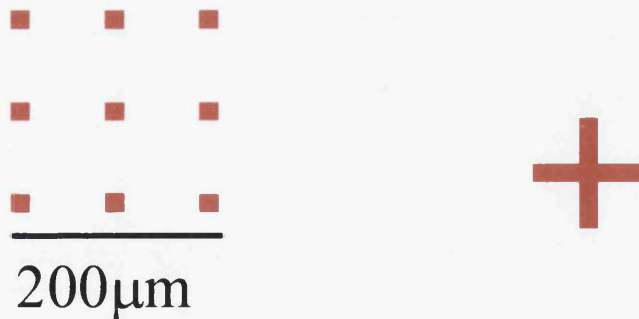


Fig. 3.3 Wam pattern for Alignment layer.

Alignment marks are required to ensure that all the layers involved correspond spatially as they should. These were initially laid down as part of the following ohmic layer. It was found that the metal involved did not survive the following annealing processes sufficiently well to give good alignment. Hence they were produced

separately using a different metal layer structure, which survives the annealing with a better edge definition, as follows.

A resist bilayer of 15% Ald and 4%Elv was spun at 5000 rpm. The Ald was baked for one hour before the Elv was spun, which was baked for two hours before submission. The marks were written with a 160nm spot size, 100nm step size at a beam energy of 50kV. They were developed with 1:1 MiBK:IPA. The following metal layers were then evaporated onto the sample (Top to bottom);

150 nm Au

30 nm NiCr

The resist was then removed with warm acetone leaving behind the markers. If a good, clean, crisp edged set of markers are produced then nanometre scale alignment can be achieved. The cross is used by the beamwriter technicians to roughly locate the markers with the minimum of exposure. This helps to maintain the clean markers and thus improve the alignment of later layers.

3.3.2 Ohmic contacts (Ohmics)

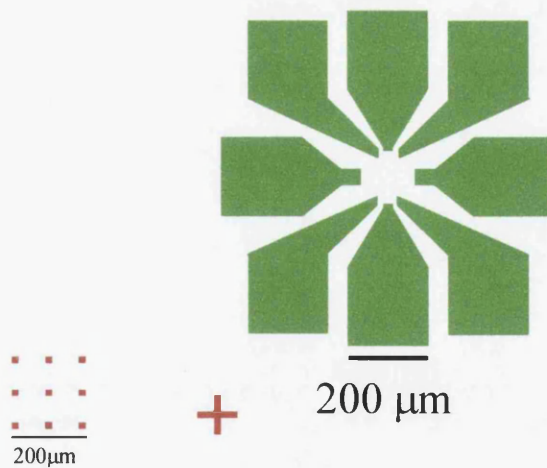


Fig. 3.4 Ohmic pattern in Wam.

This layer uses the same resist layers, spot size and step size as for the marker layer. It must be aligned carefully to the alignment marks, as must all subsequent layers, to ensure that all patterns overlap in the correct manner. The evaporated metal is however of a different structure;

250 nm Au

80 nm Ni
130 nm Au
120 nm Ge
8 nm Ni

The resist is also removed in the same way as above. Once the metal is in place it must be annealed. Annealing involves heating the wafer to 360° C in the RTA for 60s. This drives the deposited Ni and Ge into the wafer creating an electrical contact between the 2DEG and the thick gold pads on the surface. After annealing this electrical contact was tested using a D.C. probe station. This would give a two-terminal resistance measurement of approximately 1000Ω between any two contacts if the annealing was successful.

3.3.3 Isolation

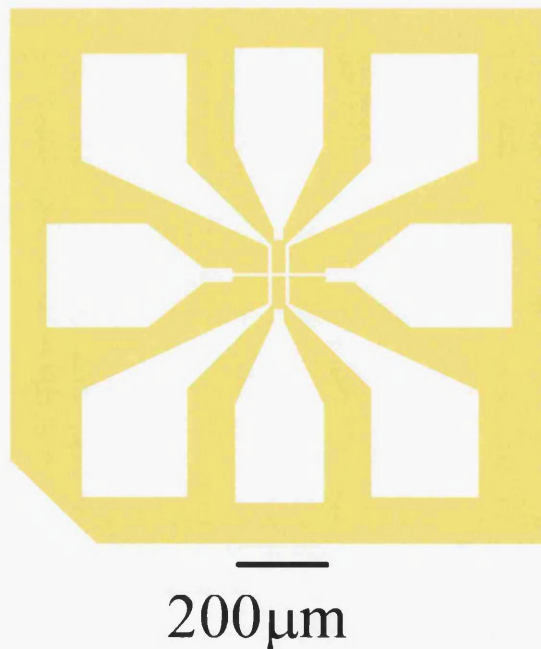


Fig. 3.5 Wam design of the isolation layer.

The active area of the Hall bar that we wish to study has to be electrically isolated from its surroundings. Thus the pattern shown is written in the same resist as before but with a spot size of 300nm and a step size of 200nm. A different spot and resolution were required as it was discovered that the backscattering of electrons

became a problem with the original resolution and spot size. This led to a narrowing of the channel in the centre which would complicate the geometry. The exposed area is etched with a solution of 100:2:0.75 of $\text{H}_2\text{O}:\text{NH}_3:\text{H}_2\text{O}_2$. This etches the wafer at 100nm/min and thus the sample is dipped in the solution for 30 s. This leaves a narrow channel of width $10\mu\text{m}$ for the 2DEG, which can be completely covered by the superlattice. The sample can now be measured with the D.C. probe station again and the two-terminal resistance should have increased by a factor of 10.

3.3.4 Superlattice

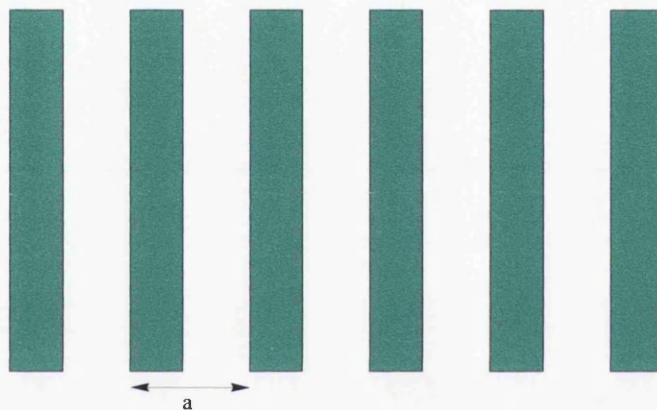


Fig. 3.6 Schematic design of a 1:1 mark:space Superlattice. a is the period of the LSSL, typically of order 100nm in this Thesis.

The superlattices have to be written using a 100kV beam. This gives a higher resolution for small features due to reduced backscattering. A single layer of resist is used, as the bilayer undercut is not required. The following parameters were used in the superlattices produced for this thesis;

Table 3.1: Parameters of superlattices produced for this thesis.

Period (nm)	Written Mark:Space (nm)	Spot Size (nm)	Step Size (nm)	Resist	Dose (μC)
300	130:170	12	10	4% Ald 4% Elv	590
200	85:115	12	5	4% Elv	570
100	35:65	12	5	4%Elv	700

The superlattices are developed with 3:1 IPA:MiBK developer. They are only dipped in the solution for 30s as little resist has to be removed. Once the superlattice has been developed the sample is handed over to a dry etch technician with instructions as to type of etchant and time in the plasma.

The dry etching for these samples was done in a SiCl_4 plasma for 60s in the case of the 300nm LSSL and 90s in the case of the 100nm LSSL. This etches the required 16nm into the wafer. Unfortunately the plasma has an induction time of approximately 30s. This time is not constant and thus introduces a significant error into the fabrication. Thus, when fabricating, a number of different etch times were tried on test pieces and whichever gave a reasonable strength of modulation was assumed to be the correct time. When full devices were produced, all samples to be etched for a specific time were etched in the same machine run to ensure consistency. A further problem is that the indium does not fully dissolve in the plasma. Thus it can redeposit on the surface of the wafer or indeed in the etched regions. When the sample is returned the resist is removed by the cleaning procedure outlined above.

On a number of occasions a wet etch technique was used. In the initial test runs the etchant used for the isolation layer was used. This produced reasonable results, but with a very short etch time, of the order of 15s. This was deemed too prone to error, and the dry etching was pursued. A period of inconsistency in the dry etch machine was encountered in early 1999, which prompted a re-investigation of wet etching. This was carried out by another PhD student, Suja Chowdhury, and the last set of samples were produced using this technique.

The etch contained 3:1 H₂O₂:Citric Acid, plus a wetting agent to ensure the etch fully reaches into the narrow mask gaps. The etch time for this etch was of the order of 90s and so a greater accuracy was expected.

3.3.5 Gate

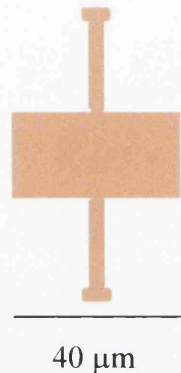


Fig. 3.7 Gate pattern as designed in Wam.

Finally a large flat metal gate is produced. This uses the same resist and beamwriter recipes as the marker and ohmic layers. A thin layer of metal (12 nm Ti and 15 nm Au) is evaporated by the Plassys over the active region.

3.4 Imaging

During the fabrication process it is necessary to image the patterns on a number of occasions. Layers such as the isolation and ohmic layers can easily be seen in an optical microscope. However, to image the LSSL it is necessary to use higher resolution methods. Thus, in the initial stages a Scanning Electron Microscope (Hitachi S900) is used. This gives sufficient resolution to allow the imaging of the pattern in the Elv resist. This allows checking to ensure that the pattern written is the pattern intended. As this uses a high energy electron beam the pattern is eventually destroyed by the imaging. Thus, unfortunately, samples intended for measurement cannot be imaged with an SEM during fabrication. Test samples must be exclusively produced.

After a sample has been measured it is useful to examine it in the SEM. This allows us to confirm the period and, possibly, the etch depth of the LSSL. However, it can be difficult to accurately gauge the depth. Thus the samples were also examined in an Atomic Force Microscope (Figs. 3.8 and 3.9).

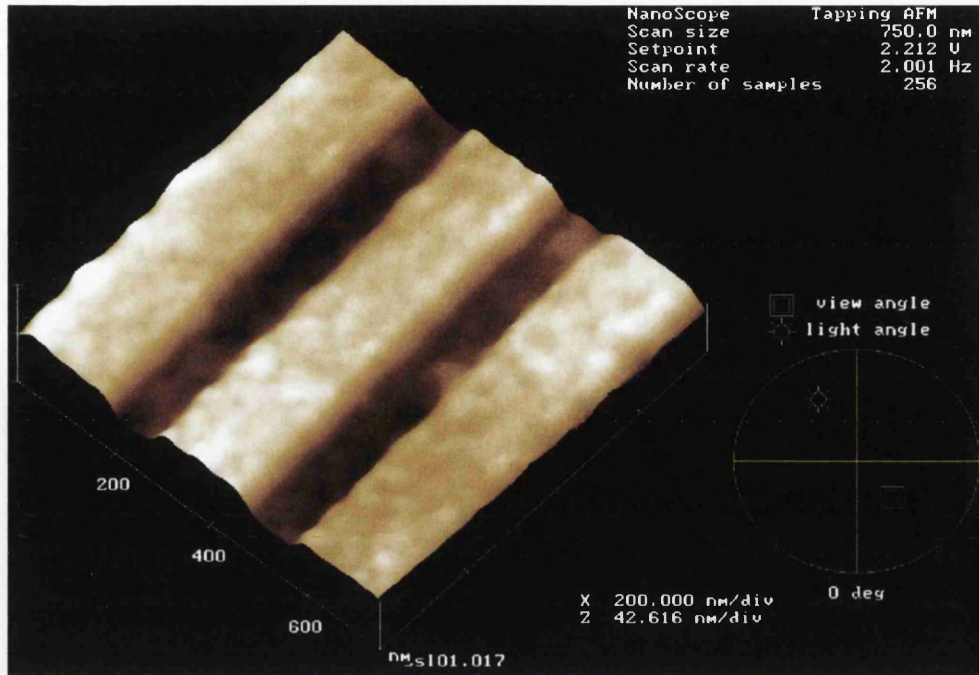


Fig. 3.8 AFM image of 300nm LSSL

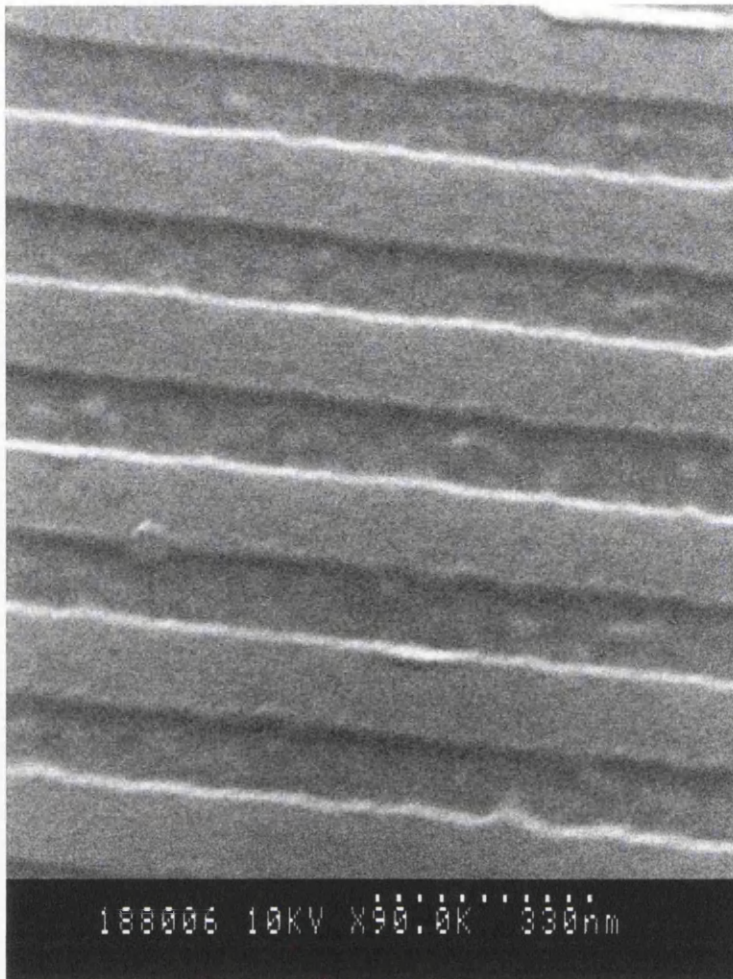


Fig. 3.9 SEM image of 300nm LSSL

It should be noted that in both images it is possible to see a roughness in the base of the trenches. This is believed to be indium re-deposition as mentioned earlier. If this is true then this could lead to random potential fluctuations in the finished LSSL.

3.5 Packaging

Once the samples have been produced they must be packaged in a manner suitable for measuring (Fig. 3.10). Thus they are cleaved into groups of two and attached to a ceramic package by means of silver epoxy. The ceramic package has eighteen gold pads around the edge which are connected to further pads on the base. The gold wire bonder can be used to electrically connect the ohmic contacts of the sample to the pads on the package and thus connect the sample to the outside world.

The pads on the outside of the chip are then connected to the measurement rod as described later.

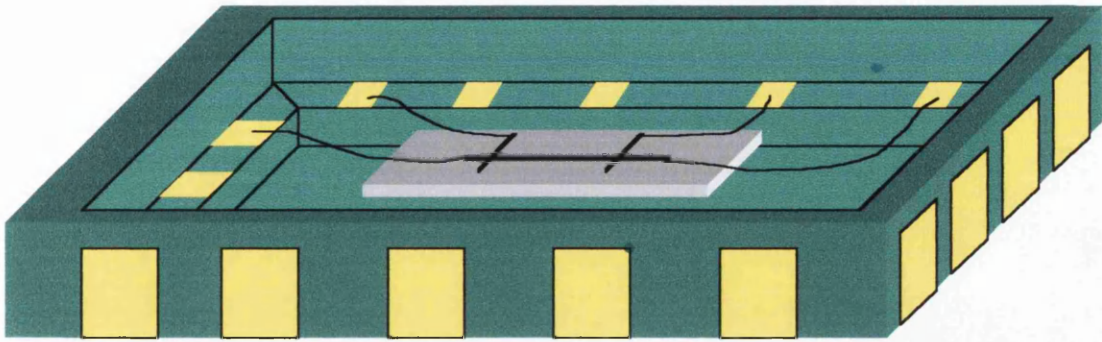


Fig. 3.10 Schematic of device in chip packaging. Only one device is illustrated for clarity.

Table 3.2 Samples studied for this thesis

Sample	Date	LSSL period (nm)	Mark:Space (as written)	Etch time (s)	Gate Voltages (V)	Temperatures (K)
1	Jan 1998	----	----	----	0 to -0.5	1.6
2	Jan to Feb 1998	300	~ 1:10	12 wet	----	1.6, 5.1, 10.2
3	Jan to Feb 1998	300	~ 1:10	17 wet	----	1.5
4	Jan to Feb 1998	300	~1:10	60 dry	----	1.6
5	Feb to March 1998	300	~1:10	80s dry	-0.3 to 0.3	1.6, 5.1, 10.2
6	Jan to Feb 1998	300	~1:10	90 dry	----	1.6, 5.1, 10.2, 20, 30, 40, 50, 75
7	Feb to March 1998	300	~1:10	120 dry	----	1.6
8	March to June 1998	300	1:1	90 dry	0.5 to 0.6	1.6
9	March to June 1998	300	1:1	60 dry	-0.3 to 0.3	1.6, 5.2, 10.2, 25, 50, 75
10	July 1998	100	1:1	60 dry	-0.3 to 0.3	1.6
11	July 1998 to May 1999	100	1:1	90 dry	-0.3 to 0.3	0.045, 0.11, 0.22, 0.34, 0.88, 1.6, 5.1, 10.2, 25, 50, 75, 100, 125, 150
12	July 1999	200	1:1	90 wet	0 to 0.6	1.6

Chapter 4 Instrumentation

4.1 Introduction

All the samples were measured in one of two cryogenic systems in the Department of Physics and Astronomy. These two systems are designated as the Black and the Blue systems according to the colour of their outer jacket.

4.2 The Blue System

The blue system is an Oxford Instruments superconducting magnet in a helium cryostat. It contains a Variable Temperature Insert (VTI) (Fig. 4.1) which enables accurate control of the sample temperature. The temperature of the “sample space” in which the sample sits can be reduced below 4.2K by pumping the volume above the liquid to reduce the pressure. This then lowers the boiling point of the liquid and thus the temperature of the sample. A steady input stream of helium through the needle valve has to be maintained to prevent the helium “running dry” and thus to keep the system in equilibrium. A base temperature of approximately 1.4K can be achieved over long periods of time by this method.

The blue system VTI also has the capability to support temperatures above 4.2K. There is a heater on the helium input needle valve which allows the temperature of the sample space to be raised to above 100K. The temperature of both the sample space and the foot of the sample rod (which is assumed to be the same as the sample) can be measured using resistors. These values can then be used to regulate the heater power, creating a stable temperature. Once again a steady stream of helium in to the sample space is required to create an equilibrium temperature, i.e. a balance between the heating power of the heater and the cooling power of the helium. This is achieved by an Oxford Instruments Temperature Controller (ITC 502). A target temperature is programmed in, along with suitable Proportional Band, Integral Action and Derivative Action values, and the system is left to reach equilibrium. [1]

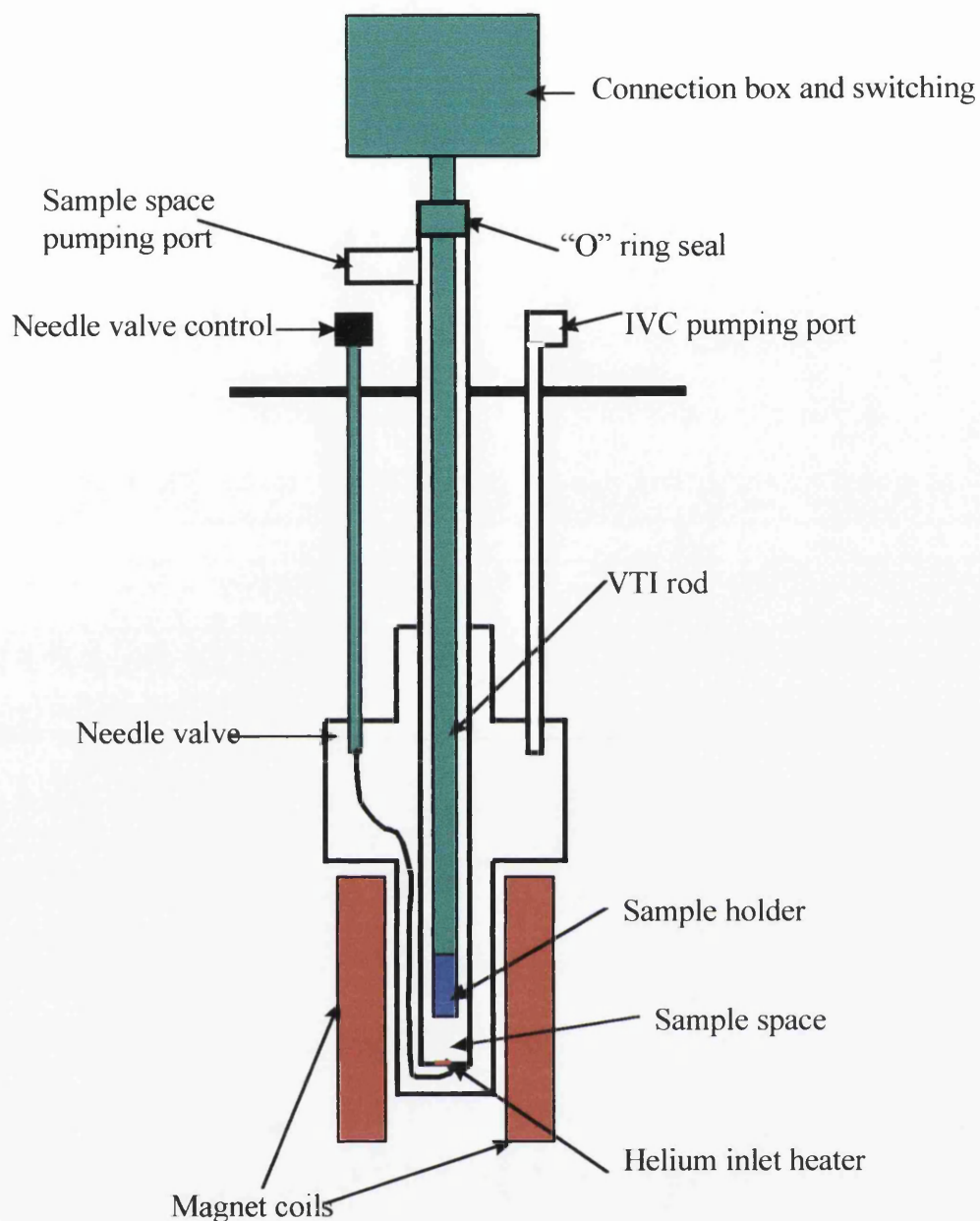


Fig. 4.1 Schematic of VTI insert and sample rod. The width to height ratio has been exaggerated. [2]

The superconducting magnet sits in the base of the cryostat in a bath of liquid helium. It is powered by an independent power supply (Oxford Instruments PS 120) which can output currents up to 100A. The field in the magnet can be swept from 0T to 10T at 4.2K or placed in persistent mode i.e. remain at a set field for an indefinite time. The user also has the option of setting the speed with which the power supply ramps to the chosen field. The faster the sweep the more energy is dissipated into the helium bath and the larger any hysteresis effects. In my experiments, a maximum rate

of 0.3T/min was used when sweeping to high fields. The minimum rate depends on the length of time one is willing to wait for a result.

Should the entire bath be reduced to a temperature of 2K then 12T can be attained. This process uses far more liquid helium than maintaining the bath at 4.2K. This is because the space above the entire liquid helium bath must be reduced in pressure by pumping to create the temperature change.

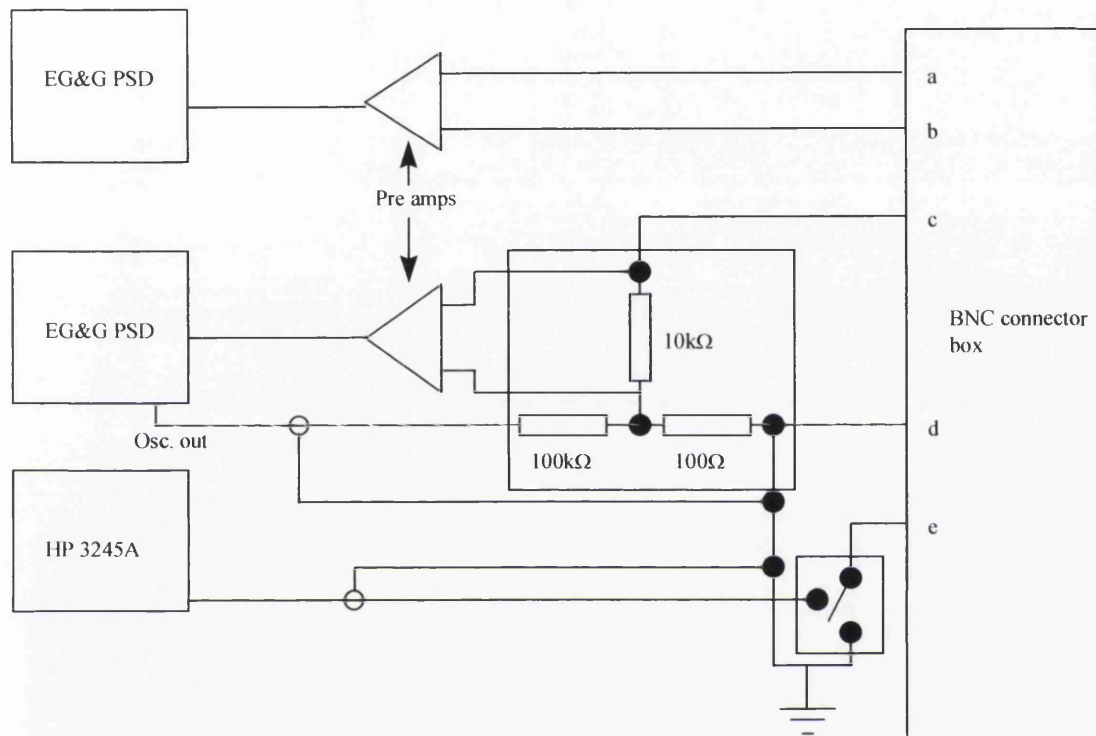


Fig. 4.2 Measurement Wiring. The letters a-e relate to the connections shown in Fig. 4.3.

The sample is mounted in the sample holder on the end of the sample rod and placed in the field of the magnet. The sample package rests on a set of 18 contacts. These contacts are then wired to a switch box at the head of the rod, through a high frequency r.f. filter. This is then connected to an array of BNC cable connectors (one for each of the 18 initial pins) which can then be connected to a set of pre-amps through a simple circuit (Figs. 4.2 and 4.3). These pre-amps increase the signal in relation to any asynchronous noise in the room. The signal is then sent to an EG&G 5210 lock-in amplifier operating at 18Hz. AC techniques are used to measure the samples as this allows us to filter out any 50Hz noise (as 18Hz is not a sub-harmonic of 50Hz) and avoids the 1/F noise to be found at low frequencies, and D.C. It is

important to use a low frequency, however, to allow the measured system to be as close to equilibrium as possible. A further source of noise comes from thermal and electrical excitation. To ensure this is as low as possible it is necessary to keep the electrical energy supplied to the sample below the thermal energy (kT). Thus, for measurements made at 1.6K, $1\mu V$ is usually placed across the sample. The sample resistance is calculated by measuring the voltage across the sample and the voltage across a known resistor in series (but outside the cryostat) with the sample. Thus the current through the sample and series resistor can be calculated and hence the resistance of the sample can be found. The gate voltage is set by an independent HP 3245A Universal Source.

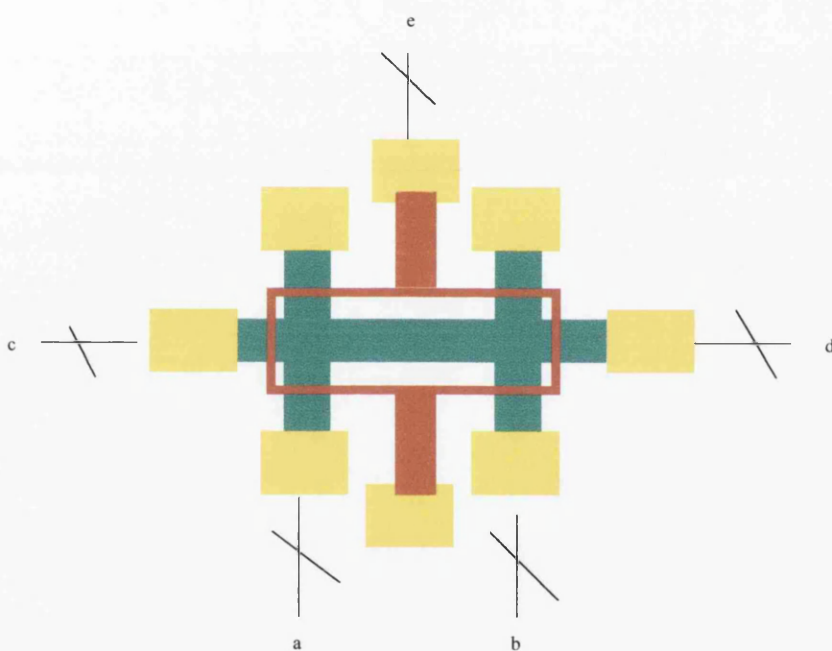


Fig. 4.3 Connections in the sample holder

All the connections from the rod to the outside world are made through a series of r.f. filters and switches at the top of the rod. Thus the sample can be kept isolated from the world, and any dangerous power surges or stray voltages, until it is required. The switch box is then connected to the measurement circuit through an array of BNC connectors. Thus, to change the measurement configuration we can simply change which BNC sockets a-e are plugged into.

4.3 The Black System

The black system is a similar Oxford Instruments cryostat with a slightly larger superconducting magnet which can achieve fields of 15T at 2K. Temperatures above 4.2K were not reached in this system but, with a dilution refrigerator insert (Fig. 4.4), temperatures as low as 30mK can be achieved.

This dilution refrigerator is a $^3\text{He}/^4\text{He}$ fridge. If the two isotopes of helium are mixed in the right concentration then the mixture splits into two phases below the tricritical temperature. These can be thought of as a “liquid” and a “gas” phase. If ^3He is pumped from one phase to the other a cooling effect can be produced in a similar way to evaporation at a liquid surface. This ^3He must then be returned to the initial phase, setting up a dynamic equilibrium. Hence, the ^3He is pumped from the still and returned via the condenser line. Here it returns to a liquid state, as it flows through a capillary which allows sufficient pressure to build up that condensation occurs, and flows back into the mixing chamber. The ^3He then moves from the “liquid” to the “gas” phase to maintain the equilibrium and the temperature remains low. The phase boundary only exists below the Tricritical point of a $^3\text{He}/^4\text{He}$ mixture which is at 0.86K. A small heater is available on the mixing chamber which allows the temperature to be varied in a controlled manner up to approximately 800mK. The sample is thermally connected to the Mixing chamber and it’s electrical connections are thermally anchored on the way down from room temperature to ensure a stable low temperature. [3]

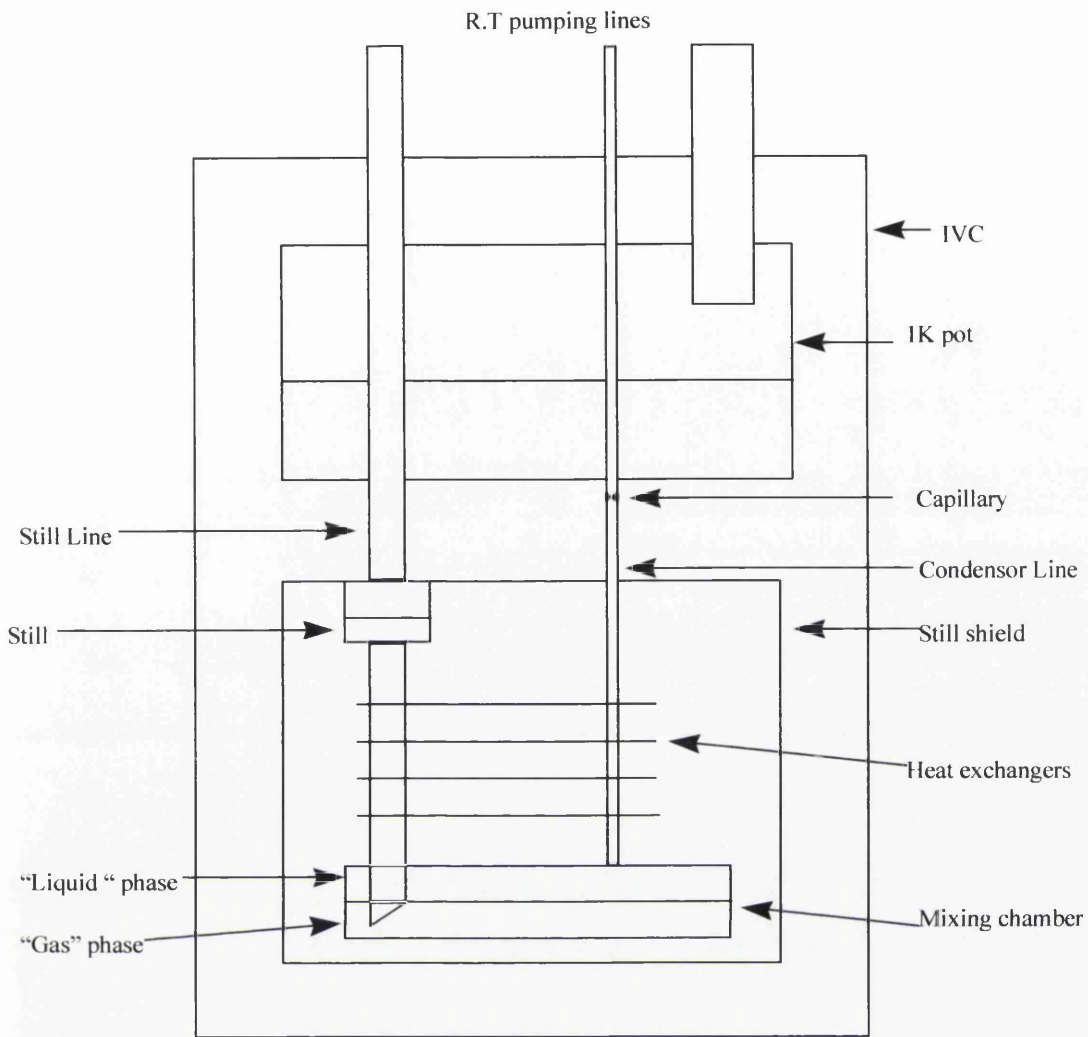


Fig. 4.4 Schematic of the dilution refrigerator [3]

These low temperatures can almost fully remove any noise in the sample due to thermal effects. Thus electronic noise becomes dominant. Obviously a very low excitation voltage (below the kT of the sample) will help to reduce this but a large amount of noise can be generated in the wires and cables used for the measurements. Thus a lot of work has been done to filter this out by K. Lister [4] (Fig. 4.5).

The current forming resistor and any voltage dividers are attached to the sample rod foot, and hence are operated at the same temperature as the fridge. This reduces the Johnson noise in the resistors, as well as reducing the length of wire over which the small voltage signals have to travel. Also, a number of low pass filters are placed in the circuit, which are battery powered to remove mains hum. These reduce the rf pickup, as well as any high frequency harmonics of the mains that may be present. Twisted pair cabling is used in the circuit, as this reduces the coupling from

magnetic fields. Also, a differential signal can be employed, which removes the problem of a fluctuating ground. Finally the entire system is operated within a Faraday cage with all but the filtered lines disconnected from the outside world. These are then connected to similar lock-in amplifiers and Universal Sources as are used on the Blue system.

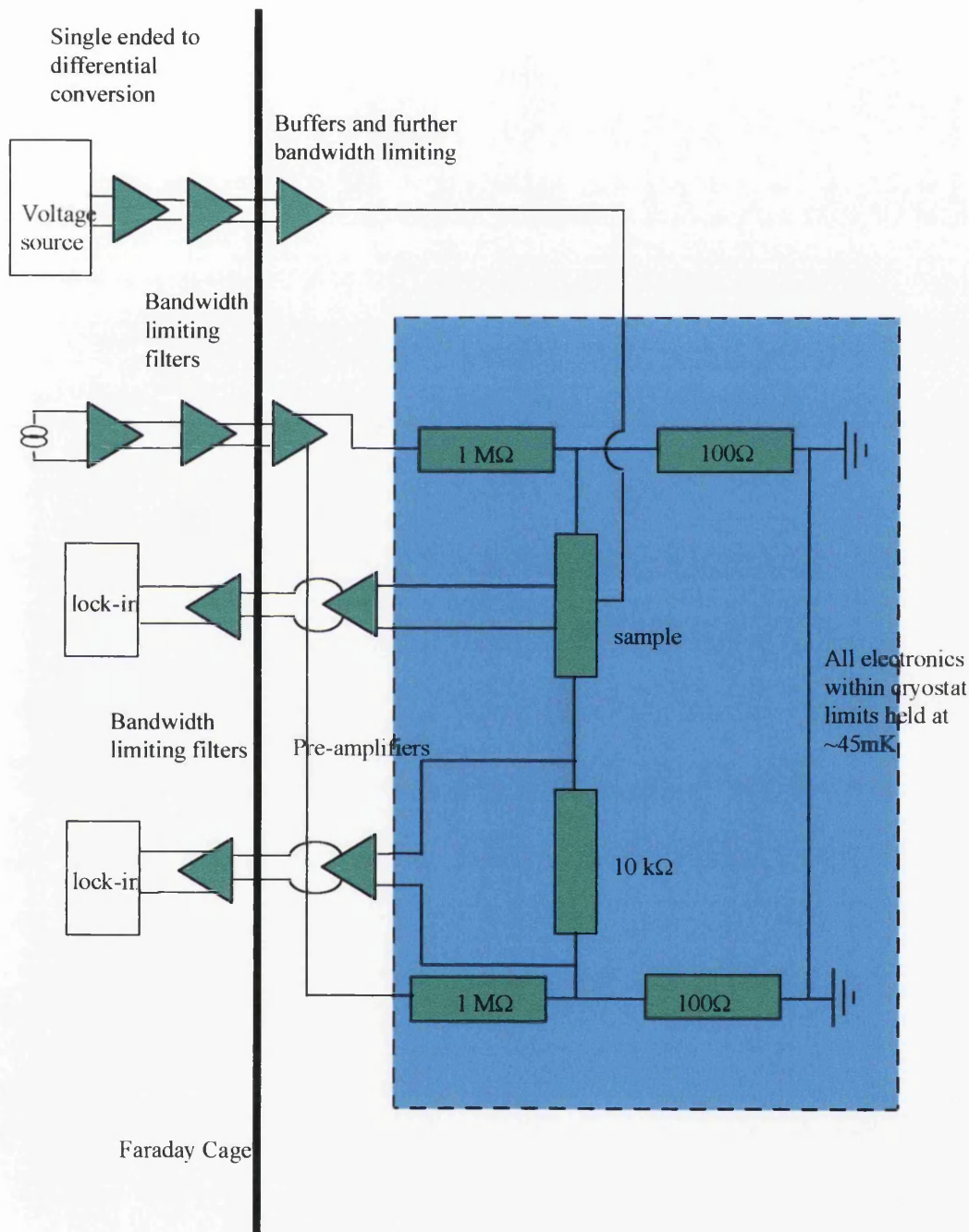


Fig. 4.5 Schematic of fridge electronics

4.4 Data Acquisition

All these measurement and biasing instruments have IEEE interfaces. Thus it is relatively easy to connect them to a computer. Using the Labview™ software writing package from National Instruments I have written a suite of programs to run the experiments and accumulate the data. It has a very good error checking and debugging facility. It also is well supported in terms of instrument drivers, both written by National Instruments and by the manufacturers of individual instruments. Using supplied drivers or ones I have written we can run a set of experiments where we vary gate voltages or magnetic field. Thus the computer will set up the required parameters of sweep rate, gate voltage etc. It will then begin the run and collect all the relevant data from the lock-in amplifiers. This is plotted on screen in real time for information and is saved to a spreadsheet-style file at the end of the run. This data can easily be viewed in spreadsheet programs such as Excel or graphing programs such as Easyplot. The main improvement over the Pascal programs used when I arrived is that measurement parameters are retained between runs, and can be easily changed on an individual basis.

It is also possible to run multiple sweeps (each being saved to its own file) such as sweeping through a magnetic field range and then incrementing the gate voltage before sweeping the field again. This allows a large amount of data to be obtained overnight or at weekends without continuous attention. I have also written programs to acquire time dependant data, capacitance data, calculate Fast Fourier Transforms and investigate gate leakage currents.

It is possible to produce these programs as stand alone executable files. However, as each member of the group has different requirements, some of which change depending on the results obtained, it was found to be simpler to maintain the software at the more memory intensive development level, so as to facilitate rapid changes if, and when, they are required

A detailed description of the measurement suite is given in the Appendix.

References

[1] Temperature Controller ITC 502 Operator's Handbook, Oxford Instruments (1993)

[2] Stuart Vallis, 'PhD Thesis, University of Glasgow (1996)

[3] Kelvinox Dilution Refrigerator Manual, Oxford Instruments (1990)

[4] Kevin Lister, PhD Thesis, University of Glasgow (2000)

Chapter 5 300nm period LSSL results.

5.1 Introduction

All the samples were produced on similar Hall bars. As Fig. 5.1 shows, there is a background set of oscillations present before any periodic potential is added. These are the Shubnikov de-Haas oscillations associated with the Landau Levels. These are present in all the traces obtained in these experiments with the period defined by the number of carriers, and the width and height by bulk scattering and the temperature.

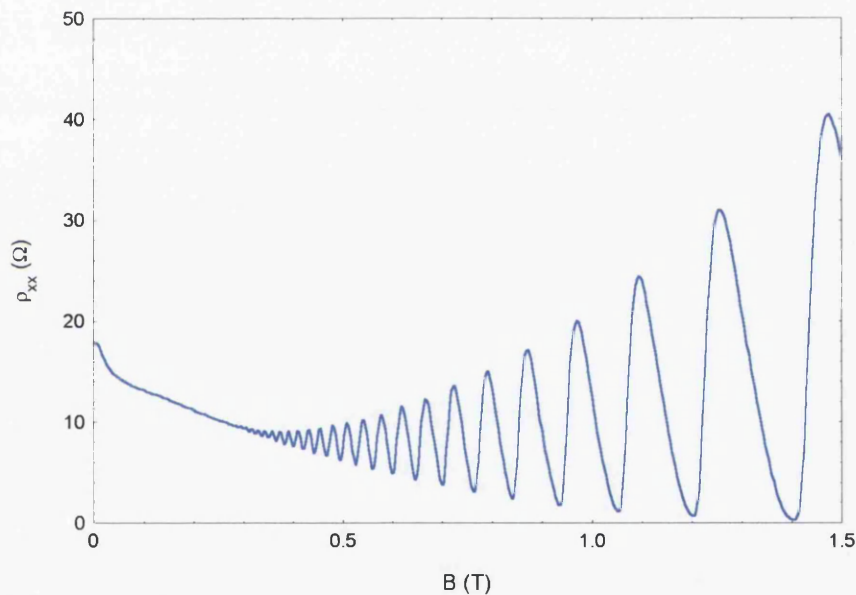


Fig 5.1 Unpatterned Hall bar fabricated on control material and measured at 1.6K

The first etched superlattices produced had a period of 300nm. Initially they were made without a gate as the fabrication process was not finalised. A mark:space ratio of 1:10 was used for the first set of samples with 1:1 being used for the rest. For the purposes of this thesis, “mark” is the mark written by the beam writer. Thus the mark becomes the trench after etching, while the space is the rib left behind.

A preliminary account of this work has been published [1].

5.2 Samples with a mark:space of 1:10.

These are samples 2 to 7 in Table 3.2. These were the first etched superlattices to be fabricated and so were produced in a number of different ways. The 60s dry etch time (sample 4) gave a very small yet measurable commensurability oscillation. This encouraged us that we were on the right lines and so we subsequently looked at 90s dry etch and 12s and 17s wet etched samples. Wet etched samples were produced using the recipe normally used in the isolation process. This was done as we were not yet in a position to say that the dry etching was going to work, and we wished to produce some samples quickly to observe the effects. This was not an ideal etch, due to its speed and so was discarded when the dry etch process was shown to be effective. The 17s sample (sample 3) was over etched. This etch depleted most of the electrons in the channel. The trace obtained (Fig. 5.2) had a very large initial resistance which then dropped with magnetic field. It continued to drop until the SdH oscillations were large enough to be seen. This occurred at fields well above that for observing COs. This does however follow the theory [2]. This theory states that a Negative MagnetoResistance (NMR) arises in the presence of a large potential modulation. For very strong modulations, this NMR can drown out the expected PMR and COs. Thus Fig. 5.2 indicates that a strong periodic potential could exist in this sample. We later discovered that the combination of surface and piezoelectric components was a minimum in the crystal direction measured (See section 2.3). Our conclusion was that a 17s wet etch is the maximum etch measurable and all further samples were aimed to be etched less deeply.

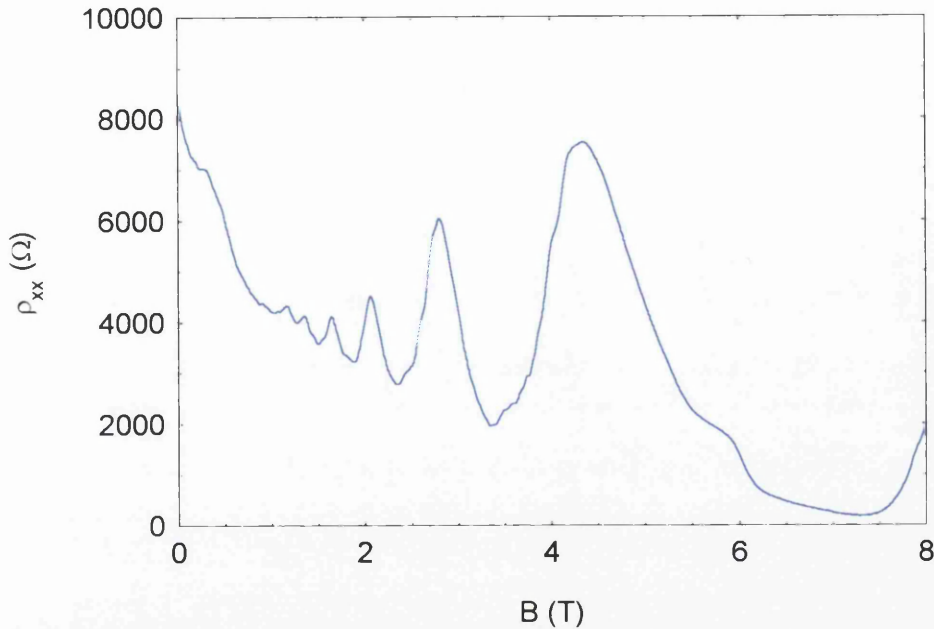


Fig. 5.2 The magnetoresistance of the 17s wet etch sample 1.6K $[01\bar{1}]$

The 90s dry (sample 6) and the 12s wet (sample 2) etched samples gave very interesting results. The carrier concentrations were similar to that of the unetched samples (sample 1) but the mobility dropped to about a third of its original value. As can be seen in the graphs of resistance (Fig. 5.3 and 5.4) against magnetic field all types of structure that are to be expected were found. This includes the low field PMR peak at approximately 0.1T in Fig.5.3, the COs, visible as large oscillations up to 1T, and the SdH oscillations, which are just visible, beginning at approximately 0.9T in Fig. 5.3. For these samples longitudinal resistance was normally measured over a magnetic field of 0T to 3T. This covered all the COs and allowed a large amount of data about the high field PMR to be obtained. These early samples did not have a gate, as we were unsure what results the etching would produce. The difference in etch methods has led to a difference in etched depths. Thus the resultant stressor induced potentials are not the same in each of the samples. The dry etched sample have larger oscillations. This would indicate that there is a larger potential modulation present, and hence that that sample has a greater etch depth.

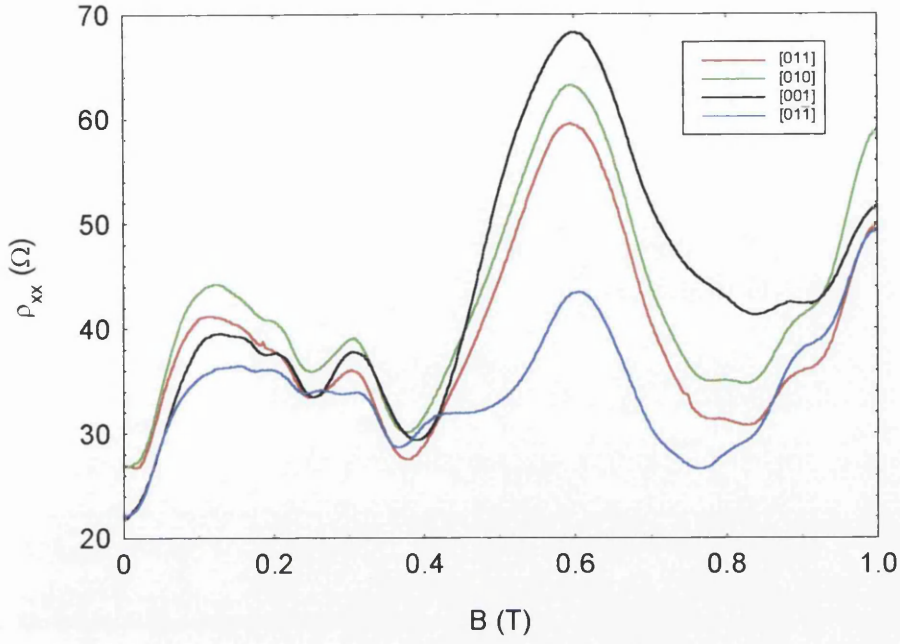


Fig. 5.3 Magnetoresistance of Sample 2 (12s wet) measured at 5K

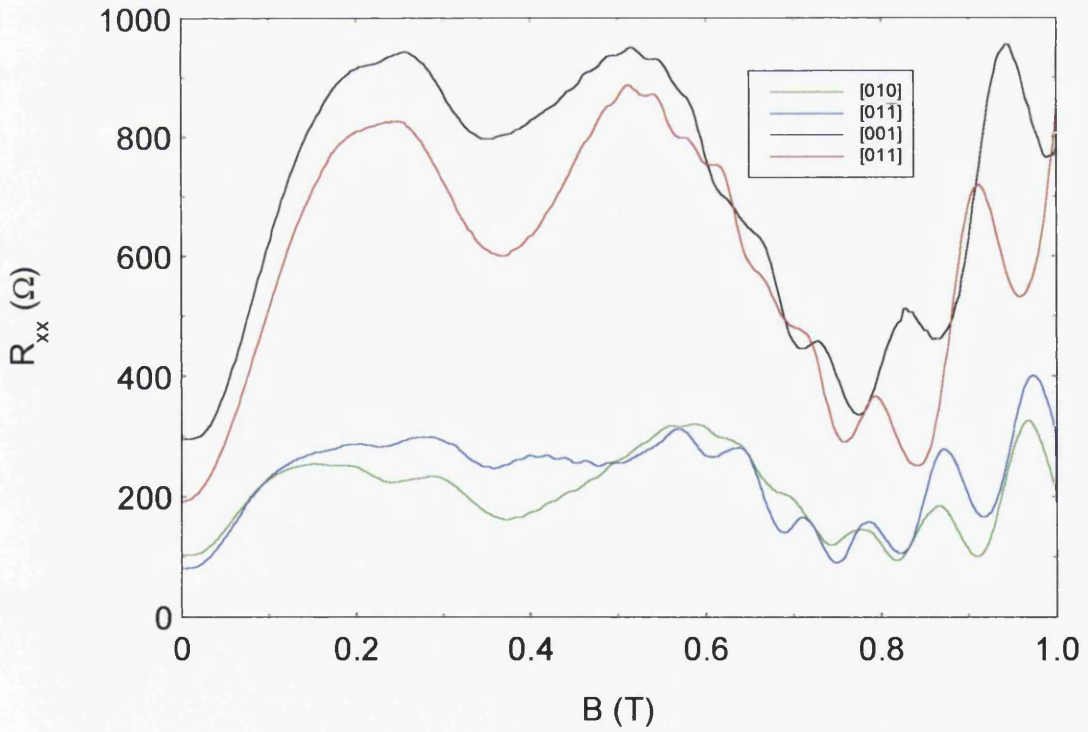


Fig. 5.4 Magneto resistance of Sample 6 (90s dry) measured at 5K. The difference in zero field resistance is due to differing carrier densities.

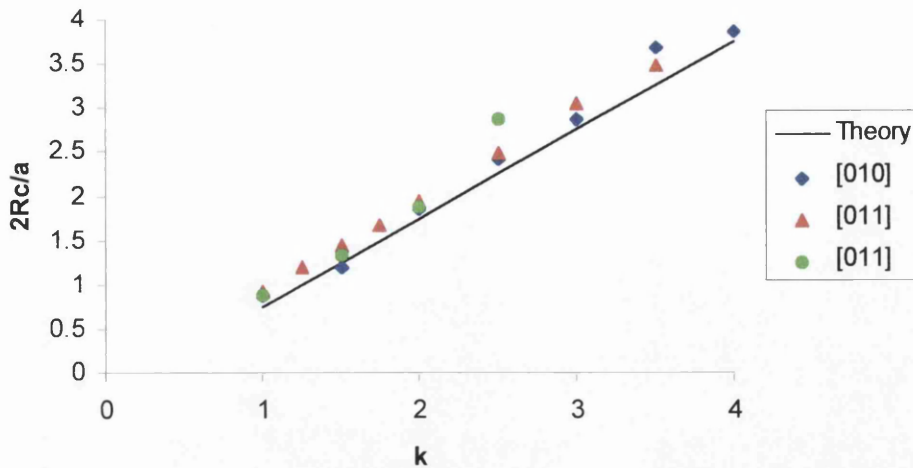


Fig. 5.5 Peak or trough position in sample 6 expressed as twice the equivalent cyclotron radius R_c divided by the period a . A theoretical line is also plotted.

As can be seen, there is a directional component which we attribute to the piezoelectric effect. The $[011]$ and $[0\bar{1}\bar{1}]$ directions are those in which a piezoelectric component is expected to be significant. In both Figs. 5.3 and 5.4 $[011]$ has larger oscillations, indicating a stronger potential, while $[0\bar{1}\bar{1}]$ has more, smaller oscillations. This fits with the idea of the piezoelectric potential amplitude changing with angle. In the $[001]$ and $[010]$ directions the piezoelectric effect is expected to be zero. Thus, the oscillations present are assumed to be due to the surface effect described earlier. We deduce further that, in $[011]$ the surface and piezoelectric potentials have the same sign. Thus they combine to give a large amplitude. In $[0\bar{1}\bar{1}]$ the piezoelectric component has the opposite sign to the surface effect. Thus the resultant amplitude is reduced.

The only minima visible in $[010]$ and $[001]$ can be explained by the basic Beenaker equation, as is illustrated in Fig. 5.5. This figure plots the peak (or trough) position as expressed in terms of the cyclotron radius of a commensurability oscillation, as a function of the cyclotron radius R_c and the period a , against k , the CO index. A theoretical set of points is also plotted, to indicate where the experimental points should fall. These theoretical points are plotted for a fundamental only, thus, any points lying in between these points can be assumed to be due to a second harmonic. Thus we can conclude that there is no second harmonic in the $[010]$ and $[001]$

directions as they follow the theory plot exactly. Therefore the surface effect does not have any significant harmonics. This indicates that the additional oscillations seen in $[01\bar{1}]$, and illustrated in Fig. 5.5 must come from the piezoelectric component. A relatively strong harmonic is expected from the piezoelectric theory [3]. The lack of detectable second harmonic oscillations in $[011]$ is due to the fundamental oscillations being large and dominating this weaker second harmonic. This addition and cancellation effect can be seen both in samples 2 and 6. The slight differences to be seen between $[010]$ and $[001]$ in Fig. 5.4 can be attributed to slightly different carrier concentrations. This occurs as the two devices were measured in different cooling cycles.

Fast Fourier Transforms (FFTs) can be calculated of the results shown. These highlight any periodic effects in the traces. These were carried out using a software tool written by Dr. Skuras and produced the results shown in Figs. 5.6 and 5.7. As can be seen in these graphs, multiple peaks are obtained. The high frequency peak is due to the periodic SdH oscillations. The position of this peak, here at approximately 8T, can be used to calculate the carrier concentration as follows;

$$\Delta\left(\frac{1}{B}\right) = \frac{hn_{2D}}{2e} \quad (5.1)$$

The lower frequency peaks can be attributed to the COs. Also, the additional peak, caused by the second harmonic in $[01\bar{1}]$ can be seen. This proves that we are indeed observing a second harmonic.

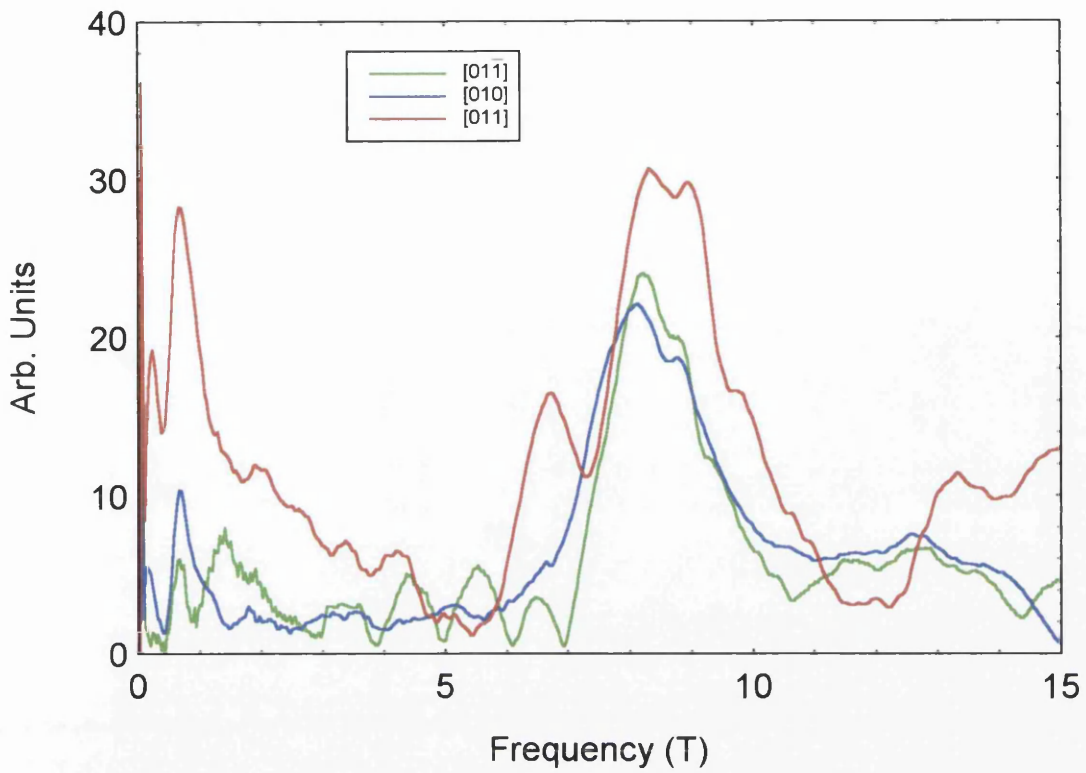


Fig. 5.6 Fast Fourier Transform of the traces plotted in Fig. 5.4

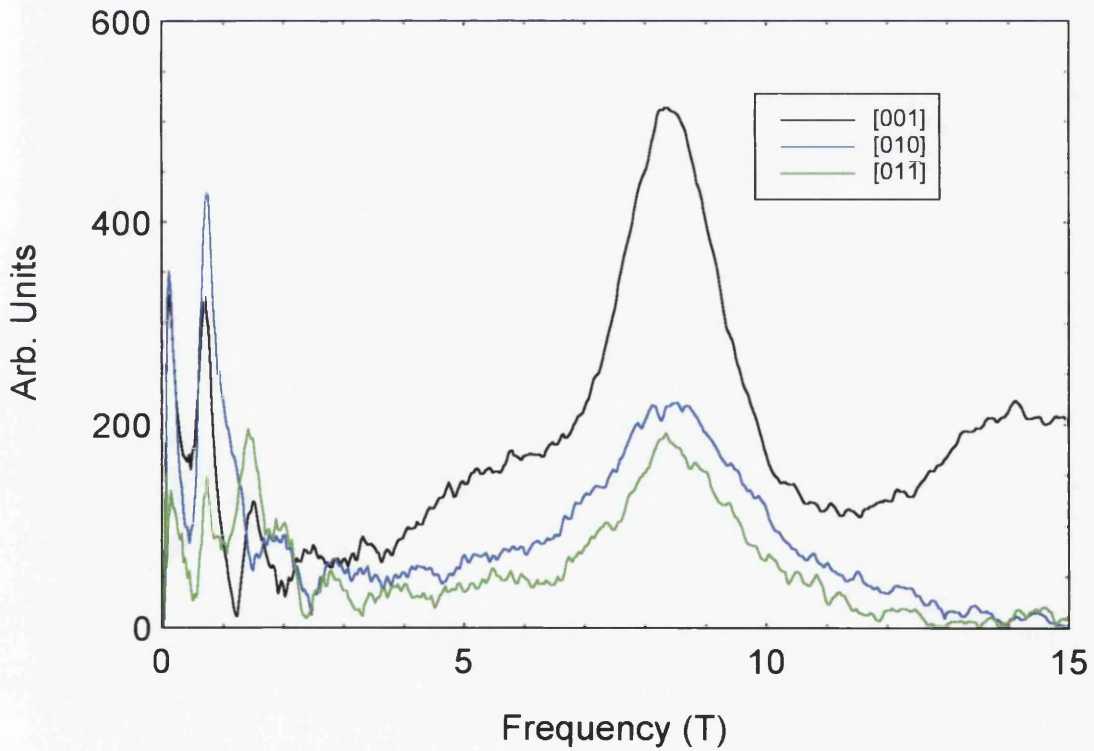


Fig. 5.7 Fast Fourier Transform of Fig. 5.3

5.3 Samples with mark:space ratio 1:1, Basic Features

These samples were produced solely by dry etching but were gated. The pattern written was such that it left a 1:1 mark:space pattern in the resist mask. An AFM picture of an ungated sample (Fig. 5.8) fabricated at the same time showed that the final mark:space ratio was 1:1.5 where the etched trench was the mark written in the beam writer.

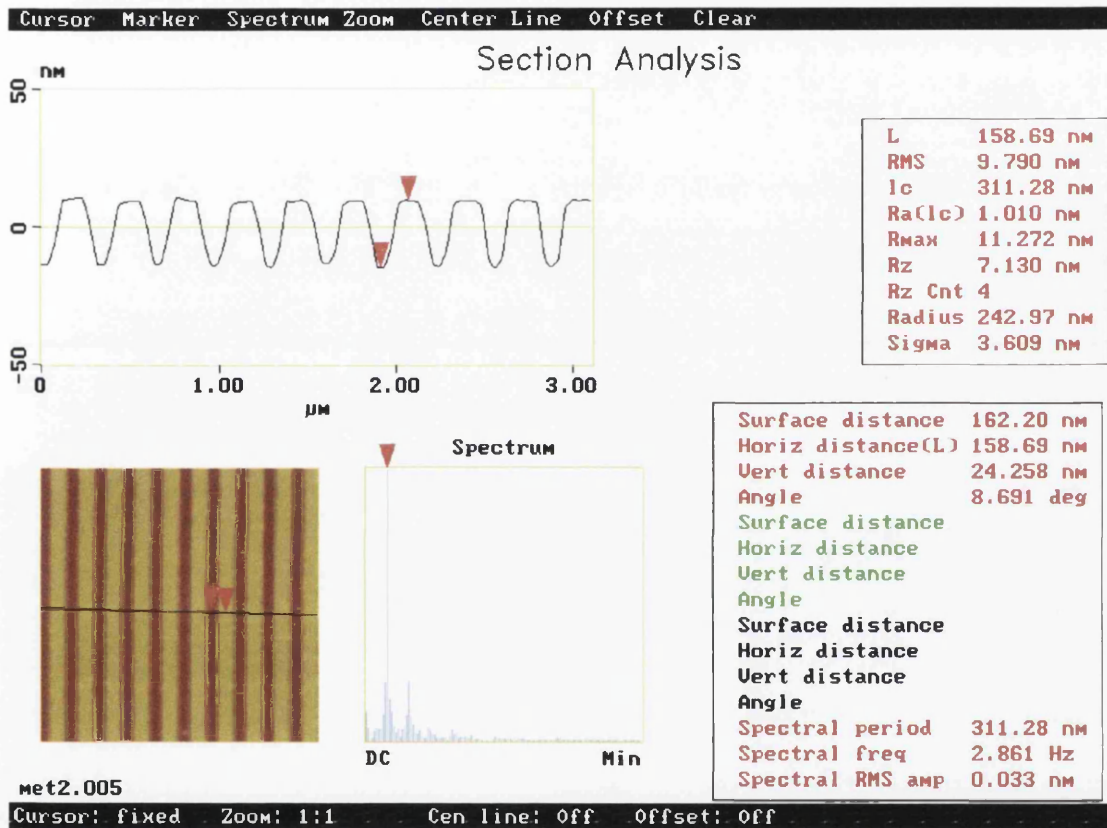


Fig. 5.8 AFM image of an LSSL manufactured using the same conditions as Sample 9, but left ungated. The analysis shown gives a depth of 23 ± 1 nm. The AFM measurement tip has a diameter of 20 nm and a length of 100 nm.

As the results show (Fig. 5.9), the main features as described in the previous section are still visible. $[010]$ and $[001]$ have similar traces and they show no sign of a second harmonic. In $[011]$ the separate potential components have combined together to produce a large potential, visible as large COs. In $[0\bar{1}\bar{1}]$ there are extra oscillations, which we attribute to the second harmonic. There appears to have been a slight change in the magnitude of the separate component however. The surface and piezoelectric

now cancel completely. This, we believe, is due to the change in mark:space ratio affecting the magnitude of the potential components such that they have similar fundamental magnitudes.

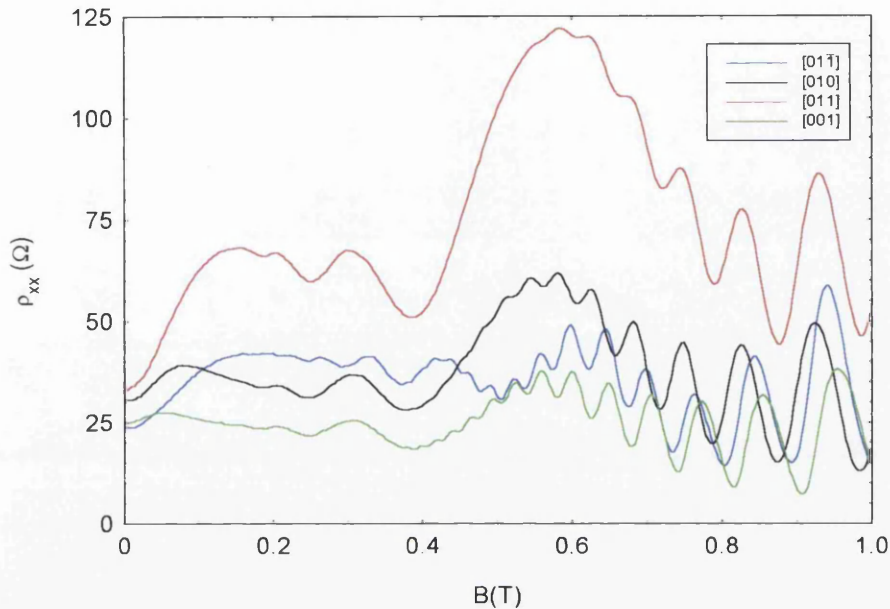


Fig. 5.9 Magnetoresistance of Sample 9 measured at 1.6K. $V_g=0V$

It turned out that, in this sample, the fundamental components of the surface and piezoelectric potentials were almost identical. Thus, when they have the same sign, [011], a large potential was observed but when they were in opposition, $[0\bar{1}\bar{1}]$, they cancelled almost perfectly. As can be seen in Fig. 5.9, when they cancel, oscillations at twice the expected frequency are seen (Fig 5.10). This is a second harmonic which is attributed to the piezoelectric part, as it is not to be seen in [001] or [010], where the piezoelectric component is expected to be zero. It is expected from theory that the piezoelectric coupling will generate a large number of harmonics while the surface potential is believed to be closer to single frequency. [4]

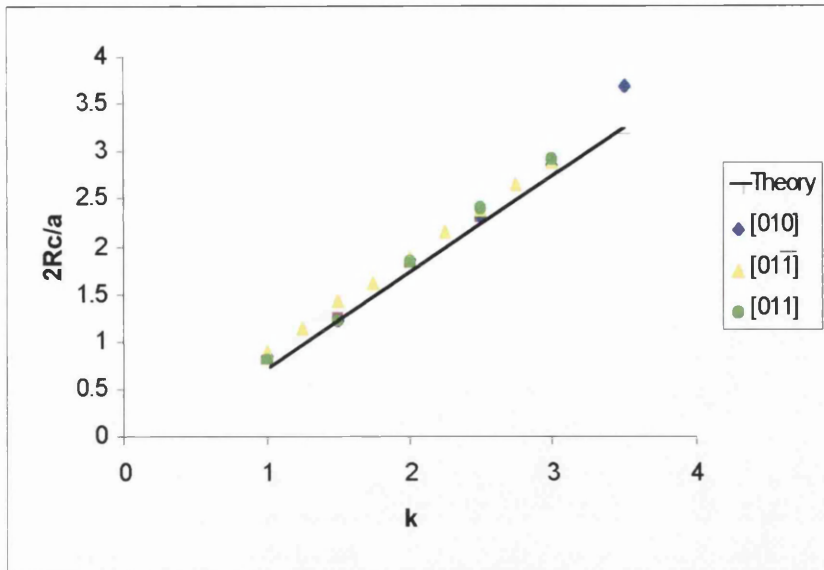


Fig. 5.10 Peak or trough position for the sample shown in Fig. 5.9 expressed as twice the equivalent cyclotron radius R_c divided by the period a . A theoretical line is also plotted.

A comparison of the traces obtained for samples 9 and 6 shows a number of things. Having changed the ratio of rib to space appears to have changed the relative magnitudes of the fundamental to second harmonic in the piezoelectric potential. The fundamental has now become smaller, allowing it to be cancelled by the surface component, while the harmonic remains large. This confirms the theory as described earlier and also suggests that specific harmonics can be encouraged by careful fabrication. It also warns how critical it is to control the mark:space ratio to produce samples with the characteristics predicted.

The samples were measured in detail at 5K rather than at the base temperature of 1.6K. This reduced the magnitude of the SdH oscillations while the CO were relatively unaffected and allowed good measurements of peak heights and positions from which values for the potential modulation could be calculated. A detailed discussion of the temperature dependence is given later.

Fast Fourier Transforms of the 1:1 samples were also calculated. As Fig. 5.11 illustrates, [010] and [001] have similar frequency spectrums while [011] has a larger low frequency peak, indicating the stronger periodic modulation. The second harmonic can be clearly seen in $[01\bar{1}]$, where it has a higher peak height than the peak due to the fundamental.

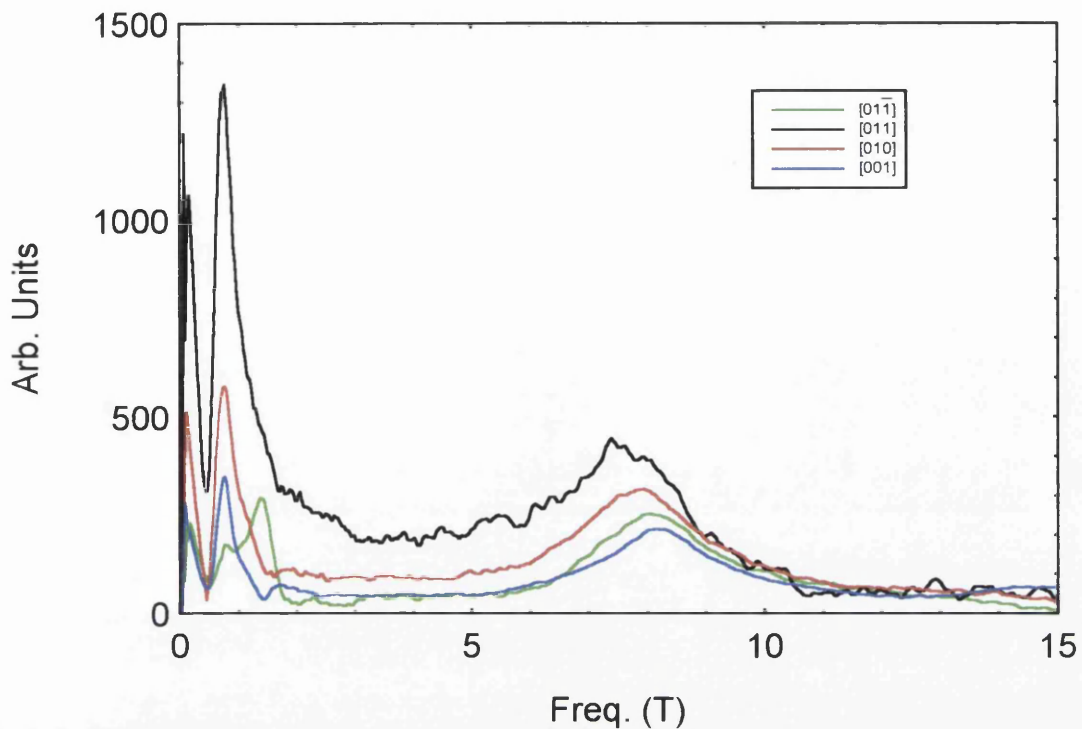


Fig. 5.11 FFT of results shown in Fig. 5.9

If the results for the control samples (samples missing the InGaAs stressor layer) are studied (Fig. 5.12), then it can be seen that they mirror closely the results obtained from the [010] and [001] stressed samples. This is true in both the directions associated with piezoelectric effects in the stressor sample, and the cube axis directions. [011] data is plotted as an example of the former and [001] as an example of the latter.

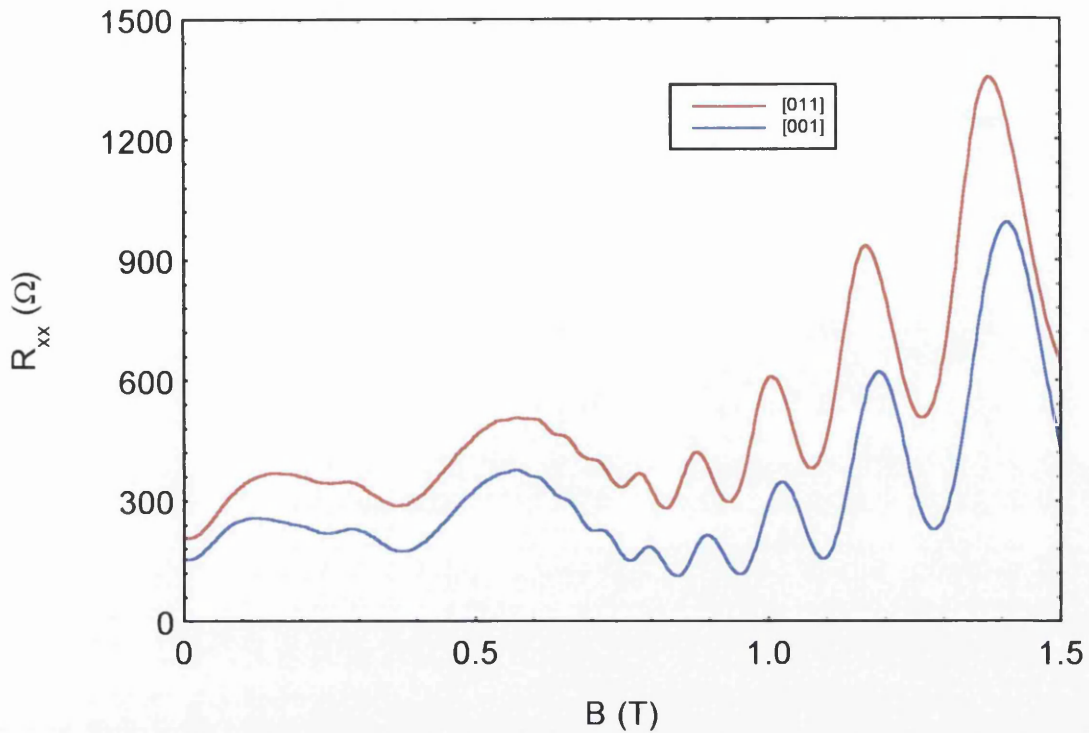


Figure 5.12 Magnetoresistance traces obtained from the control samples, made at the same time, and under the same conditions as the stressor sample 9. $T=1.6\text{K}$.
 $V_g=0\text{V}$

5.4 Samples with 1:1 mark:space, Gate effects

When a voltage is applied to the surface gate overlaying these samples the complex behaviour of Figs. 5.13 and 5.14 is observed.

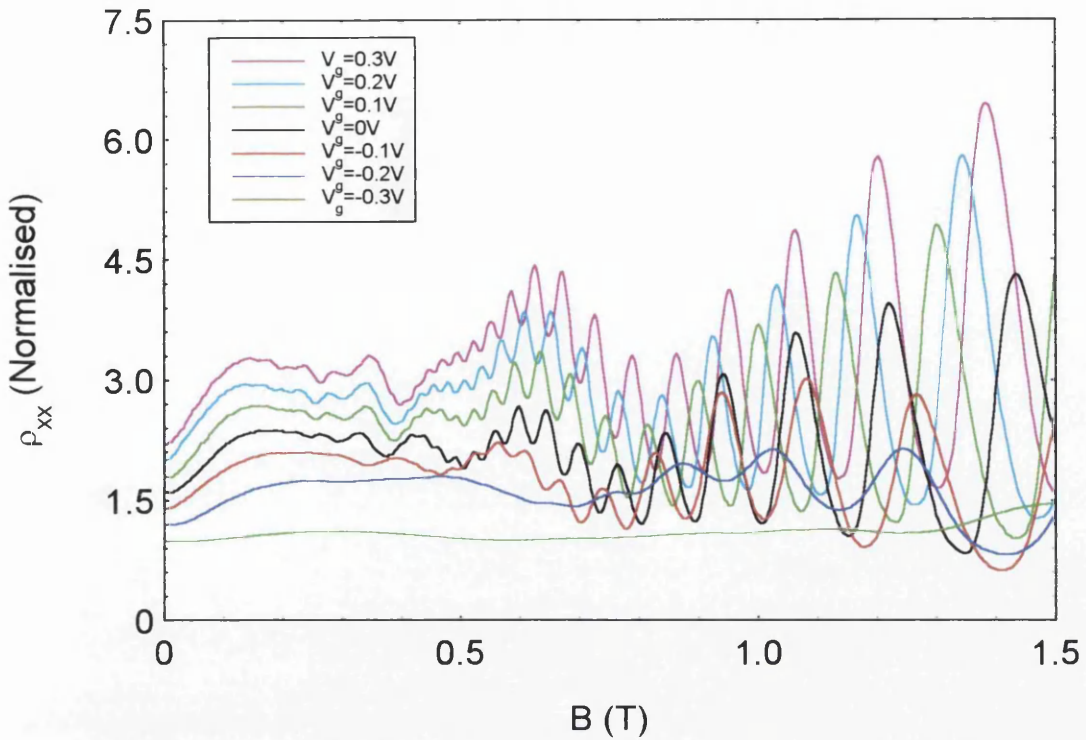


Fig. 5.13 Voltage effects on the magnetoresistance of the $[01\bar{1}]$ orientation of sample 9 at 5K. Traces have been normalised to a zero field resistance of 1 and then displaced by 0.2 for clarity.

As is expected biasing the gate changes the carrier concentration and also the ratio; $\frac{eV_0}{E_F}$. The heights of the CO peaks observed are proportional to the square of this ratio. Therefore, if this ratio is changed by biasing the gate, the size of the oscillations observed will also change. The magnitude also varies with the square of the mean free path in Beenakers equation (Eqn. 2.8). As $l = (2\pi m_{2D})^{-\frac{1}{2}} \frac{\eta\mu}{e}$ and E_F varies proportionally with the same carrier concentration then the change of resistance becomes proportional to $\frac{1}{n_{2D}}$

When potentials are calculated (see following section) it can be seen that the total potential changes with voltage. This indicates that the gate itself has a periodic effect which further adds to the potentials present, and hence confirms that, after fabrication, the gate metal fills the troughs caused by etching. Thus the gate is closer to the 2DEG in the etched regions than on top of the ribs, supplying further modulation.

No second harmonic is observed in [010] or [001] when the voltage is varied (Fig. 5.14). This shows that the gate has no second harmonic content. Therefore, it is possible, in a device with strong second harmonic to tune the sum total of the fundamentals such that they are minimised and a device with effectively half the initial period can be produced. This maybe useful as we approach the current size limit of lithography which is a lattice of period 50~60nm.

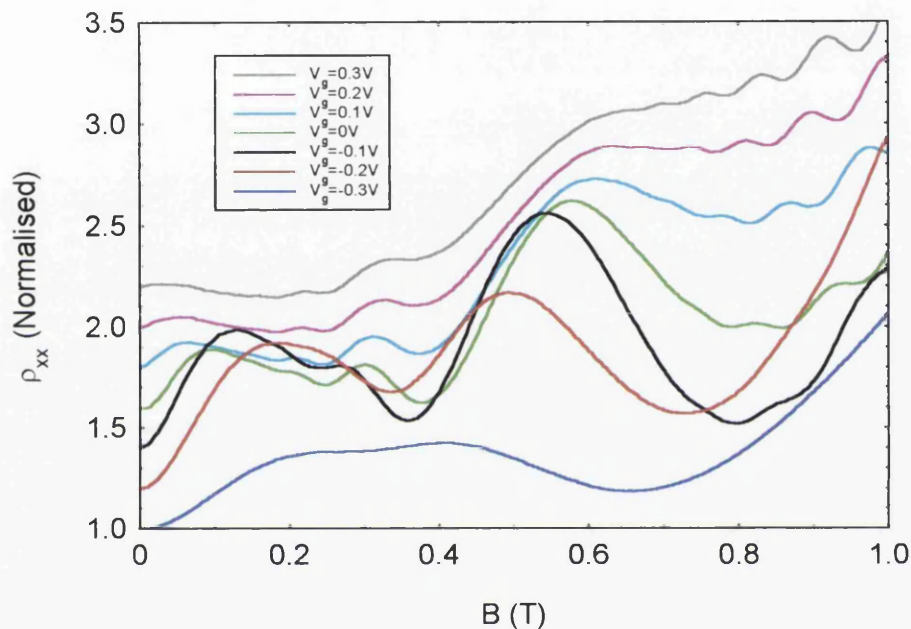


Fig. 5.14 Magnetoresistance variation with gate bias for [001] crystal direction. Traces have been normalised to a zero field resistance of 1 and then displaced by 0.2 for clarity.

5.5 Potential Magnitudes of 1:1 mark:space samples

Dr. J.H. Davies has produced a spreadsheet that calculates the theoretical potential modulation amplitudes produced by an etched rib, based on Larkin, Davies, Long and Cusko [4]. By assuming an elastic gate on a rigid surface the spreadsheet calculates the forces due to the lattice mismatch. It then calculates the electrostatic potential from the piezoelectric polarisation, both when a parasitic layer of electrons exists about the donors, and without this parasitic layer. For the 300nm samples the spreadsheet produced the values in Table 5.1.

	Fundamental (meV)	Second Harmonic (meV)
Parasitic layer	-0.615	-0.517
No parasitic layer	-1.472	-0.07

Table 5.1 Theoretical values of potential modulation in 300nm period $[01\bar{1}]$ sample.

The magnitude of the potential was calculated from the data by the two methods described in Chapter 2. These were (I) measuring the peak to peak change on resistance in a commensurability minimum and applying the Beenaker formula [3] and (II) measuring the relative positions of the PMR peak and a minimum and applying the formula as given by Beton et al [5]. Measurement errors can arise from both these methods as we are ignoring any interactions between the two oscillations that may affect the amplitudes. Hence we calculate potential magnitudes using data measured at 5K, where the SdH oscillations have been reduced. Also, if the potential magnitude is large, the PMR peak can overlap the COs, leading to an error in the measured positions. There is also a measurement error associated with judging the background slopes effect on any given measurement.

Fig. 5.15 a-d shows the periodic potential of sample 9 for the four crystal directions fabricated as a function of gate voltage. As previously explained there are two different ways of calculating the potential and the results from these two methods have been displayed together for comparison

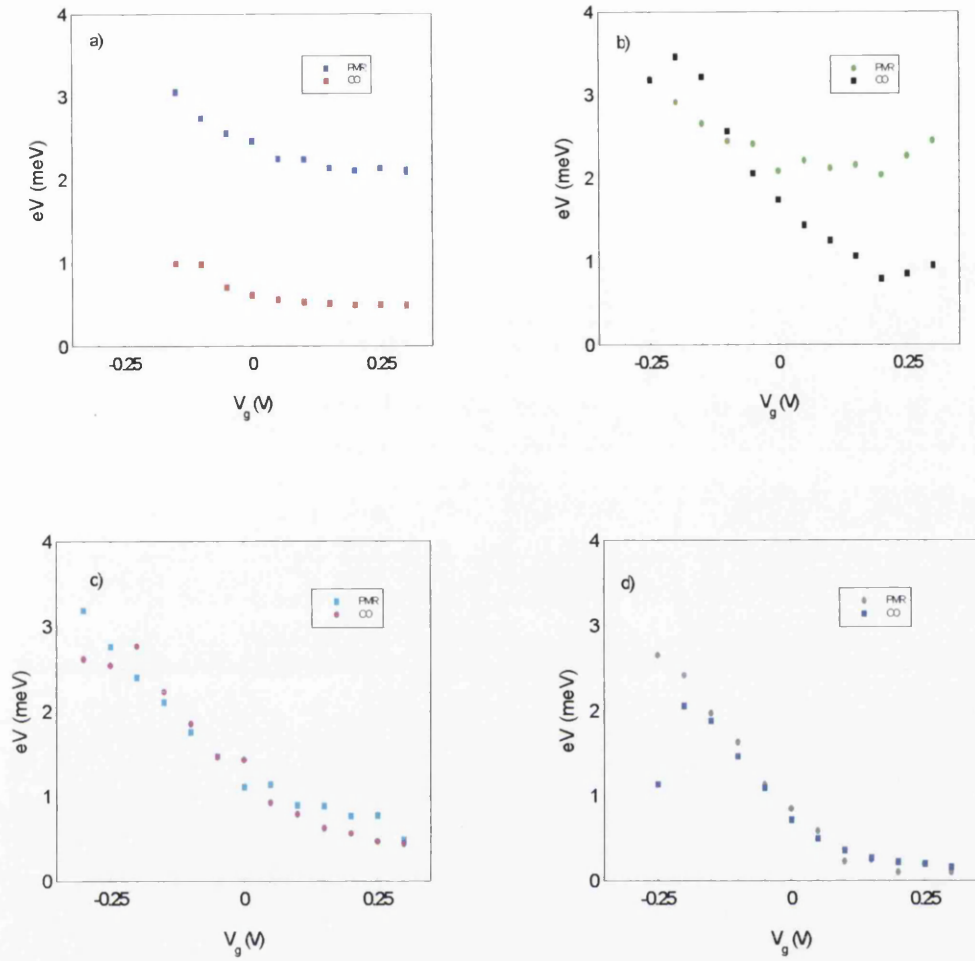


Fig. 5.15 Amplitude of the periodic potentials in sample 9. a) $[0\bar{1}1]$, b) $[01\bar{1}]$, c) $[010]$, d) $[001]$

Figs. 5.15c and d show the results for the directions where the piezoelectric component is zero. The two methods are seen to give the same result. This indicates that there is no second harmonic present in these two samples. The divergence at high negative gate voltage can be attributed to the fact that both the CO and SdH oscillations are small, increasing any measurement errors in the methods. Reduced screening of the potential from the channel, by electrons in the donor layer, at negative gate voltage also occurs. This contributes to a rapid increase in the magnitude observed, as well as the changing mean free path. The periodic effect of the gate voltage is evident in the variation of potential with voltage, as in $[001]$ the potential almost vanishes at $+0.3V$.

Fig. 5.15a shows $[0\bar{1}1]$, the direction in which the second harmonic is visible. As can be seen, the PMR method gives a much greater magnitude than the CO method. This is the fact that the PMR method gives a value for the potential which includes the harmonic components as well as the fundamental (See Chapter 2). In Fig. 5.15a it can be seen that the fundamental (CO) remains small due to the surface and piezoelectric components being in opposition. It still varies with gate voltage but only by a small amount. The combination of harmonics and fundamental (PMR) gives a much larger effective potential amplitude. This varies similarly with gate voltage as would be expected, the fundamental being a varying component of the total.

Fig. 5.15b shows the potential for $[011]$. Here the different sources of fundamental modulation have the same sign and so a large amplitude is calculated from the CO method. This varies quite considerably with gate voltage as the effective surface potential is a sum of the gate potential and the initial surface potential. There is harmonic content to the potential which can be seen at high positive gate bias. Here, the gate reduces the effective surface potential and hence the total fundamental amplitude is reduced. This allows the harmonic to become a significant part of the total potential. In high negative bias the gate increases the effective surface potential. Thus a large fundamental potential is observed and the harmonics become less significant. Therefore, at high negative voltage only the fundamental is visible, i.e. both methods give similar values.

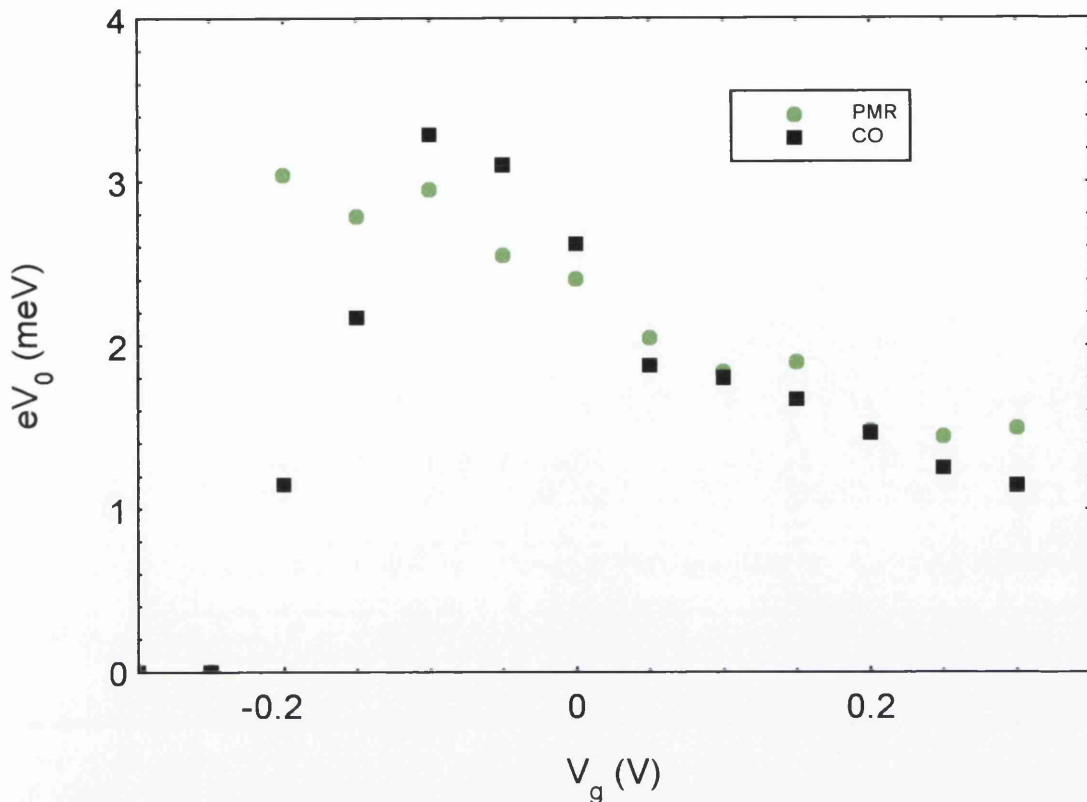


Fig. 5.16 Potential magnitude calculated from sample trace shown in Fig. 5.11 Crystal direction $[0\bar{1}\bar{1}]$

Fig. 5.16 shows the results calculated from a control sample. The result obtained is very similar to that seen for a stressor sample, with a current flow direction of $[010]$ or $[001]$. Once again, the two methods give similar results, indicating a lack of second harmonic. The behaviour at large negative bias is due to the small mean free path causing a smearing of the COs, as well as a reduction of the screening increasing the potential at the 2DEG.

An item of interest to theorists is the sign of the potential. From these experiments it can be seen that, in $[010]$ and $[001]$ a positive gate voltage reduces the magnitude of the potential energy. Thus attracting electrons to a trough reduces the potential energy. The surface potential energy under a trough is positive from basic electrostatic arguments [6]. In the $[0\bar{1}\bar{1}]$ direction the piezoelectric effect cancels the surface effect. Therefore the piezoelectric effect must have a negative potential energy. In the $[01\bar{1}]$ direction the surface and piezoelectric effects add, thus the piezoelectric

effect has a positive potential energy. This agrees with the calculations of Larkin et al [4]

5.6 Temperature dependence of 1:1 mark:space ratio samples

These experiments were carried out at a number of temperatures from 1.6K up to 75K (Fig. 5.17). The SdH oscillations die off reasonably quickly at low temperatures. This leaves the CO which are less temperature dependant. The CO begin to reduce soon after, leaving both a high field and low field PMR. The SdH oscillations at this high field would appear to have their peak heights determined by the slope of this high field PMR. This indicates that at a SdH peak, transport is in the bulk and the modulation dominates the behaviour. When in a trough the edge states are the dominant feature and the minima are well developed. Thermal broadening will cause both the Landau levels and the COs to become less well defined, electrons existing in a band around the Fermi level, rather than at a well defined E_F . In this latter case the commensurability criterion (Eqn. 2.2) occurs over a range of magnetic field values causing the oscillations to become wider and smaller. However this broadening is relatively minor below 10K. Thus the potential can be measured here without adversely affecting the result. It is preferable to measure at as low a temperature as possible to reduce this broadening. At low temperatures, though, the SdH oscillations are large and make measurements of peak height difficult. Thus most measurements are made at 5K to 10K. The carrier concentration was measured at 1.6K as the SdH oscillations at 5K are too small to use.

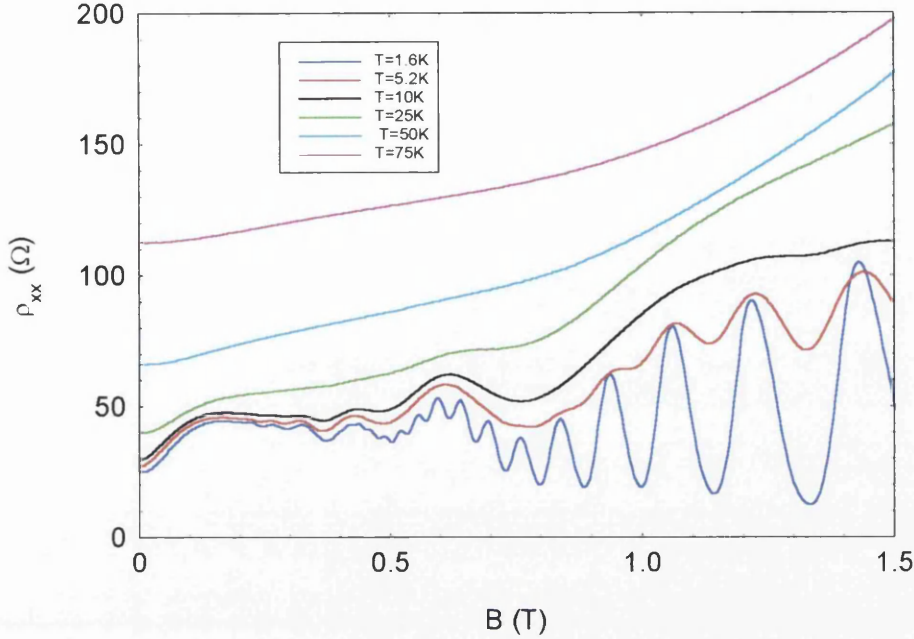


Fig. 5.17 Variation of magnetoresistance trace with temperature for sample 9, $[01\bar{1}]$.

The temperature dependence of COs has been studied by Beton et al [7]. They showed that the magnitude of a CO amplitude varies with temperature as follows;

$$\frac{\delta\rho_{xx}}{\rho_0} = \left[\frac{T}{T_a(B)} \right] \text{csc} h \left[\frac{T}{T_a(B)} \right] \quad (5.1)$$

where $k_B T_a(B) = \frac{\eta\omega_c k_F a}{4\pi^2}$. It should be noted that they have assumed that the

temperature effects on the mean free path are small. There is however a significant temperature difference associated with the scattering rate which is linearly dependent on temperature [8]. Thus this condition may not hold at higher temperatures.

In Figs. 5.18 and 5.19 we plot the CO amplitudes against temperature, together with the theoretical values from Eqn. 5.1

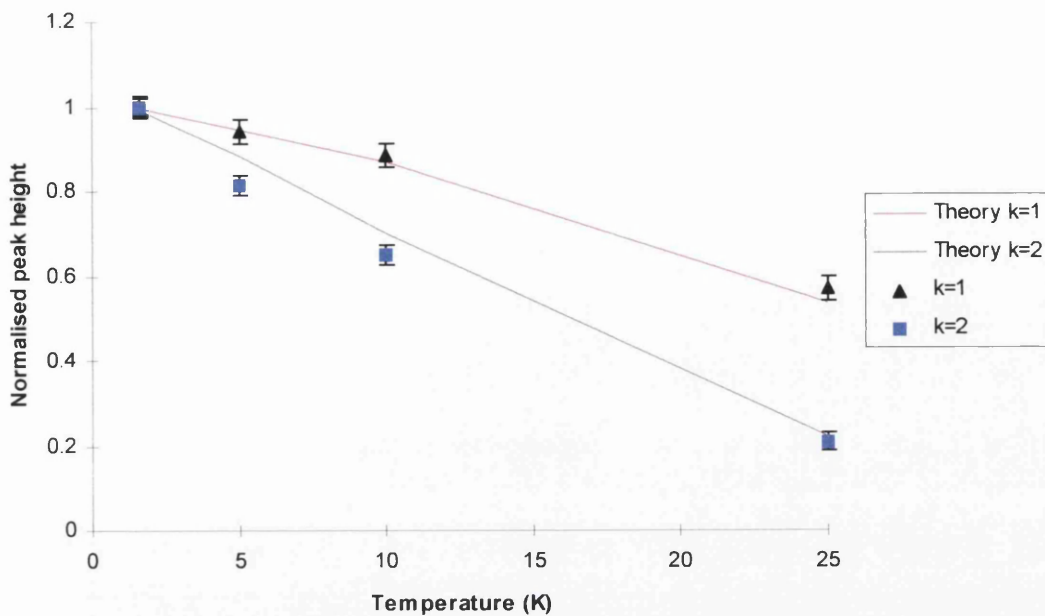


Fig. 5.18 The peak and trough magnitudes for sample 9 $[011]$ against Temperature. Peak heights have been normalised to unity at 1.6K

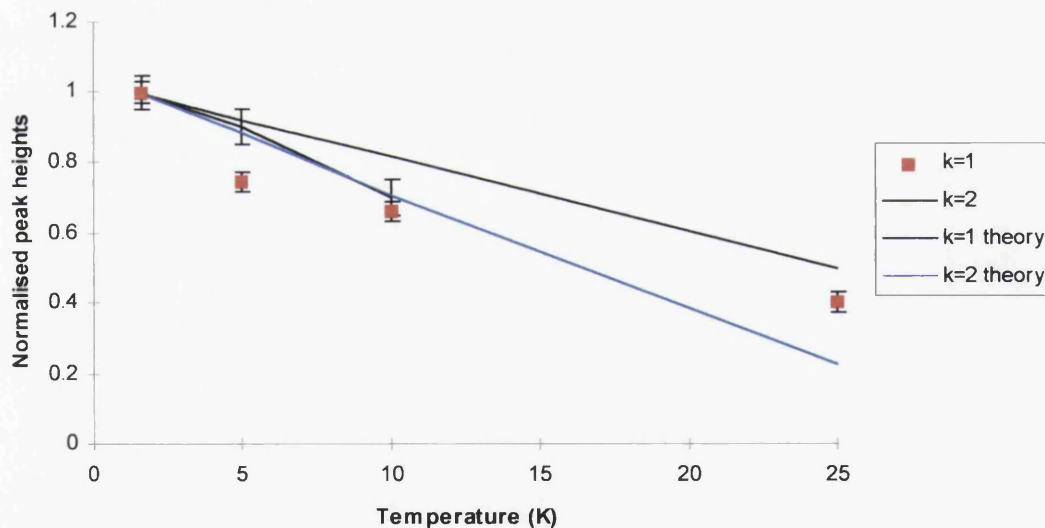


Fig. 5.19 The peak and trough magnitudes for sample 9 $[01\bar{1}]$ against Temperature. Peak heights have been normalised to unity at 1.6K

Generally agreement between theory and experiment is good, particularly for $[011]$. In the case of $[01\bar{1}]$ the $k=1$ experimental values do not correspond to theory as well as the other results. It is believed this is due to the value at 1.6K being incorrect, the increased SdH and second harmonic CO interference making it more difficult to

accurately measure the trough magnitude. The remaining values are then offset by the normalisation. Also, the $k=1$ trough is inherently more difficult to accurately measure. This is due to there being no easily identifiable point at which the trough becomes part of the high field PMR.

References

- [1] C.J. Emeleus, B. Milton, A.R. Long, J.H. Davies, D.E. Petticrew and M.C. Holland. *App. Phys. Lett.* **73** 1412 (1998)

- [2] G. Muller, P. Streda, D. Weiss, K. von Klitzing, G. Weimann. *Phys. Rev. B* **50** 8938 (1994)

- [3] C.W.J. Beenaker *Phys. Rev. Lett.* **62** 2020 (1989)

- [4] I.A. Larkin, J.H. Davies, A.R. Long and R. Cusco *Phys. Rev. B* **56** 15242 (1997)

- [5] P.H. Beton, E.S. Alves, P.C. Main, L. Eaves, M.W. Dellow, M. Henini, O.H. Hughes, S.P. Beaumont, C.D.W. Wilkinson *Phys. Rev. B* **42** 9229 (1990)

- [6] E. Skuras, M.C. Holland, C.J. Barton, J.H. Davies and A.R. Long *Semicond. Sci. Technol.* **10** 922 (1995)

- [7] P.H. Beton, P.C. Main, M. Davison, M. Dellow, R.P. Taylor, E.S. Alves, L. Eaves, S.P. Beaumont and C.D.W. Wilkinson. *Phys. Rev. B.* **42** 9689 (1990)

- [8] T.Kawamura and S. Das Sarma *Phys. Rev. B* **42** (1990)

Chapter 6 100nm and 200nm period LSSL, high temperature results

6.1 Introduction.

This chapter will deal with the 100nm samples first, followed by the 200nm samples. These were produced on identical hall bars to the 300nm period structures. For the 100nm samples a 50nm mark, 50nm space pattern was produced in the resist mask and dry etched. The samples were measured in the same way as the previous 300nm samples and also at low temperatures in the dilution fridge. This chapter will deal with the higher temperature ($>1K$) results.

In the case of the 200nm samples, a mark:space ratio of 100nm:100nm was used. Only high temperatures ($>1K$) were used to measure these samples, due to a lack of time.

6.2 100nm samples.

6.2.1 Basic features

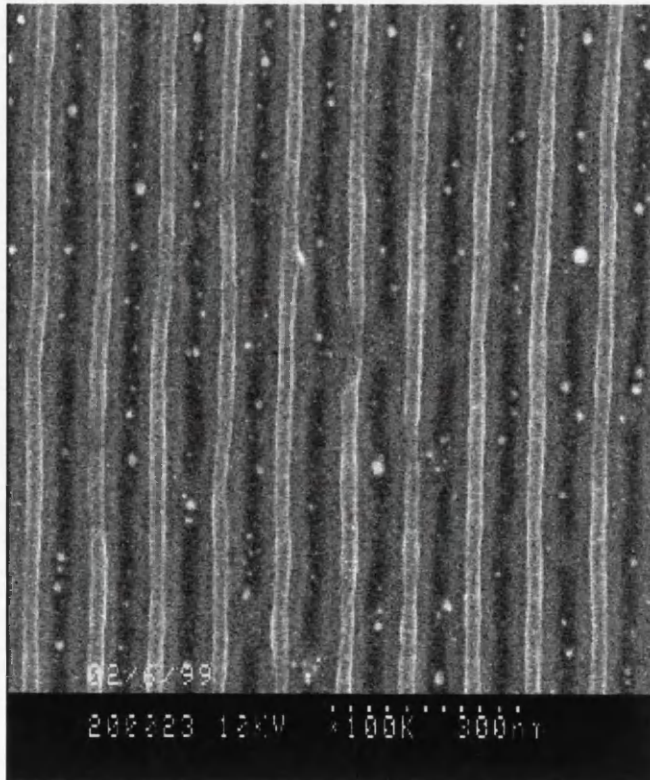


Fig. 6.1 SEM micrograph of 100nm period etched surface.

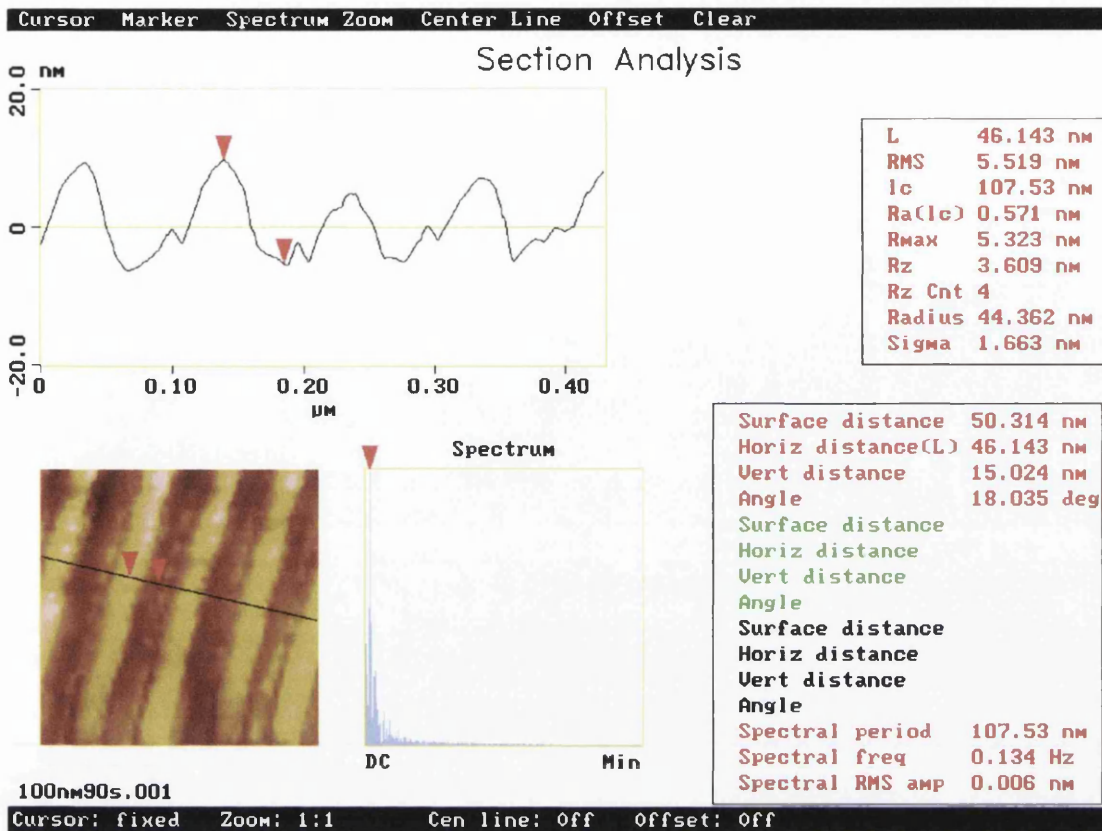


Fig. 6.2 AFM analysis of 100nm LSSL, 90s etch time. A vertical distance of 15nm is measured between the two red markers. The AFM tip has a diameter of 20nm and a length of 100nm

Two etch times (60s and 90s) were used with the 100nm samples. Only dry etching was used as it was believed to be a more accurate method of fabrication. This is due to the etch times involved being longer. Thus any error in the etch time should be proportionately smaller. Unfortunately, there is an induction time to be considered with dry etching. This is the time taken for the etching plasma to be formed, which can vary. However, as all samples, both stressor and control, are etched together, at the same time, there is no variation of etch time between samples. This can not be said for wet etching, where each sample is individually dipped in the etching solution. Fig. 6.1 is a SEM micrograph of a 90s etch time device. This has been etched rather deeply. Also, re-deposition of in-volatile Indium compounds is visible as little light coloured lumps in the base of the trenches. Due to the high amount of etching, the resist mask has begun to degrade while still in use. This is the most likely explanation of the sloping nature of the trench walls. It is believed that the piezoelectric strain originates from the edges of the stressor material at the strained boundary, thus the effective

mark:space ratio should be calculated from here. An AFM investigation (Fig. 6.2) showed the depth of the trenches to be approximately $14 \pm 2 \text{ nm}$ deep.

We believe that some of the unevenness of the tops of the ribs can be attributed to resist scum. When the sample is being dry etched, the resist mask becomes hardened by the plasma. It thus becomes harder to remove than normal. This resist can, therefore, remain after the usual cleaning process, and lead to errors in estimations of the depth. This scum should not affect the piezoelectric potentials created, as that arises from the InGaAs layer, not the resist. Some of this scum can also be seen in the base of the trenches. It is not immediately obvious what is scum and what is indium re-deposition.

These samples show similar anisotropy to the 300nm samples, in their magnetoresistance traces, but with a number of interesting differences.

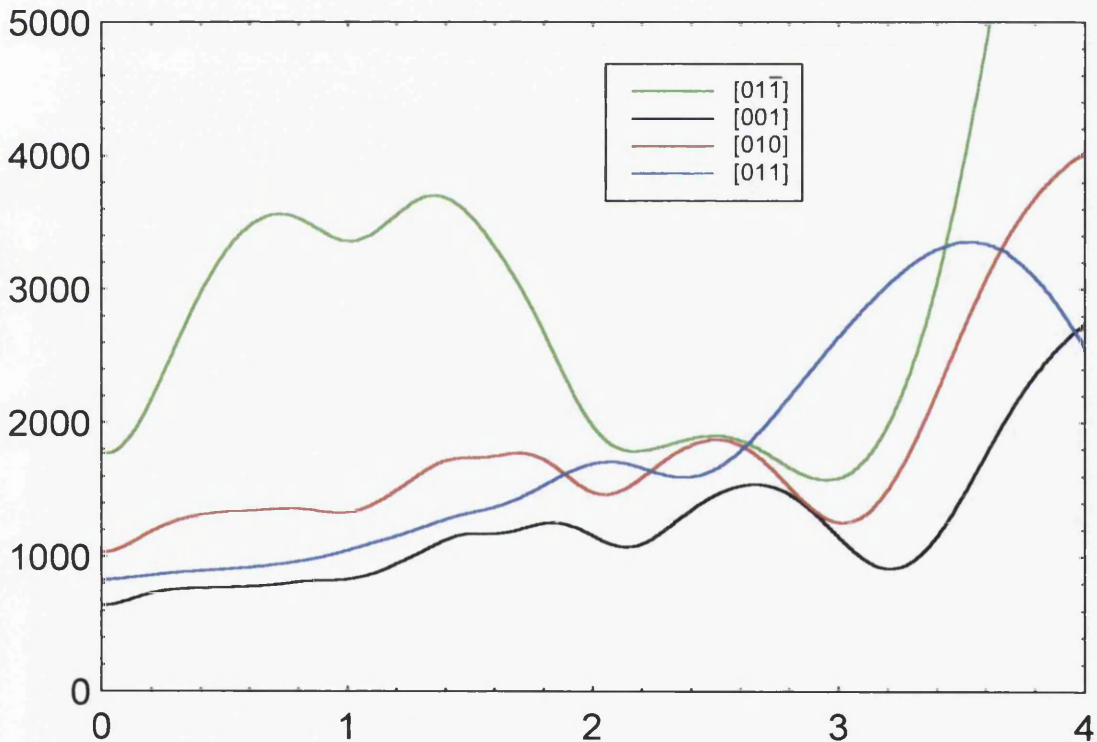


Fig. 6.3 Sample 11 measured at 10K

Sample 10 (60s etch) gave a very small potential but sample 11 (90s etch) seemed to be almost perfect. The potential was large enough to have begun to deplete the 2DEG without reducing the quality of the CO observed. Fig. 6.3 shows the four measured directions without gate bias. $[01\bar{1}]$ has a very large low field PMR peak and

strong CO. As the period of the modulation has been reduced, this reduces the size of cyclotron orbit required to interact with the potential. Thus the commensurability oscillations occur at higher field. Due to the high field the SdH oscillations are large, even at 10K. This interferes with the $k=1$ minimum which should lie at about 2.5T. This does not affect $[01\bar{1}]$ a great deal as the commensurability oscillations are large. In $[010]$ and $[001]$ the CO are not as big, however. Thus the SdH oscillations modulate the CO quite heavily. In the $[011]$ direction there is no modulation to be seen, other than SdH oscillations. From the previous arguments about the change of sign of the piezoelectric potential with direction this would seem to indicate that the surface effect is exactly equal and opposite to the piezoelectric effect in this direction. Further, there are no harmonics to be seen in any of the traces. This does not entirely agree with the theory. From Larkin et al [1], the second harmonic should be significant at this period, becoming zero at a period of approximately 400nm (Fig. 2.6). However, as the mark:space ratio is not exactly 1:1 then the magnitudes of the graph obtained from Larkin et al will change (Fig. 6.4). As this shows, the second harmonic is indeed much smaller, in comparison to the fundamental, for the non 1:1 mark:space ratio.

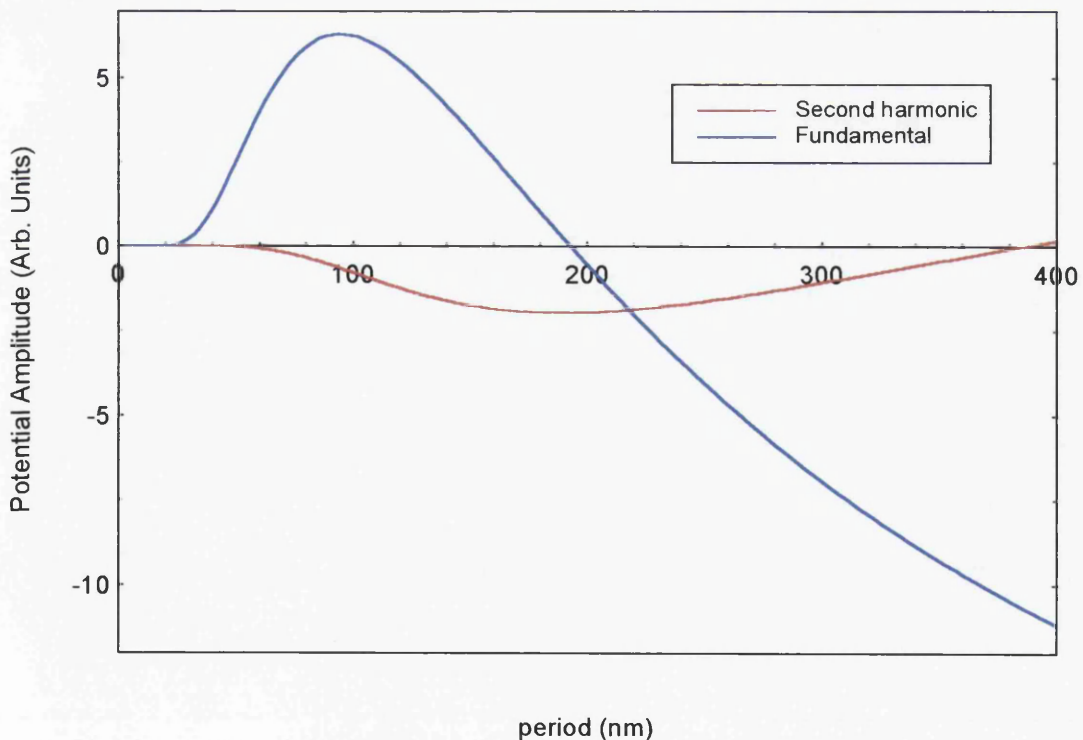


Fig. 6.4 Theoretical potential magnitudes for sample 11. Mark:space ratio of 15:7 estimated from SEM micrograph Fig. 6.1 and the AFM analysis, Fig. 6.2

It should be noted that the addition direction in this sample is at right angles to that in the 300nm data. This is a consequence of the Larkin et al [1] theory as explained in Chapter 2 and can be seen in Fig. 6.4, where the fundamental changes sign at a period of 200nm. This is a strong confirmation that we are dealing with a predominantly piezoelectric induced modulation.

If a Fast Fourier Transform (FFT) of the data in Fig. 6.3 is calculated then the trace seen in Fig. 6.5 is obtained. This picks out periodic effects in the magnetoresistance traces. The peaks at approximately 2T in all the traces except [011] can be attributed to the CO. The lack of a further peak at 4T rules out any second harmonic content. The peak that occurs between 5T and 7T in all four traces is due to the SdH oscillations. The trace for [011] has no peak at 2T, further reinforcing the belief that the various periodic potentials have combined to zero. The SdH peak is small in this example, due to the measurement being taken at 10K. If a lower temperature was used then the peak attributable to the SdH oscillations increases, with no change in the peak due to the CO. Thus, while it is useful to study the magnetoresistance at higher temperatures, to reduce SdH interference, this choice does not affect the FFT results.

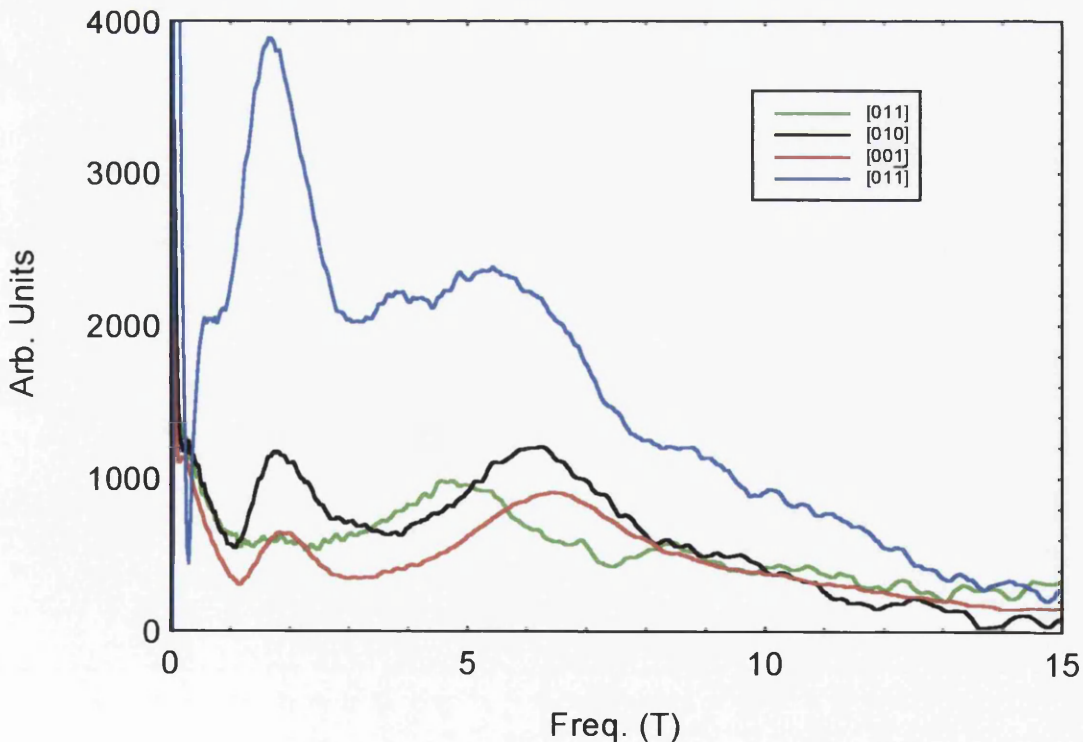


Fig. 6.5 Fast Fourier Transform of the traces in Fig. 6.3

6.2.2 Gate effects.

Once again the voltage upon the gate was modified to alter the density of the 2DEG (Fig. 6.6). This time no additional modulation was seen. We believe that this is due to the etched troughs being too narrow for a significant level of metal to be deposited within, especially towards the base due to the sloping walls. Thus the modulation of the gate to 2DEG distance is slight. This will be discussed further in the following section.

Although the gate itself does not appear to change the magnitude of the potential, it does alter the traces seen. With positive gate bias the number of electrons in the channel is increased. This reduces the overall resistance and allows more CO to become visible. This can be useful when estimating potential magnitudes. Additional minima between the low field PMR peak and the $k=2$ minima ensures that there is no interference between the two. Thus a more accurate estimate of the position and magnitude of the $k=2$ minima and low field PMR peak can be obtained. However, this increase in carrier density also increases the number of SdH oscillations seen. Thus the interaction between the CO and the SdH becomes greater. Hence, once again, a trade off has to be made between the quality of the COs observed and the accuracy of the potential magnitudes calculated.

Fig. 6.7 shows the voltage effects on a [001] device. The effect on the SdH oscillations is more prominent, due to the reduced size of the CO, but similar effects to those seen in Fig. 6.6 can be observed occurring to the CO in Fig. 6.7.

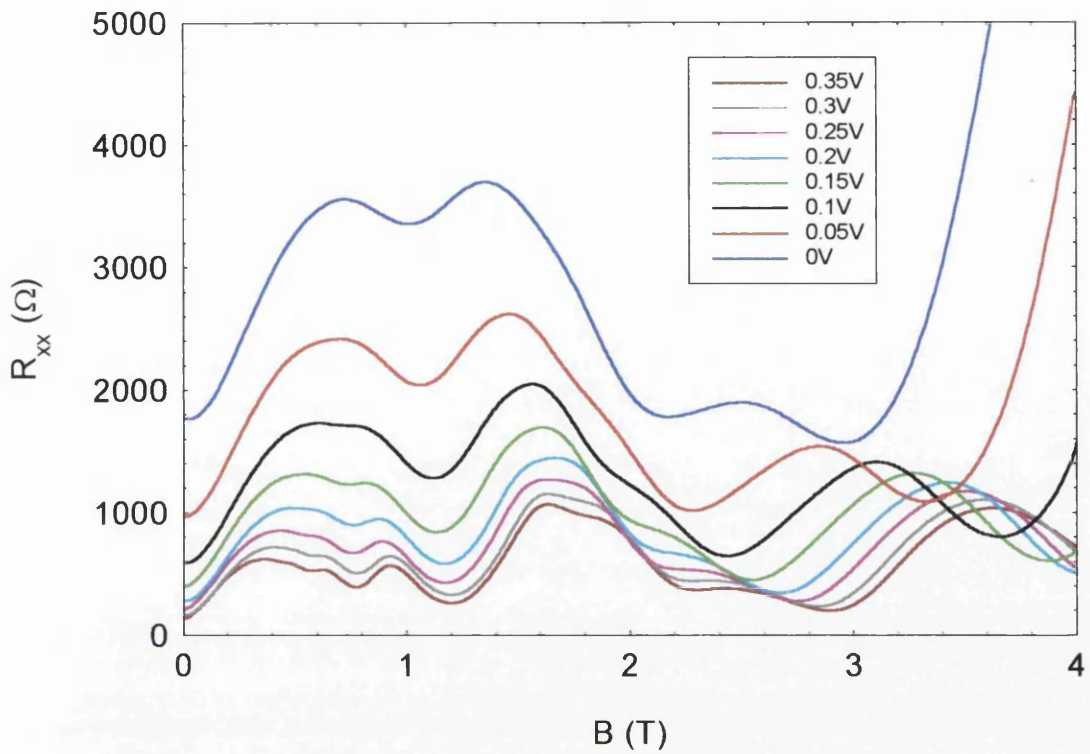


Fig. 6.6 Variation of magneto-resistance traces with gate voltage for $[01\bar{1}]$ at 10K

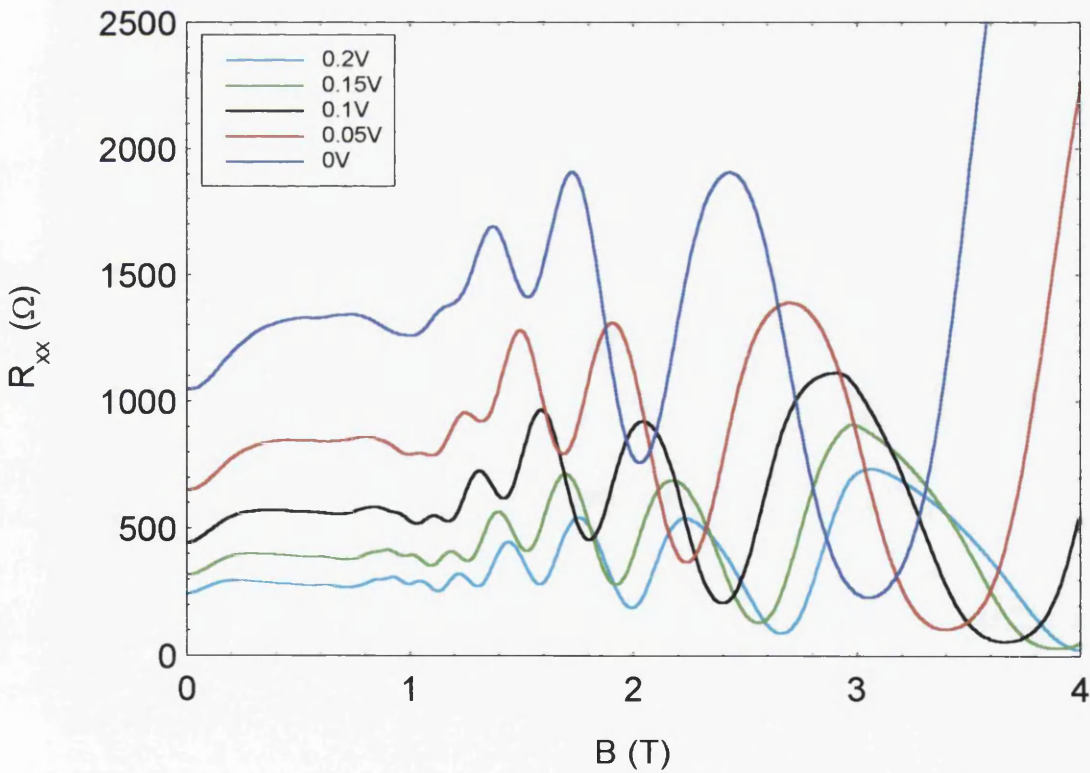


Fig. 6.7 Voltage effects for $[001]$ device.

6.2.3 Potential Magnitudes.

There were no visible COs in the [011] direction at any bias and hence the total periodic potential is zero. For the other three directions the potentials can be calculated as before. Results for $[0\bar{1}\bar{1}]$ and [001] can be seen in Fig. 6.8. The results for [010] are similar for [001] due to the piezoelectric effect equalling zero in these directions. As can be seen, especially for large negative gate voltage, [001] does not have a potential half that of $[0\bar{1}\bar{1}]$, as would be expected if the piezoelectric component was equal in absolute magnitude to the surface effect, i.e. $[0\bar{1}\bar{1}]=2*[001]$. This leads us to believe that the combination of the different potential components is not linear.

As no second harmonic is visible the two potential modulation calculation methods should give the same value in Fig. 6.8. This is obviously not the case. If there was a second harmonic present, then the PMR results would be greater than the CO results. This is also not the case. In these samples the Fermi level lies at approximately 14 meV at zero gate bias. Thus the results calculated from the CO magnitudes give a potential magnitude of approximately half the Fermi level. This is no longer a small perturbation. Thus investigation of the theoretical expression for analysing the effects of large potentials is required.

The gate would appear to have very little periodic effect. For [001] the potential calculated does not appear to change greatly with gate voltage. There is a change for $[0\bar{1}\bar{1}]$ but this may be due to the inaccuracies of the theory due to the potential modulation not being a perturbation of the Fermi level. Also, as the bias becomes more negative the number of electrons screening the channel from the potential source reduces. This, therefore, leads to a larger potential modulation at the 2DEG level. The reduction in carrier concentration also shifts the CO minima to lower field. This may lead to more interference between the low field PMR peak and the $k=2$ minima, thus increasing any error in estimating trough magnitudes.

This lack of periodic gate effect can be attributed to the reduction in the size of the troughs. Perhaps the gap is too narrow to allow a significant amount of gate metal to enter. Thus the variation in distance of gate to 2DEG is much reduced. Hence any periodic modulation of the 2DEG at a given gate voltage is similarly much reduced.

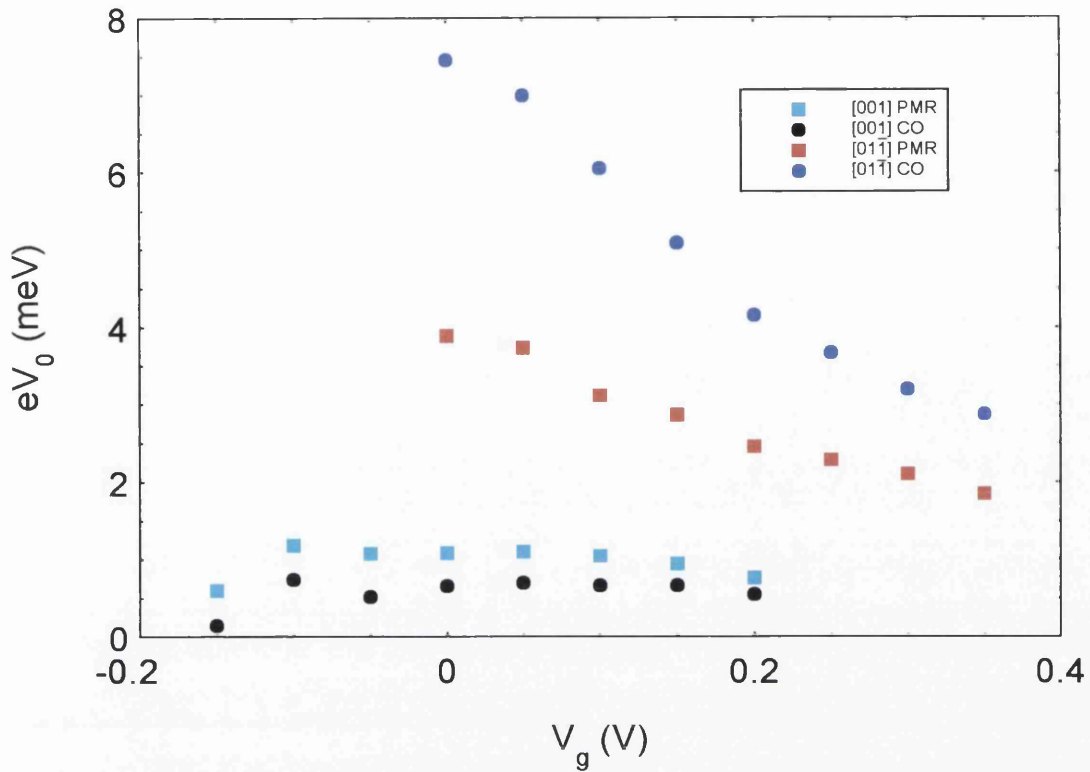


Fig. 6.8 100nm LSSL potentials at 10K

6.2.4 Temperature

Once again the temperature was varied and similar effects to those seen for a 300nm sample were seen (Fig. 6.9). The high field PMR is believed to again dictate the SdH peak heights. This is less obvious here due to the CO extending to higher fields. As can be seen the SdH peak between 2T and 3T is large. It is this that we were trying to reduce by measuring at higher temperatures. It can still be seen at 10K but, as we made use of the $k=2$ minima to estimate potential, we made all our measurements at this temperature. 10K appears to give an unchanged PMR peak and $k=2$ minima. However, $k=1$ is not as deep as before. We attribute this to the reduced effect of the SdH rather than a smearing of the CO, which has not been seen to have occurred at lower fields. Also, Beton et al [2] showed that the low field oscillations are quenched before higher field ones, further supporting this theory.

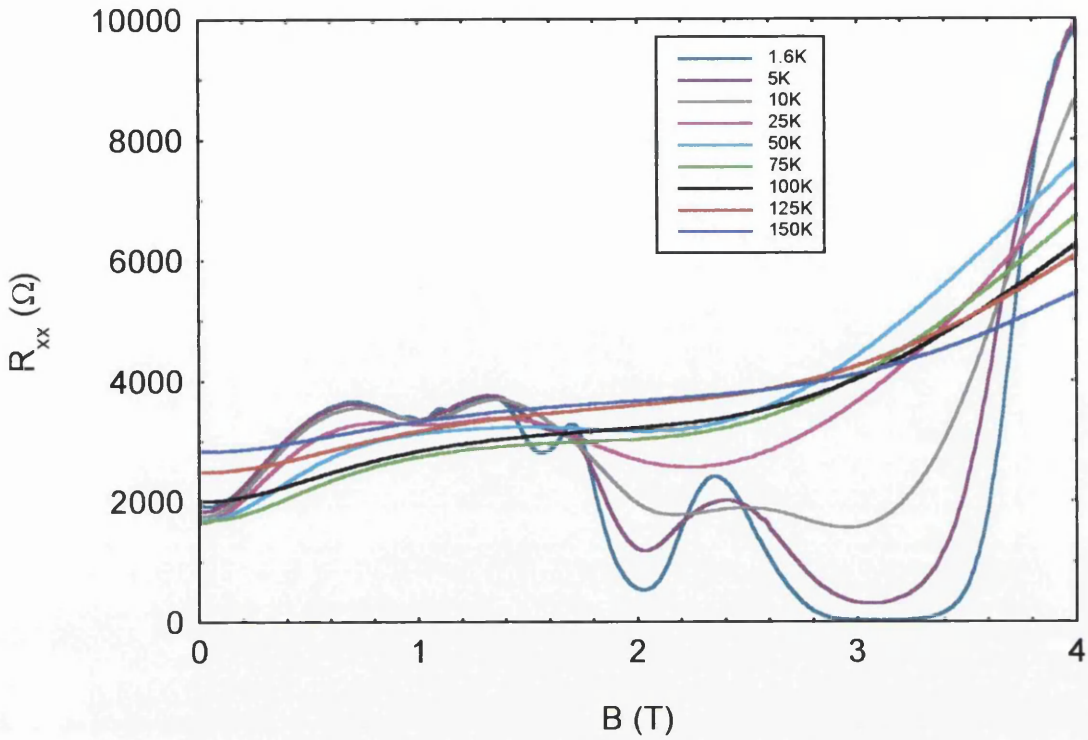


Fig. 6.9 Temperature dependence of sample 11. $V_g=0V$ $[01\bar{1}]$

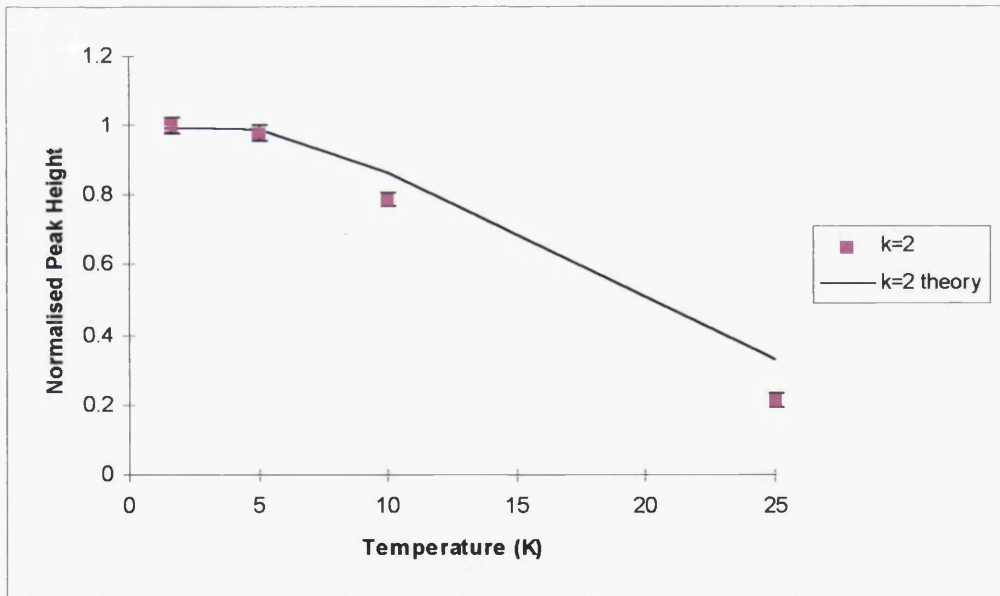


Fig. 6.10 $k=2$ trough depth against temperature for the $[01\bar{1}]$ sample. Heights have been normalised to unity at 1.6K

Similar analysis to that carried out in Chapter 5 can be done on the 100nm sample (Fig. 6.10). Unfortunately, the large SdH oscillations strongly affect the $k=1$ minimum, making it very difficult to make accurate measurements of the trough depth.

However, it can be seen that the experimental results for the $k=2$ minimum continue to follow the theory closely.

6.3 200nm samples

6.3.1 General features

The 200nm samples were fabricated as indicated above, except that a citric acid based wet etch was used to define the etched trenches. Unfortunately, due to time constraints, the etchant had not been fully studied. Thus the trenches created were too deep, as can be seen in Fig. 6.11.

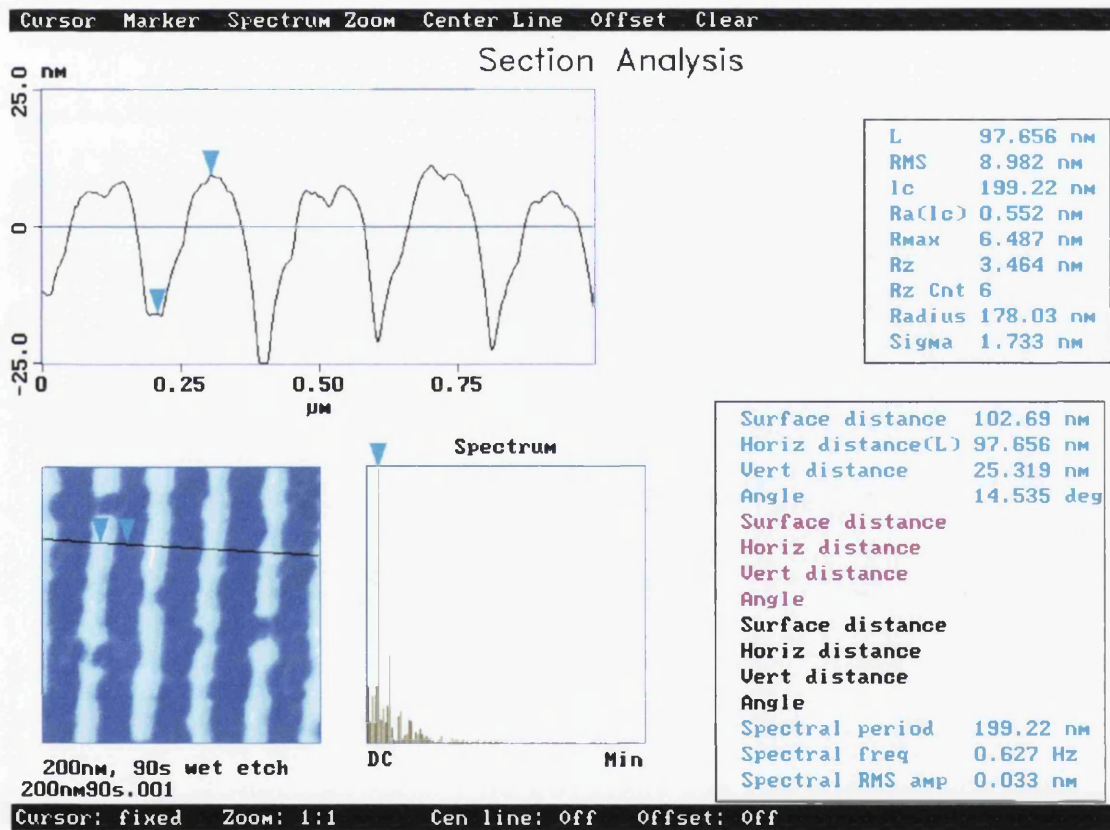


Fig. 6.11 AFM picture of 200nm period LSSL. Depth between two indicated points is 23.5nm, indicating an average depth of approximately 24nm.

As can be seen, the base of the trenches is not uniform. This, we believe, is due to the Indium re-depositing onto the surface, as it does not dissolve well in the etchant. As this is a wet, chemical, etch we do not expect any hardening of the resist

mask. Thus, we can assume that all the resist has been removed in the cleaning process.

Fig. 6.12 shows a magnetoresistance trace for this 200nm LSSL device. As can be seen, there is a very large zero field resistance, which can be attributed to the heavy etching. The carrier concentration has been largely reduced. However, if a gate bias is applied, then commensurability type oscillations can be seen in far forward bias (Fig. 6.13). These do not show any harmonic content and are isotropic in crystal direction. We believe that the stressor layer has relaxed, due to the excessive etching, such that there is no piezoelectric component. Also $\frac{d}{l} = 4$ which is expected to give a minimum value of the piezoelectric fundamental from Larkin et al [1] (See Section 2.3). Thus we are simply seeing the surface effect. This surface effect is large, due to the large change in surface height, created by the over-etching. This does, however, illustrate that in our previous samples we were well within the etching limit, and were in no danger of depleting the 2DEG.

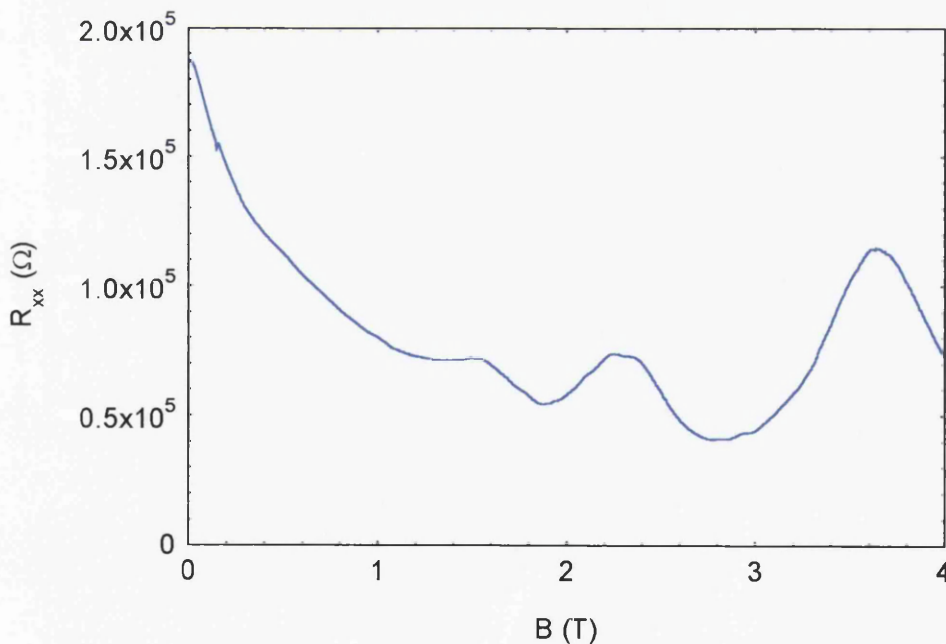


Fig. 6.12 Magnetoresistance against magnetic field for the 200nm LSSL, $V_g=0V$, $T=1.6K$, $[01\bar{1}]$

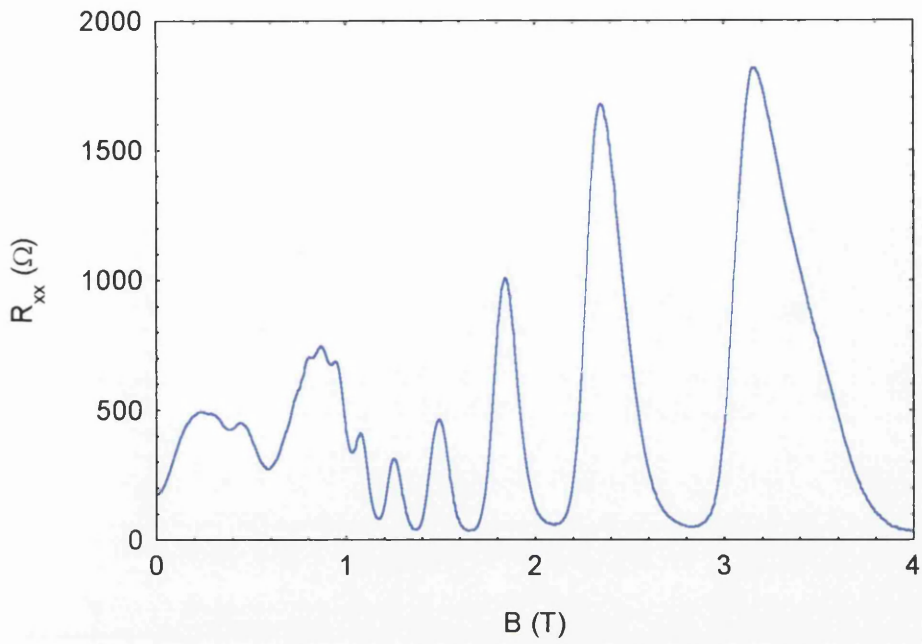


Fig. 6.13 Magnetoresistance against Magnetic field for the 200nm LSSL, $V_g=0.6V$,
 $T=1.6K$, $[01\bar{1}]$

References

- [1] I.A. Larkin, J.H. Davies, A.R. Long, R. Cusco. *Phys. Rev. B* **56** 15242 (1997)

- [2] P.H. Beton, P.C. Main, M. Davison, M. Dellow, R.P. Taylor, E.S. Alves, L.Eaves, S.P. Beaumont and C.D.W. Wilkinson *Phys. Rev. B.* **42** 9689 (1990)

Chapter 7 100nm period LSSL, low temperature results.

7.1 Introduction

This chapter will deal with results obtained at temperatures between 45mK and 800mK. The same samples used at the higher temperatures (Chapter 6) were used in these experiments. Thus the magnitude of the potential should be consistent and any differences should be due solely to different cooling cycles. As $[01\bar{1}]$ had the strongest potential, the majority of the experimental time was spent on samples in this direction.

7.2 Basic Features.

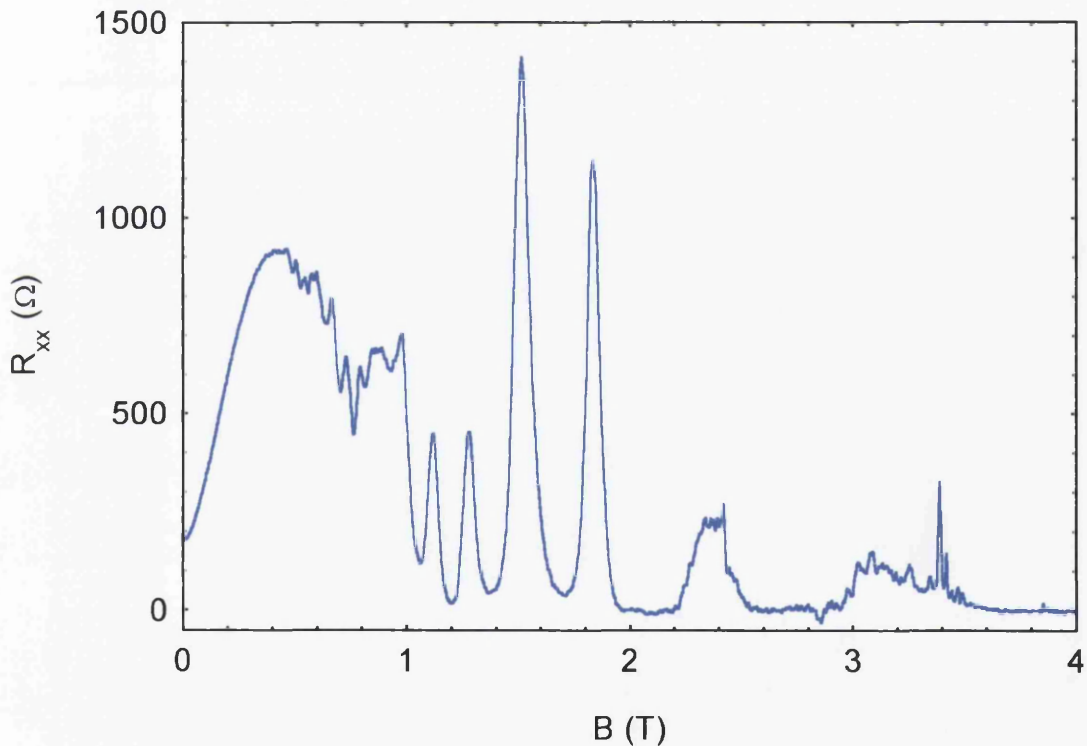


Fig. 7.1 $[01\bar{1}]$ $T=45\text{mK}$ $V_g=0.3\text{V}$

Due to the much reduced temperatures the SdH oscillations in these traces were much more pronounced (Fig. 7.1, positive gate voltage shown as it enhances the oscillations.). This is due to a large reduction in thermal broadening of the Landau levels. Thermal and electrical excitation of the 2DEG leads to broadening as the electrons at the Fermi energy are given extra energy. This causes the electrons at the

Fermi energy to spread out over a range of energy states. Hence, the conditions required for a Shubnikov-de Haas peak extend over a range of energies, and hence magnetic field, broadening the peaks seen. Broadening will, however, also come from external noise sources, either electrical or through sample heating. Extraneous signals are filtered out by the screened room, but it is very important to ensure that electronic broadening from the applied current does not have an effect. Thus the current supplied to the sample, via the current forming resistor, (also known as the excitation) is kept as low as possible, i.e. the excitation voltage $\ll \frac{k_B T}{e}$. Hence, this reduced broadening shows up as narrower SdH oscillations which have minima close to zero when the Landau levels are well spaced. Fig. 7.2 illustrates the effect of a change in excitation voltage.

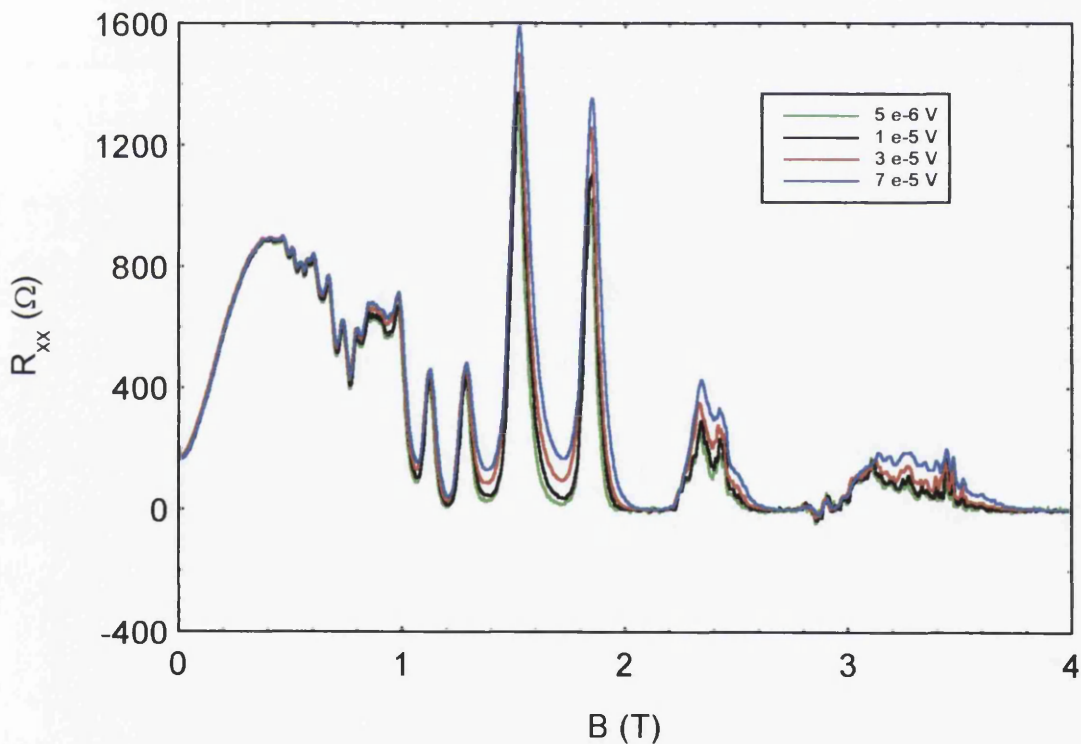


Fig. 7.2 Trace shown in Fig. 7.1 for differing values of excitation voltage

The CO can still be observed at 45mK (Fig. 7.1). Fig. 7.3 illustrates that the potential magnitudes are similar, for the two different temperature runs, as the PMR peaks occur at the same position of magnetic field. It can be seen that the interference between SdH and CO is very strong, thus making it hard to estimate the CO positions

with great accuracy. It was noting this interference in a mild way at higher temperatures and a wish to investigate it further that led to this experiment.

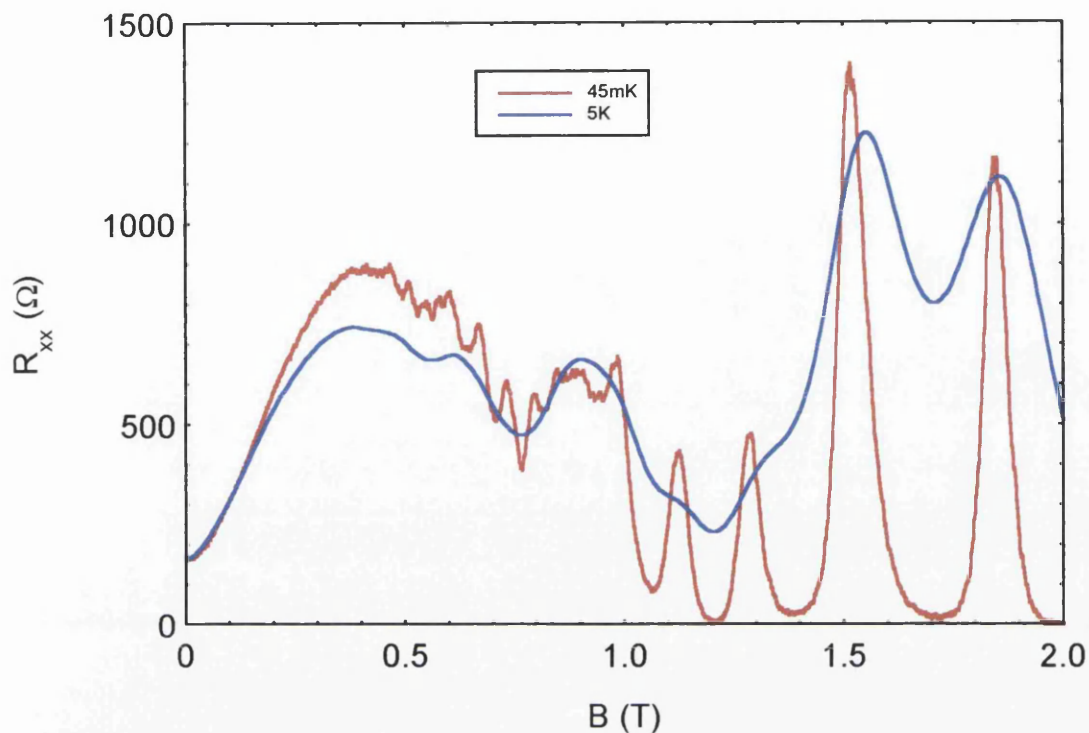


Fig. 7.3 Comparison between high and low temperature runs. $V_g=0.3V$

The trace, for a crystal direction of $[01\bar{1}]$ and a gate bias of $0.3V$, is divisible into three different sections. Section 1 (Fig. 7.4) covers the field range from $0T$ to $1T$. In this section the CO are the dominant effect. Section 2 (Fig. 7.5) ranges from $1T$ to $2T$. Here the SdH are dominant. Finally Section 3 (Fig. 7.6) covers fields above $2T$. Here we can see some interesting structure in the SdH peaks.

$$V_{nn'} = V_0 \left[\frac{n'!}{n!} \right] \exp\left(-\frac{1}{2} X\right) X^{\frac{(n-n')}{2}} l_n^{n-n'}(X) \operatorname{Re}(e^{iKx_0} i^{n-n'}) \quad (7.1)$$

where $X = \frac{1}{2} K^2 l^2$, $K = \frac{2\pi}{a}$ and $l = \sqrt{\frac{h}{2\pi e B}}$

This change in energy caused by the perturbation is calculated from;

$$\Delta E_{2n} = \frac{\sum_{n'} |\langle n | V_{nn'} | n' \rangle|^2}{E_n - E_{n'}} \quad (\text{Fig. 7.2})$$

This produced, for integer values of Landau Level number, the result seen in Fig. 7.5.

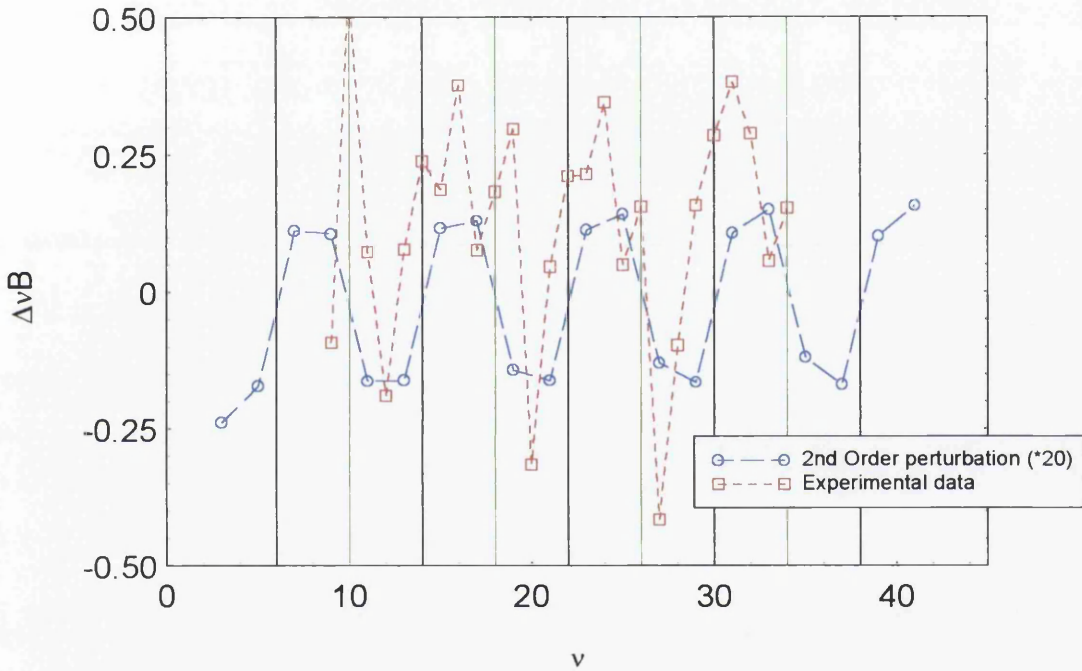


Fig. 7.5 Second order perturbation calculation. Second order perturbation multiplied by twenty for clarity. Black lines indicate CO minima, green lines indicate CO maxima.

This graph shows $\Delta\nu B$, which is the shift of the SdH peak from its expected position, where $\Delta E = \frac{h}{2\pi m^* e} (\Delta\nu B)$. This is calculated experimentally by plotting B position of peak against filling factor. In an unpatterned sample, this should rise linearly as

$$B = \frac{h n_{2D}}{e \nu} \quad (7.3)$$

Therefore, multiplying the B position by the filling factor should give a flat line

with value $\frac{hn_{2D}}{e}$.

Thus if we calculate the deviation from this expected straight line we can get

$\Delta(\nu B)$;

$$\Delta(\nu B) = \nu B - \langle \nu B \rangle \quad (7.4)$$

where $\langle \nu B \rangle = \frac{hn_{2D}}{e}$

This we then compare to the perturbation term. As can be seen, the periodic nature of the experiment is partially seen in the theory. There appears to be more structure in the experimental results, but the overall period matches. This is to be expected as the mean Landau level energies oscillate the CO period.

Unfortunately, the magnitude of the experiment is ten times that of the theory. Thus further analysis was carried out, based on a different model.

It has been shown by Zhang and Gerhardt [1] Vasilopoulos and Peeters [2] that the Landau level width Γ is modulated quantum mechanically by a periodic potential as follows;

$$\Gamma = V_0 \pi^{-\frac{1}{2}} X^{-\frac{1}{4}} \cos\left(2\sqrt{X} - \frac{\pi}{4}\right) \quad (7.5)$$

where $X = \left(\frac{\pi R_C}{a}\right)^2$. The argument of the cosine term is the same here as in the

Beenaker expression for the COs. Hence, at a CO minimum Γ is predicted to be zero. This is known as the “flat band” position. This is a first order effect and is therefore expected to be stronger than the second order movement of peaks calculated above.

Further, Raikh and Shahbazyan [2] have explained how a change in the width of the Landau level modifies the density of states. They explain how the density of states (g) in the Landau levels are affected by random scatterers, which changes the density of states of the Landau levels by δg , in the following manner;

$$\frac{\delta g}{g} = 2 \cos\left[\frac{E}{h\omega_c} - \frac{1}{2}\right] \exp\left(\frac{\Gamma^2(E)}{h^2 \omega_c^2}\right) \quad (7.6)$$

where $\Gamma(E)$ is the width of a Landau level at energy E due to a scattering potential.

As both a periodic potential and random scatterers are present in our samples they both should be taken into account. Hence, if the width modulation due to the scattering potential and the periodic modulation are combined in quadrature to give a total width ($\Gamma^2 = \Gamma_{width}^2 + \Gamma_{periodic}^2$) the density of states can be calculated. For this calculation we write $\Gamma_{random}^2 = \frac{\Gamma_0^2 a}{R_c}$, where Γ_0 is a fitted value, here equal to 1 meV.

If the periodic potential is equal to zero then the exponential term becomes equivalent to the quantum mobility as follows;

$$\frac{\Gamma_{E_F}}{h^2 \omega_c^2} \equiv \frac{\pi}{\mu_q B} \quad (7.7)$$

Thus a quantum mobility can be calculated from the fitted value. For these results a value of $1.44 \text{ m}^2 \text{V}^{-1} \text{s}^{-1}$ was calculated, comparing with an experimental value of $2 \text{ m}^2 \text{V}^{-1} \text{s}^{-1}$. This experimental value was calculated from an unpatterned sample, with the same carrier concentration as the patterned sample.

The density of states can then be plotted as a function of magnetic field to obtain Fig.7.6.

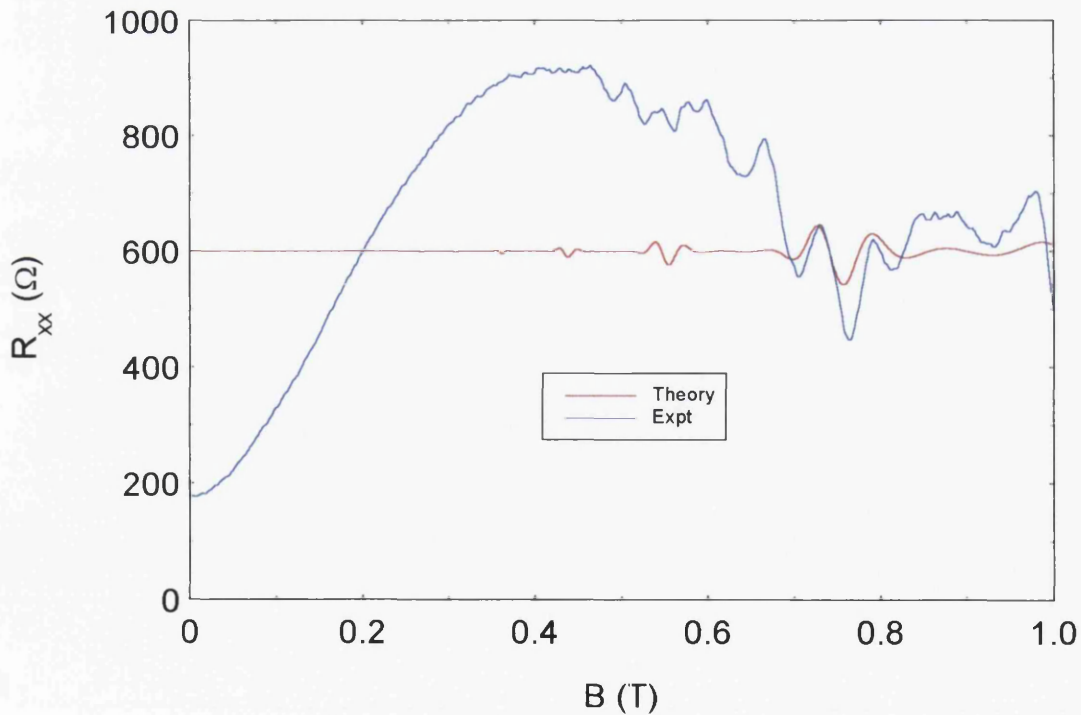


Fig. 7.6 DOS perturbation calculated from the Raikh and Shahbazyan based model, compared to the experimental result. The theoretical results have been scaled to have an initial resistance of 600Ω

As can be seen the calculated modulation of the SdH oscillation heights with magnetic field clearly follows the experimental trend. The lower field, higher CO order, oscillations are hidden behind the PMR peak. This behaviour has not been seen previously due to the majority of experiments being carried out at higher temperatures or with a smaller periodic potential. We do believe, however, that the argument presented above satisfactorily explains the observations.

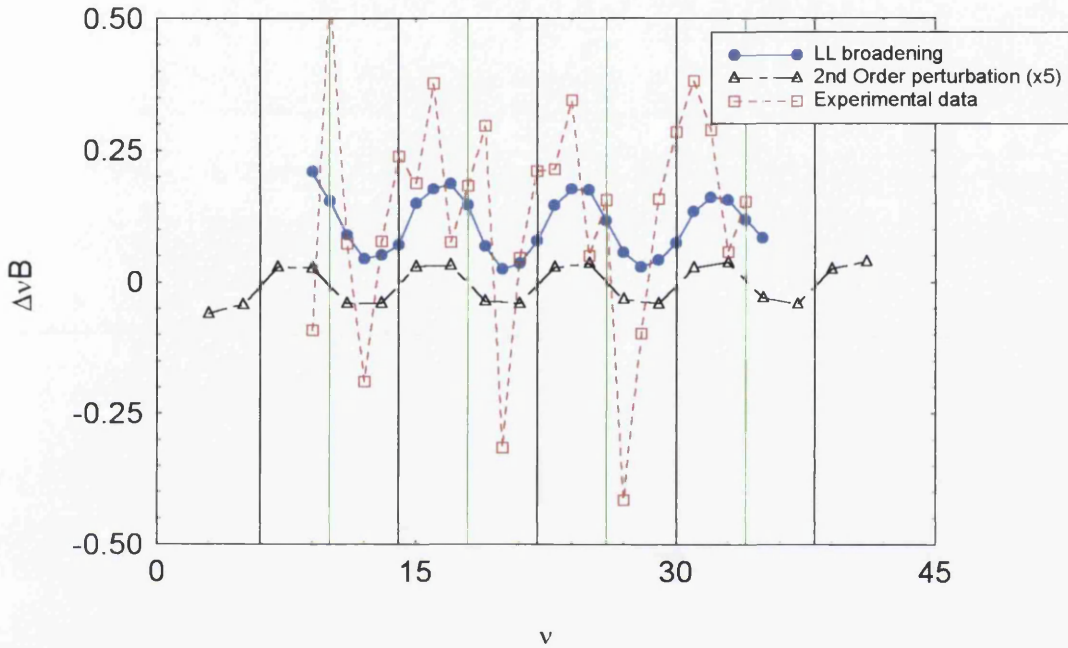


Fig. 7.7 SdH oscillation displacement against filling factor. Second order perturbation multiplied by five for clarity. Black lines indicate CO minima, green lines indicate CO maxima.

Further confirmation can be seen from an analysis of the peak positions of the oscillations produced by this theory. Peak plotting against filling factor can be done for the theoretical results plotted in Fig. 7.6, in the manner outlined above and illustrated in Fig. 7.7.

Fig. 7.7 shows that a similar periodic offset is observed but, the magnitude of the effect is much closer to that seen in the experimental results than for the perturbation calculation.

From the results obtained we believe that Section 1 occurs when the Landau levels overlap. It is the degree of overlap which is modified by the periodic potential to produce the traces seen.

7.4 Section 2 (1T to 2T)

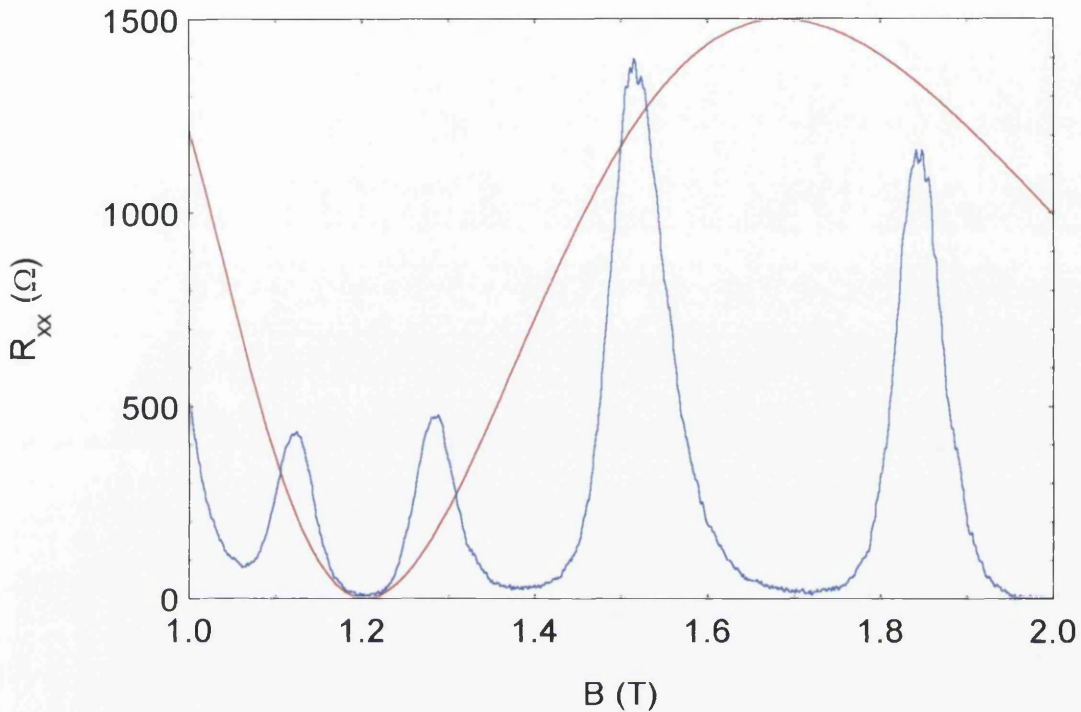


Fig. 7.8 Section 2 $[01\bar{1}]$ $T=45\text{mK}$ $V_g=0.3\text{V}$ Red curve indicates theoretical position of Commensurability Oscillations.

In this region the Landau levels no longer overlap, even when the additional broadening term is taken into account. Hence we see well defined SdH oscillations with minima very close to zero, as one expects in an unperturbed 2DEG. The maxima of the oscillations are of interest however. As can be seen in Fig. 7.8 the peaks do not follow the usual exponential envelope as would be seen in an unpatterned Hall bar. There is a reduction in the size of the oscillations where we would expect a minima in the commensurability. Similarly there is an increase in the peak heights where we would expect a CO maxima. This behaviour does not seem to affect the SdH minima however. It should be noted that this is the opposite to Section 1 where large SdH oscillations were seen at CO minima.

While we have no formal theory for this effect we believe the following is occurring. When the Landau Levels are well separated and the bulk Fermi level lies between Landau Levels, conduction is in edge states and R_{xx} approaches zero. If the Fermi level lies in a Landau Level then conduction is in the bulk. Thus, at this point bulk effects should dominate. Hence R_{xx} is dominated by the periodic potential at this point. Hence the peak height resistance is determined by the Beenaker style magnetoresistance values. This is a similar effect to the one we saw in the high field PMR at higher temperatures (Chapter 5.6).

7.5 Section 3 (above 2T)

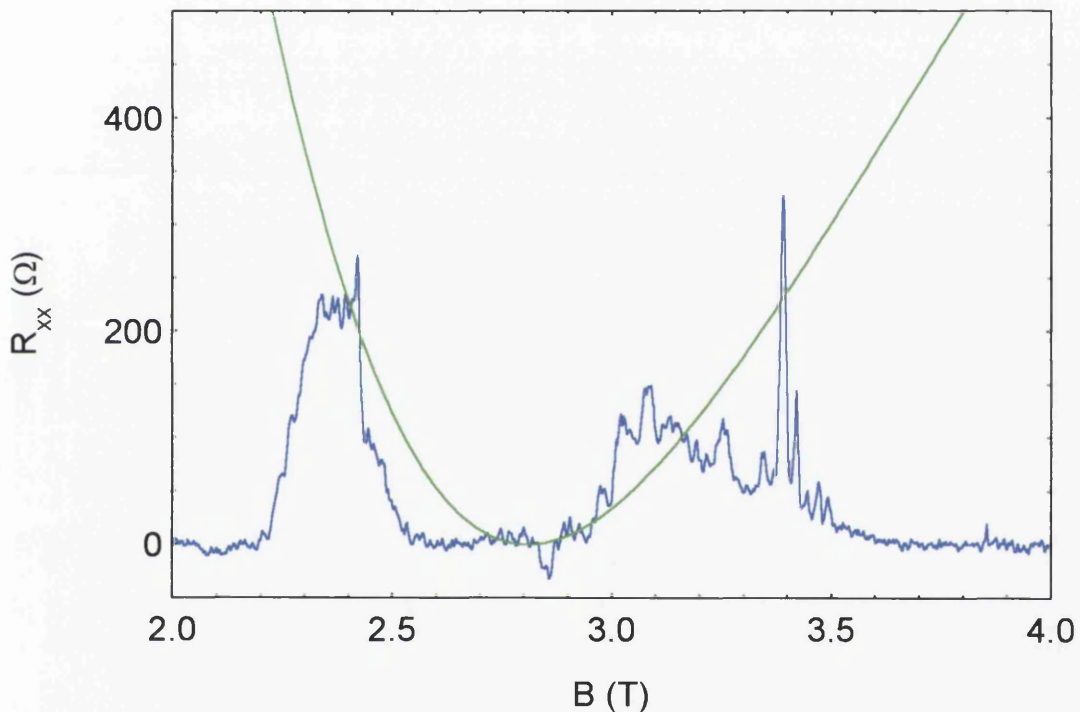


Fig. 7.9 Section 3 $[01\bar{1}]$ $T=45\text{mK}$ $V_g=0.3\text{V}$ Green line indicates theoretical position of Commensurability Oscillation.

Fig. 7.9 shows Section 3. The $k=1$ minima for the CO should occur at approximately 2.5 T, as the green line indicates. Thus we can assume that the SdH oscillations in the region displayed are reduced by the same mechanisms as explained in the previous section. However, as can be seen the SdH oscillations are no longer smooth. The major structures observed are not noise, as the random noise level is approximately $\pm 5\Omega$. The major features, however, such as the sharp peaks at

approximately 3.4T are reproducible. Also reproducible is the negative resistance at approximately 2.8T.

If a similar sweep is run, measuring the voltage along the Hall bar using the pair of voltage probes on the opposite side of the Hall bar to normal, a different trace is obtained (Fig.7.10). There is still an indication of the peak splitting up but it is not as obvious. A similar run was also carried out on a different device. It was manufactured in the same way at the same time, but on a different part of the initial wafer. As can be seen (Fig.7.10) this also shows anisotropy between the two measurement sides as well as splitting up of the peaks. This indicates that a sample specific effect is present in this region.

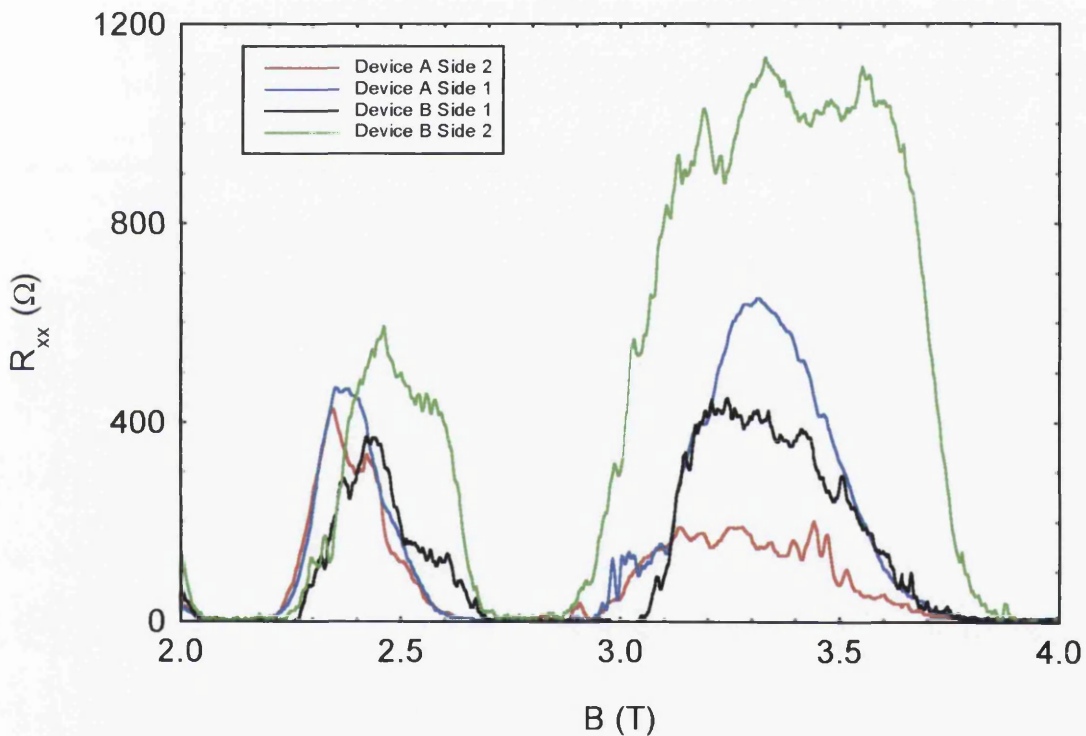


Fig 7.10 Anisotropy and small structure visible at high fields at 45mK, $V_g = 0.3V$
 Device A side 2 here corresponds to the trace shown in Fig. 7.9

It was decided to run an unpatterned Hall bar, produced on the control wafer, in the dilution fridge to see if the structure in the high field peaks was due to the periodic potential (Fig.7.11). It can be seen from this trace that the high field SdH oscillations again show pronounced structure. It should also be noted that the peaks in the equivalent of section two do not increase linearly as would be expected. Thus this

unknown source of modulation has to be taken into account when trying to understand the modulation of the peak heights seen in Fig. 7.8.

Therefore, these low energy, high frequency oscillations are neither a product of the periodic potential, nor the InGaAs layer. Possibilities could include; AlGaAs clustering, dopant clustering or quantum confinement in some area. We do not understand this phenomenon at present and much work, possibly involving TEM studies of the grown layers, is required.

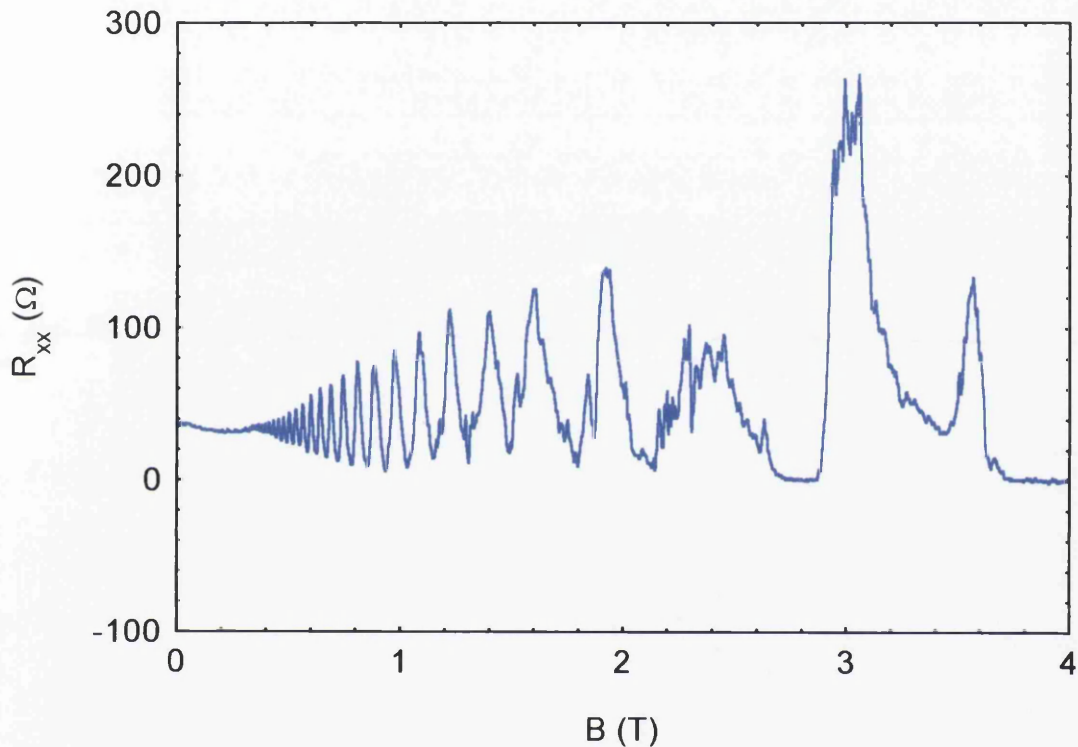


Fig. 7.11 Unpatterned control wafer (i.e. no InGaAs stressor layer) at 45mK, $V_g = 0.3V$

7.6 Temperature dependence.

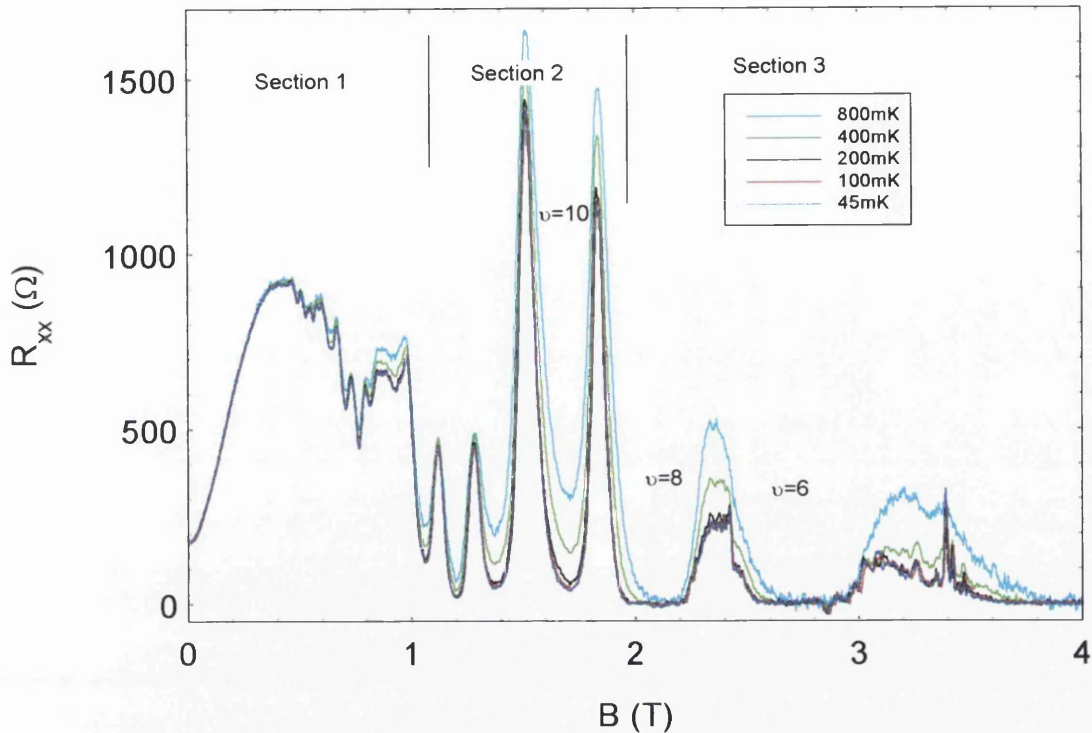


Fig. 7.12 Temperature effects $[01\bar{1}]$ $V_g=0.3V$

Fig. 7.12 shows the temperature effects on the complete characteristic, which are pronounced. As is to be expected, the SdH oscillations begin to die out in Section 1. The minima in Section 2 become less well defined as thermal broadening causes the Landau levels to overlap. Interestingly the maxima of the SdH also rise in resistance. This could be due to the strong SdH pulling the CO maxima down. Both these effects are much more pronounced at the CO maximum at $\nu=10$ than at the CO minima at $\nu=14$ (the flat band position). Overall, as the temperature rises, the SdH oscillations weaken, and the CO structure reasserts itself.

The extra structure of section 3 begins to disappear at 400mK. By 800mK there is very little left, most of the structure being thermal noise. This indicates that these are low energy effects and thus indicates that they are likely to be of a quantum mechanical origin, while also having a sample specific component, as mentioned earlier.

7.7 Voltage effects

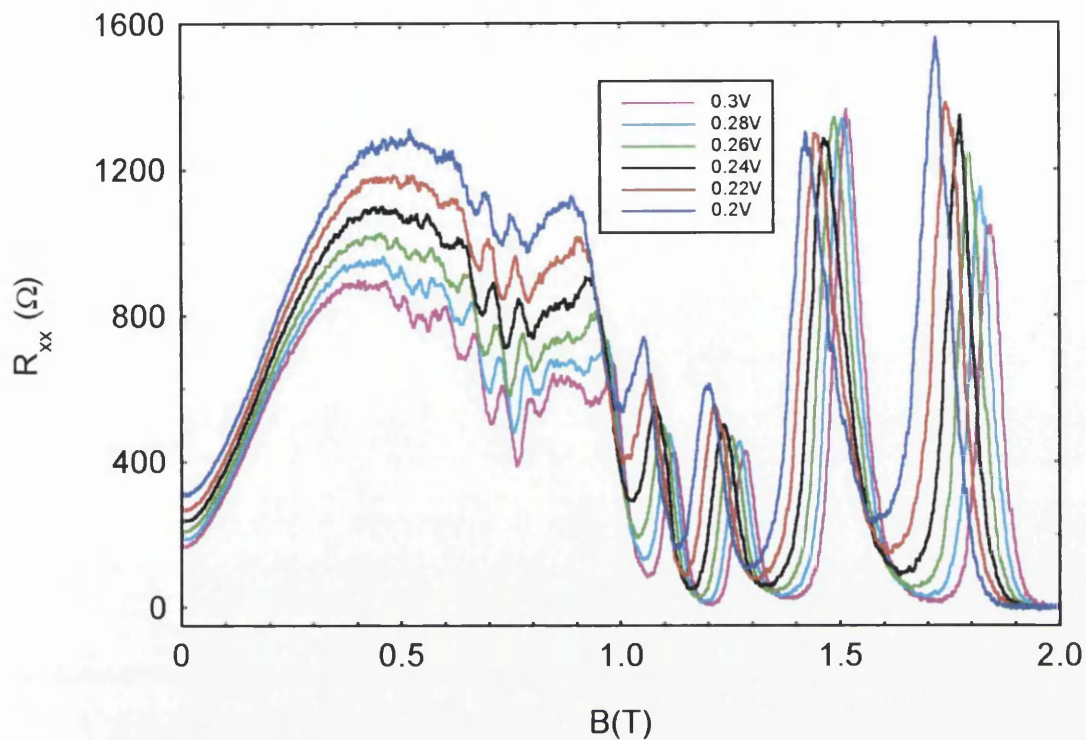


Fig. 7.13 voltage effects for Sections 1 and 2

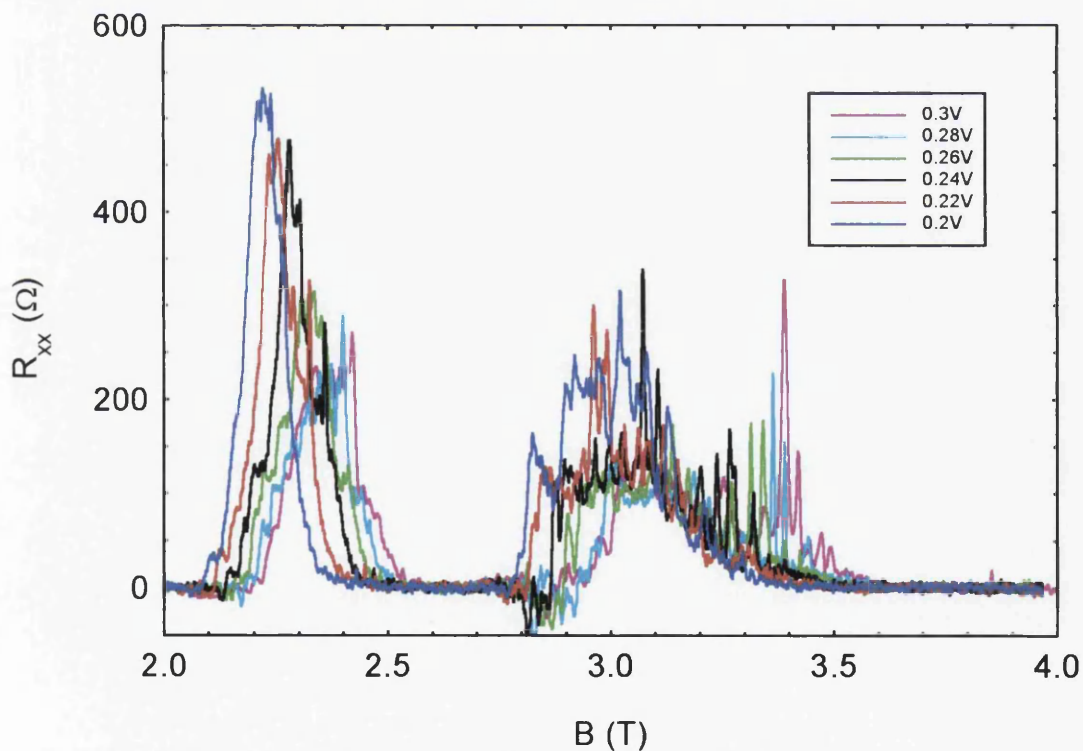


Fig. 7.14 Voltage effects for Section 3

The blanket gate is able to change the electron density without significantly altering the magnitude of the potential. It will vary the surface component of the potential but, as stated in Chapter 6, this is a small effect in these samples. As the carrier concentration reduces with more negative gate voltage each individual SdH oscillation is observed at a lower magnetic field (Eqn. 2.2).

Hence the Landau levels become closer together leading to more overlap between neighbouring levels, for any given filling factor. Thus, less well defined SdH oscillations are observed for any given filling factor.

As stated earlier, if there is significant overlap between SdH oscillations then the COs dominate. Thus, as the gate voltage decreases from 0.3V to 0.2V the carrier concentration drops and the SdH oscillations become less well defined. This is best illustrated at $k=2.5$ maximum.

Here, as the carrier concentration drops the minimum corresponding to $\nu=18$ becomes suppressed by the $k=2.5$ CO peak. Also, it can be seen that the SdH troughs for $\nu=10, 12$ etc. no longer reach to 0Ω . They are no longer fully separate and slightly overlap, allowing the CO behaviour to begin to reassert itself.

7.8 Hall resistance

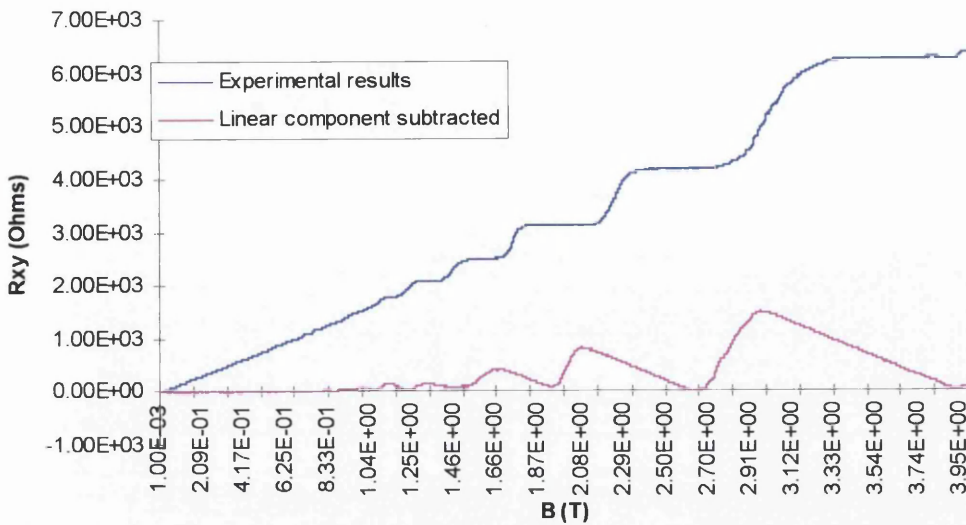


Fig. 7.15 Hall trace and with linear component subtracted for $[01\bar{1}]$ $V_g=0V$ $T=45mK$

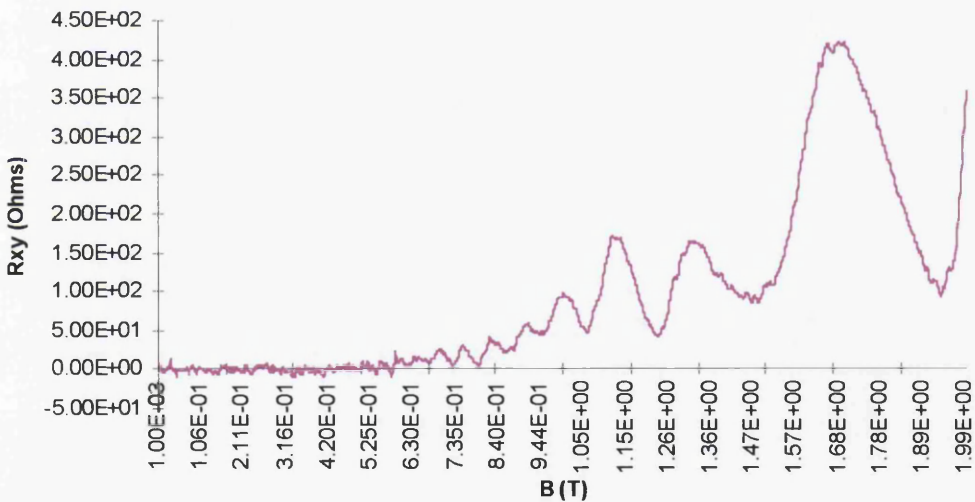


Fig. 7.16 The second trace (the trace with the linear component of the Hall effect estimated and reduced) shown in Fig. 7.15. The scales have been reduced to show the modulation in the peaks.

Measurements of the Hall resistance were also made. As they are difficult to interpret the linear component of the Hall effect was estimated and subtracted from the trace. This gives the trace seen in Fig. 7.16. A number of interesting things were noted in these. At low fields there appears to be a modulation in the heights of the resultant

oscillations at approximately 0.8T. We initially thought that this may be due to a similar effect to that which is seen to modulate the SdH oscillations, i.e. the strong COs. It was, however, noted that the modulation in the Hall trace does not move in a corresponding way to the modulation in the SdH when the gate voltage is altered, as can be seen in Fig. 7.17. Here the modulation moves to lower field with higher carrier concentration. For COs the modulation moves to higher field.

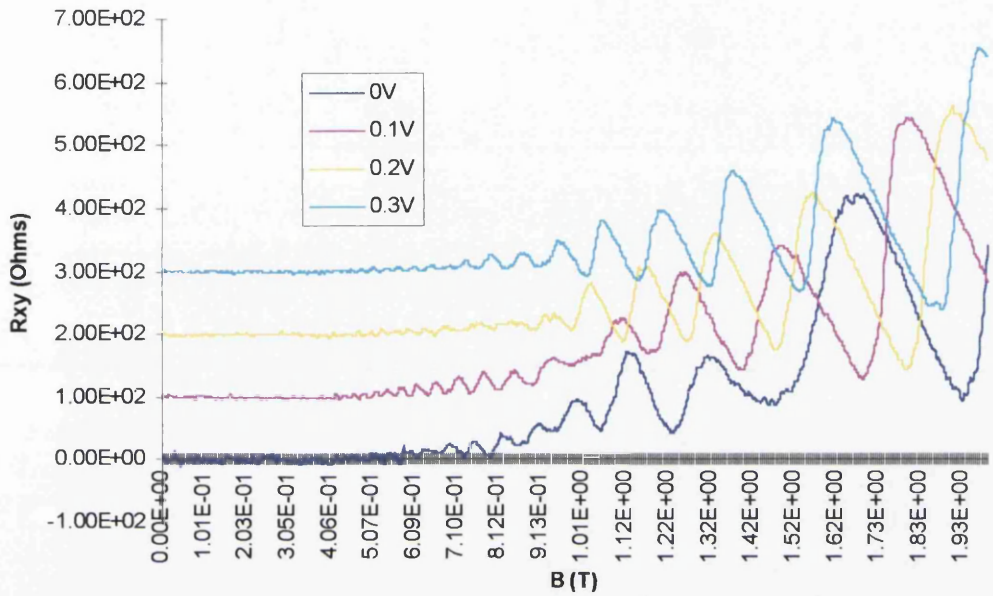


Fig. 7.17 Hall traces measured at different gate voltages. The linear component has been estimated and subtracted. Each trace is offset by 100Ω

From these traces it is possible to estimate the B field value that corresponds to a filled Landau Level. Plotting $\frac{1}{B}$ against filling factor should give a straight line with a gradient dependent on the carrier concentration (Eqn. 7.3). If this is plotted out (Fig. 7.18) then it can be seen that there appears to be a change of gradient, which occurs around the modulation point previously noted.

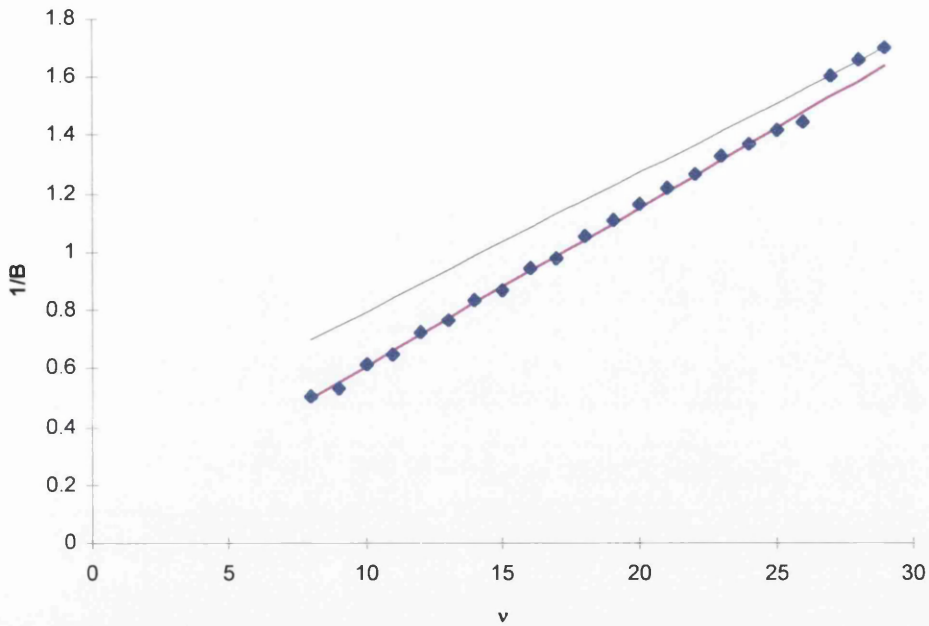


Fig. 7.18 $1/B$ v. ν for $[01\bar{1}]$, $T=45\text{mK}$, $V_g=0.3\text{V}$. Lines are added as guides to the two different gradients observed.

This change of gradient appears in all the Hall traces obtained, Fig. 7.20 illustrates the change with gate voltage. As can be seen the gradient change moves to higher filling factor (lower magnetic field) with increasing gate voltage. This is in the opposite direction to the movement of SdH oscillations and COs with gate voltage.

This behaviour is very similar to a theory by Albrecht et al [3], calculated for 2-D superlattices, which states there is a magnetic breakdown point where the orbit geometry changes, due to magnetic breakdown. This states that minigaps are visible in the repeated zone scheme which are overcome by an increase in magnetic energy. Thus the circumference of the Fermi surface increases. This is, however, the opposite of what we see, i.e. our results show a reduction of orbit geometry with an increase of field. Thus, we are presumably seeing a different effect, but we have not, as yet, pinned this down.

A second point of interest occurs at higher fields. The transitions from one Hall plateau to the next are not smooth. When looked at in derivative form it can be seen

that multiple peaks are seen. We believe this may be a similar effect to that seen in the SdH oscillations at similar magnetic fields.

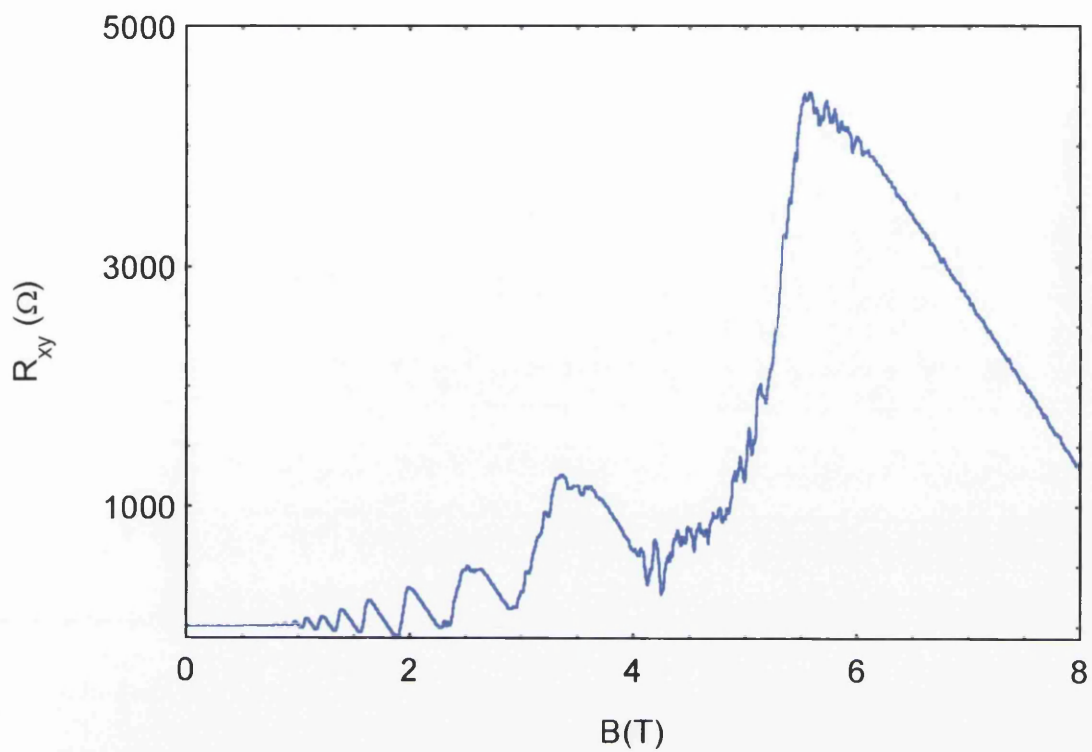


Fig. 7.19 Hall resistance at high magnetic field, $T=45\text{mK}$ $V_g=0.3\text{V}$ $[01\bar{1}]$ Linear component subtracted

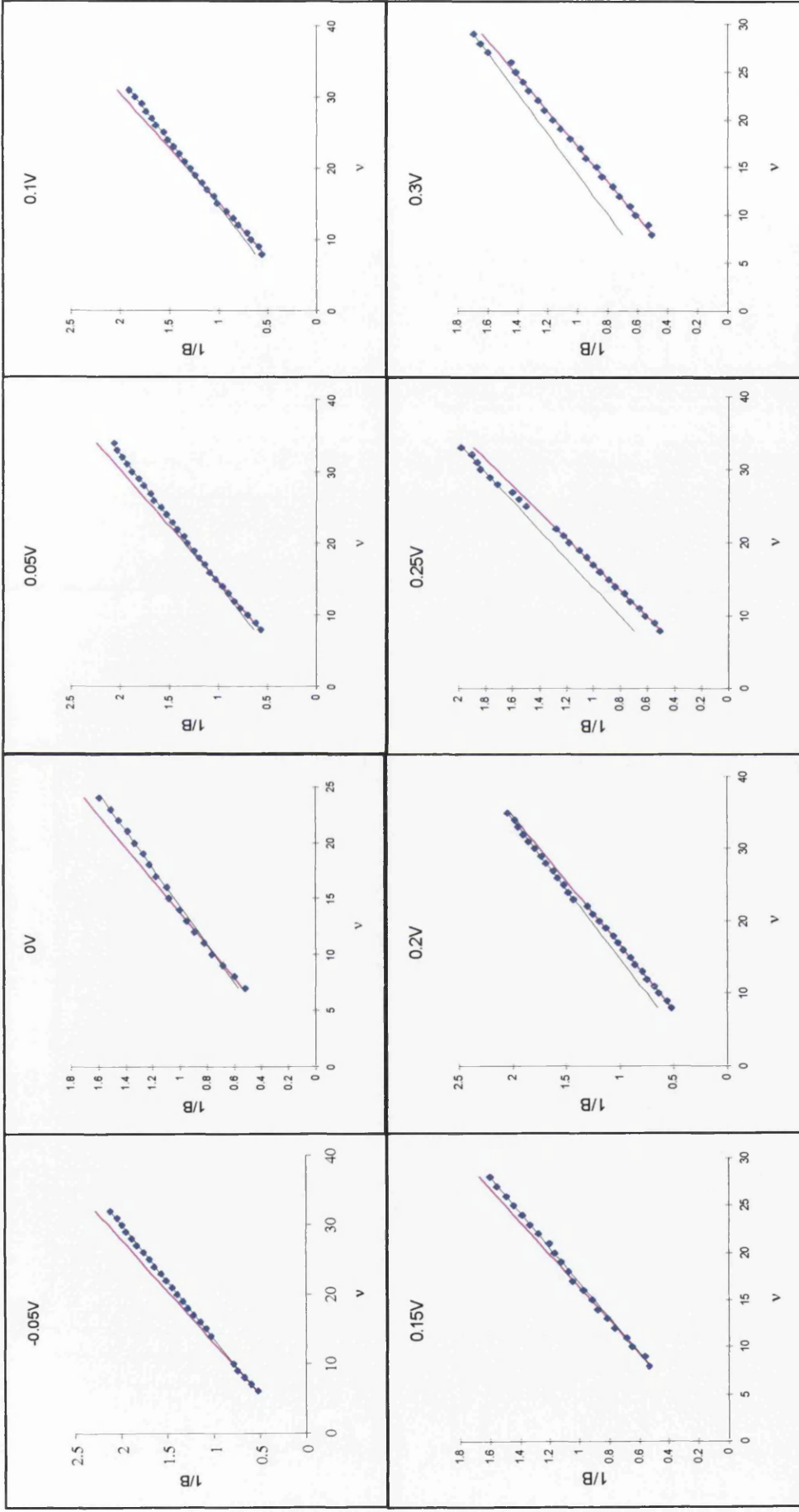


Fig. 7.20 $1/B$ against v as measured from Hall traces of samples $\langle 011 \text{ bar} \rangle$, $T=45\text{mK}$, $V_g=0.3\text{V}$. Coloured lines are guides as to the gradient of the two sections.

References

- [1] C. Zhang and R. R. Gerhardts Phys. Rev. B **41** 12850 (1990)

- [2] M.E. Raikh and T.V. Shahbazyan Phys. Rev. B **47** 1522 (1993)

- [3] C. Albrecht, J.H. Smet, D. Weiss, K. von Klitzing, R. Hennig, M. Langenbuch, M. Suhrke, U. Rössler, V. Umansky, H. Schweizer. Phys. Rev. Lett. **83** 2234 (1999)

Chapter 8 Conclusion

8.1 Fabrication technique

We have seen that it is possible to produce small period, regular one-dimensional patterns in a PMMA resist mask, using the beamwriter. These patterns can then be transferred to the wafer by two etching methods.

When it is working, the dry plasma etch technique provides more accurate depth control and allows all the samples to be etched simultaneously. Unfortunately, this etch hardens the resist mask, making it difficult to remove. This can lead to complications when spinning new resist, laying down gates or performing a topographic study using an Atomic Force Microscope. Unfortunately, problems with the equipment used in this technique caused long delays, which prevented a full study of the 200nm devices.

The second method, wet chemical etching, does not suffer from the resist hardening problem. Each sample has to be etched individually, one after another which can lead to error. Also, a new etching solution has to be produced for each etching day which can lead to variations in relative concentrations. Also, there is significant difference in etch time between control and stressor samples for the wet etch.

Both etching techniques suffer from short etch times. This makes the effect of timing errors more significant than is desired. The overall result, however, is good with regular, one-dimensional stressor ribs being produced.

These ribs then produce a strong potential modulation at the 2DEG which should show significant harmonic content. Unfortunately, it has been difficult to guarantee a fixed mark:space ratio, due to variations in beamwriter power, and etching efficiency, which strongly affects the harmonic content, as has been seen.

8.2 Experimental results

8.2.1 Introduction

We can strongly modulate the 2DEG with the periodic potential. This modulation was as large as ten percent of the Fermi level, a significant improvement on purely electrostatic gates. While this modulation has been seen to have a significant effect, it has not depleted the 2DEG, ensuring good mobility and a long mean free path.

8.2.2 300nm period samples

The 300nm samples proved that there was a piezoelectric potential involved in the modulation of the 2DEG. It also showed that there was a “surface” effect, due to the etching modulating the 2DEG. We were able to study the interaction of these two effects, along with a further potential introduced by the electrostatic gate, at a number of crystal directions. This showed that both the surface and gate potential components were isotropic, as expected, while the piezoelectric component varied with angle, as predicted by theory.

Also, we observed a strong second harmonic and proved that it was due solely to the piezoelectric contribution. This agrees with the piezoelectric theory. Also, we observed no harmonics in the surface effect, which supports our theory of a purely electrostatic effect.

Further, we studied the effects of temperature on our samples, and showed that they correspond to theory well, up to 25K. Some problems were encountered due to strong interaction between the SdH oscillations and the COs, especially for the $k=1$ CO.

The introduction of an electrostatic potential from the surface gate allowed us to “tune” the magnitude of the fundamental component of the potential. This allowed us to promote the second harmonic in the results and led us to believe we could produce small period superlattices, which we could then “tune” to obtain even smaller effective periods.

8.2.3 100nm period samples

The 100 nm samples further backed up our proof of a piezoelectric potential, in combination with a surface effect. Once again we saw no harmonics in the surface effect. However, we also saw no harmonics in the piezoelectric component, which were expected. This we attribute to the mark:space ratio not being exactly one to one. This showed the sensitivity of the piezoelectric effect to variations in the fabrication technique. This sensitivity does agree with the theoretical calculations. However, when the mark:space ratio was measured and the theoretical calculations carried out using the value obtained, a small second harmonic was still expected.

We calculated the potential magnitude for these 100nm period samples and discovered that, in the direction where the surface and piezoelectric contributions have the same sign, the resultant potential magnitude was approximately half the Fermi energy. This is no longer a small perturbation and we believe that the theory no longer holds true in all cases. We believe that this may contribute to the reason why no second harmonic was seen.

Unfortunately this illustrated that it would not be as simple to "tune" for small effective potentials as the 300nm period samples had led us to believe. This lack of second harmonic was further compounded by a lack of a gate effect upon the periodic potential. We believe that the trenches are now too small for a significant amount of gate metal to enter. Thus the contribution of the gate to the periodic potential was less than we would have hoped.

Due to the small period causing the COs to manifest at higher fields, there was a greater amount of interaction between SdH oscillations and COs. This led to problems when measuring results as well as leading us to cool the samples further, to study this interaction.

When the 100nm samples were cooled to 45mK a number of interesting effects were seen. The Shubnikov-de Haas oscillations were better defined and they showed a strong interaction with the Commensurability Oscillations. At low fields, we attributed this interaction to a quantum mechanical effect. The Commensurability Oscillations varied the width of the Landau Levels, which we were able to see as variations in the

height and definition of the Shubnikov-de Haas oscillations. At higher fields, we believe that the Shubnikov-de Haas oscillations were dominant, with the Commensurability Oscillations only being visible when conduction was in the bulk.

Further, we observed a set of peaks at high magnetic field which were independent of potential, and indeed of an InGaAs stressor layer. We believe these are due to anisotropies in the wafer, but further study is required to prove this.

8.2.4 200nm period samples

200nm samples were fabricated using a wet chemical etch. This was due to problems that had developed with the dry plasma etching equipment. Due to lack of time this new etch was not fully studied before the samples were produced. Hence this new wet chemical etch was very quick and the samples produced were over etched. In order to observe COs it was necessary to use a large positive voltage on the blanket gate, to attract electrons back into the channel. While COs were observed they were seen to be isotropic and it is believed that no piezoelectric effect was present. This we attribute to the over etched stressor layer relaxing. Some of this work has been published. [1,2,3]

References

[1] B. Milton, C.J. Emeleus, K.Lister, J.H. Davies and A.R. Long *Physica E*, **6** 555 (2000)

[2] C.J. Emeleus, B. Milton, A.R. Long, J.H. Davies, D.E. Petticrew and M.C. Holland *Superlat. and Microstuc.* **25** 39 (1999)

[3] C.J. Emeleus, B. Milton, A.R. Long, J.H. Davies, D.E. Petticrew and M.C. Holland *App. Phys. Lett.* **73** 1412 (1998)

Appendix A; Data Accumulation using National Instruments

Labview™ Software

A1 Introduction

Initially all computer measurement was done using Pascal programs written by Dr. Skuras and Dr. Long. I was asked to transfer these programs into the National Instruments Labview™ programming environment. This is a programming package that uses a graphic representation of a block of code rather than a text function (Fig. A.1). It is quite simple to use as it is mostly a case of connecting together pre-supplied functions in the desired form. However, if an instrument is required to be used that is not catered for then it can become quite complex.

A2 Basics of programming in Labview™

The basics of this programming system are relatively simple. A large number of functions, such as multiplication, open file and input integer, are supplied as sub-vis (VI - Virtual Instrument). These can be viewed in the diagram as a square box. They can be treated as a “black box” for the purposes of simple programming. Many can be opened up to allow more complex activities but that is usually not necessary. To allow passage of data from one block of code to another, the two blocks are “wired” together. All vis have a number of connectors built in. Simply drag the wire tool from the connector on one block to the requisite connector on the other block to connect the two functions together. A completed program is also known as a vi. It can, in turn, become a sub-vi in a larger program.

There is an element of colour coding involved in the diagrams, i.e. integers and wires leading from integers are blue, floating point numbers are orange, strings are pink etc. This can be very helpful when debugging. The system can also be run in such a way that every result produced can be displayed, allowing you to follow calculations through to spot the wrong operation.

The majority of measurement instrument manufacturers produce sets of vis which allow quick and easy interfacing with their hardware. Normally they will supply a set of basic building block sub-vis and an example of a fully functioning interface. It is then up to the individual to combine the building blocks into an interface suitable for their purposes, or just to use the example, if they wish. These vis are now available for the majority of modern equipment.

A3 Program Specifics

I initially took a program written by Dr. Long that measured the voltage across and the current through a sample while the magnetic field was ramped up or down and removed its bugs with a large amount of help from the manuals [1,2]. This was later expanded upon to add the ability to repeatedly sweep the magnetic field while changing the voltage upon the gate, at the end of each sweep. This was an option not available in the original Pascal program. This program is now in regular use by a number of members of the group and this has allowed the discovery of its many bugs and their correction. The one problem that has not been overcome is setting the sensitivity on the measurement equipment. This is not so much a problem with Labview as a question of standardising elapsed time. The time involved in checking each measurement and adjusting the sensitivity accordingly is too long and could result in irregular times between measured points.

After this, a number of programs were produced which are described below;

A.3.1 Gatesweep programs

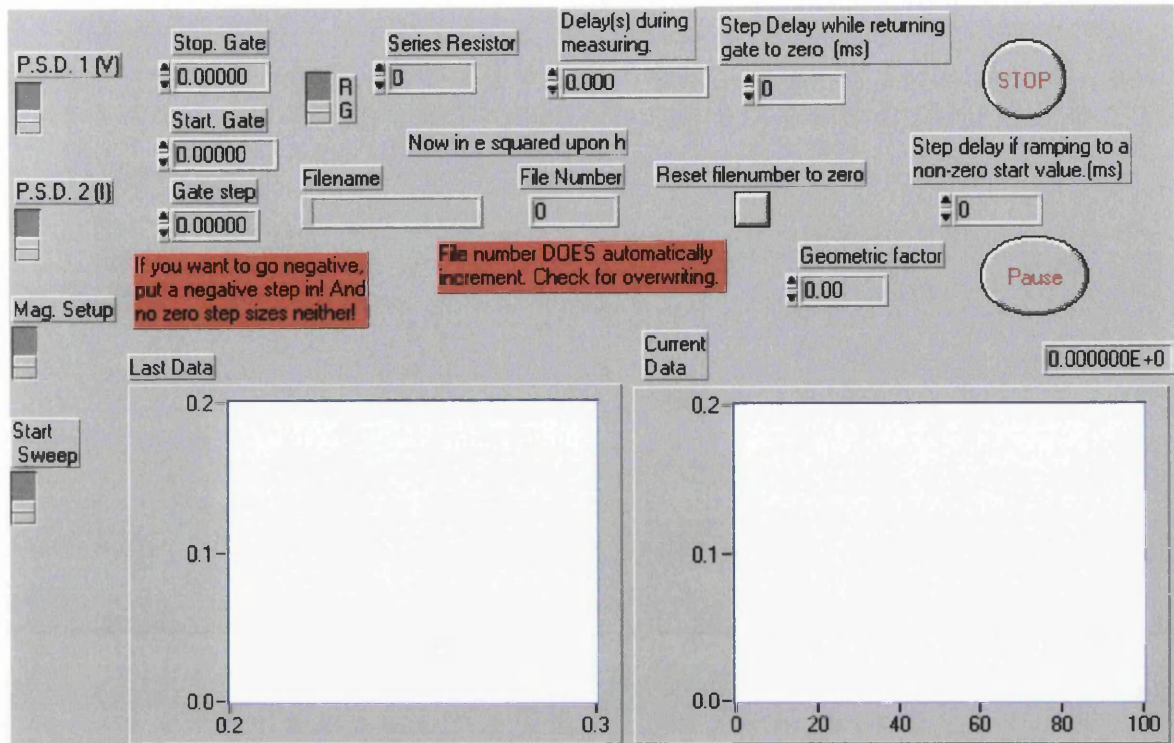


Fig. A.2 Front panel of EG&G Gatesweep program

Two of these were produced. One acquires current and voltage information from two EG&G 5210 lock-ins and one from a Keithley 236 source/measure unit. Both work in basically the same way. Type in the required information about filename, delays (both between measurements and between gate steps while ramping up or down), size of series resistor and the geometric factor. This factor allows calculations of resistance per square should it be required. The file number defaults to zero at the start. However, a dialogue box will appear at the start of the sweep to confirm if you wish to use zero. After this, the program will increment the filename by one after each run. It can be reset to zero with the button provided thus calling the dialogue box once again and allowing a change to your desired number.

Both programs also have the option to set up the instruments remotely. This includes the lock-ins/Keithley, the magnetic field power supply and the voltage source unit. Thus, it is possible to run all facets of a gate sweeping experiment solely from the software.

Once all the required values have been set up, toggling the Start Sweep button will begin the experiment. If, at any point during a sweep, values, such as the measurement instrument sensitivities, require to be altered, then the Pause button can be pressed. This will cause the program to halt, after the next measurement has been recorded, and display a dialogue box. Once the system is ready to proceed, pressing the Go button on this dialogue box will restart the program.

After a run is complete the program will save the data obtained to the filename specified, increment the filename by one and then wait for further instructions. At this point it is possible to change any of the variables before performing another sweep.

In order to illustrate the information being measured by the program, each data point is displayed on the Current Data graph. This only plots the resistance (or conductance) value against the number of points measured. Thus, a second chart is plotted after all the data has been acquired, which is displayed on the Last Data graph. This plots the data as resistance (or conductance) against gate voltage applied.

A.3.2 Magnetic sweep programs

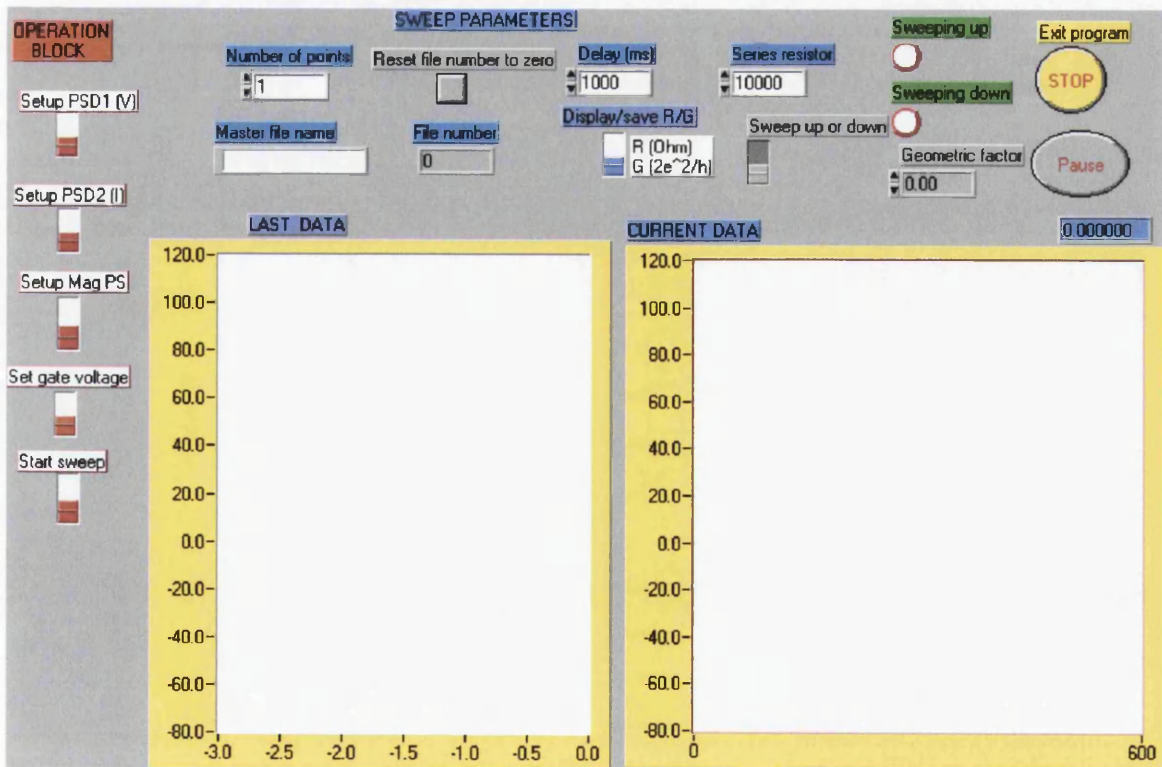


Fig. A.3 Single Magnetic Sweep program Front Panel

Two of these have also been produced. A program to simply sweep the field once and one to sweep a number of times at different gate voltages. The basic drill is the same as for the gatesweep programs. Fill in the relevant information, set up the magnet power supply and begin. Different things in this one are the number of points and a number of delays.

The magnet power supply runs on its own internal timer. To ensure that the computer keeps time with the magnet, you must calculate your number of points and delay between each point such that the last point measured is at your required field.

i.e. $\text{Number of points} * \text{Delay between points} = \text{Set field} / \text{Set Rate}$.

It is possible to sweep a field all the way from zero to the set point and back before incrementing the gate voltage or simply to sweep up to the set field, increment the voltage, sweep down, increment again and so on. The data measured is saved to disk at the end of each sweep, before the gate voltage is incremented. There is also a delay before the sweep when changing gate voltage. This is between the gate being set and the field beginning to sweep. It is there to allow time for the signal to settle.

As for the filename in the multiple sweep program, it can be set with the initial filename box. It will then increment at the start of each field sweep in a particular run.

A.3.3 Capacitance Programs

Once again two of these were produced. One for gatesweeps and one for magnetic sweeps. This program makes use of a Hewlett Packard 4274A Multi-Frequency LCR meter. This can measure the current through and the capacitance of a system under test, while the voltage across the sample is varied. It was necessary to write a driver for this device as none was available. Luckily, there was a driver for the next generation of device, 4275A, which it was possible to cannibalise, as a base from which to start. Both capacitance and conductance data are displayed, hence there are four graphs on the front panel. Other than that it works in the same way as the other programs. This program was not used in my work.

A.3.4 The FFT program

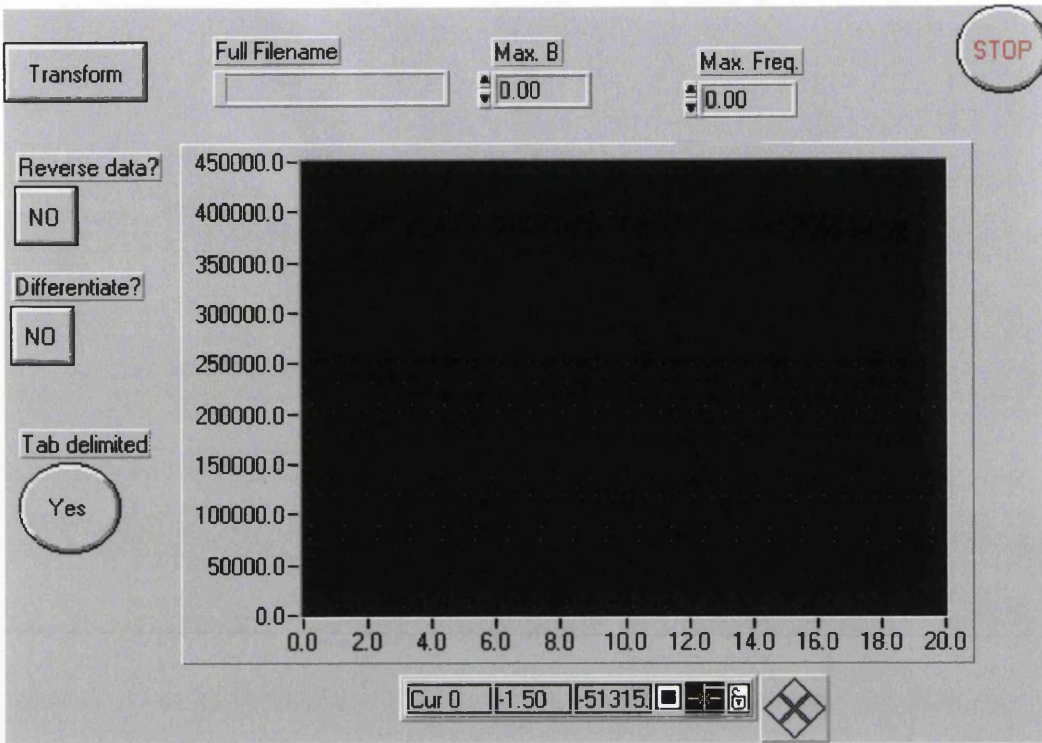


Fig. A.4 Front Panel of Fast Fourier Transform program

This will take a data file and produce a Fast Fourier Transform of it. There is also the option to differentiate the data before transforming to remove the average value. It is much quicker than the Pascal program previously used by the group, but gives slightly different results. I attribute this to the different algorithms being used.

An interesting problem with this program is that it expects to receive data in a certain format. This was the format initially used when outputting data from a measurement program. It consisted of only two columns, one for the variable being swept (magnetic field or gate voltage) and one for the value being measured (resistance or conductance). This format was changed later on to include two extra columns. These were the actual values measured from the lock-ins, which then were used to calculate the resistance (or conductance). It was then necessary to produce a further, small, program which would remove these extra columns before the data could be transformed.

References

[1] Labview Tutorial National Instruments Corporation 1994

[2] Labview User Manual National Instruments Corporation 1994

